

# **Recent Trends in Charged Particle Optics and Surface Physics Instrumentation**

## **Proceedings**

of the 16<sup>th</sup> International Seminar,  
held in Skalský dvůr near Brno, Czech Republic,  
from June 4 to June 8, 2018,  
organized by  
Institute of Scientific Instruments The Czech Academy of Sciences

**Edited by Filip Mika and Zuzana Pokorná**

Published and distributed by the Institute of Scientific Instruments The Czech Academy of Sciences, v. v. i. technical editing by Miroslav Janáček, printed by MJ servis spol. s.r.o.

Copyright © 2018 by the Institute of Scientific Instruments The Czech Academy of Sciences (ISI CAS) and individual contributors. All rights reserved. No part of this publication may be reproduced, stored in a retrieval system or transmitted in any form or by any means, electronic, mechanical, photocopying, recording or otherwise, without the written permission of the publisher, except as stated below. Single photocopies or single articles may be made for private study or research. Illustrations and short extracts from the text of individual contributions may be copied provided that the source is acknowledged, the permission of the authors is obtained and ISI CAS is notified.

The publishers have made every effort to reproduce the papers at their optimum contrast and with optimum resolution from materials provided by the authors. The publishers accept no liability for the loss of image quality resulting from supply of poor original material or improperly prepared digital records.

**ISBN 978-80-87441-23-7**

### **This seminar is dedicated to the memory of Professor Armin Delong (1925-2017)**

Armin Delong was the pioneer and founder of electron microscopy in Czechoslovakia. He built the first Czechoslovak electron microscope that was commercially available (1953) and founded the Institute of Scientific Instruments in Brno (1957), dedicated to the development of electron microscopy. His prototype of transmission electron microscope, BS242, won the Golden Medal at the Brussels World EXPO in 1958. His latest major creation, a desktop low-voltage TEM, came in the 2000's and became a popular cost-effective solution for high-contrast imaging of biological samples.

Armin Delong's legacy can hardly be overestimated. During his 30-year-long tenure as the director of the Institute of Scientific Instruments, extensive research was done on emission electron microscopy, holographic imaging and very low energy electron microscopy, both in the scanning and transmission mode. He oversaw the development of new prototypes of electron optics devices that dominated the Eastern Bloc market for 40 years.

He brought up a new generation of electron microscopy researchers who continue to push the boundaries of knowledge both in academia and the industry and it is due to his influence that Brno is now a vibrant hub of electron microscopy technology. A laureate of several prestigious awards, he has remained a kind and humble person.

Armin Delong, a fluent speaker of four languages, was born into a family of French immigrants settled near Ostrava, in the heart of Czech heavy industry region. As a boy, he fell in love with electronics and soon could construct a telephone or a simple radio – a rather dangerous wartime hobby, as the region was occupied by Nazis.

In 1945 he went to study at the Technical University in Brno where he became an assistant to Prof. Bláha, who then toyed with the idea of developing an electron microscope, as only a handful of industrially developed states could manufacture it at the time. A small team of students gathered around him who succeeded in producing the first working prototypes and in 1954, they founded the Laboratory of Electron Optics of the Czechoslovak Academy of Sciences which later went on to become the Institute of Scientific Instruments.

Two years later, TESLA, a Brno-based electronics company owned by the communist state, started producing the BS242, designed by A. Delong and his team. The BS242 aimed to be a simple, easy-to-operate, cost-effective electron microscope with the accelerating voltage of 30–75 keV, a modest resolution of 2 nm and astigmatism correction. In the Eastern Bloc, it became a sensation and about 1200 of these microscopes were sold. The Communist state played with the idea of some modest monetary award to its creators for each sold device, but, as Armin Delong recalled with a smile, “then they scrapped the idea, as that would make us millionaires, and you can't have millionaires in a workers' state”.

Procuring all the necessary materials and components was difficult in a tightly controlled and centrally directed Communist economy, and as A. Delong recalled, “We were always a bit

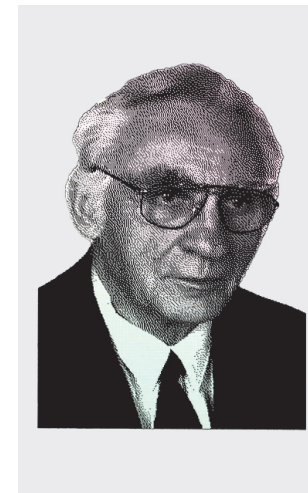
behind the world because of that. We had to resort to buying these things from people who smuggled them from abroad, or we had them bought in Switzerland illicitly.”

Armin Delong also taught at the Brno University of Technology, became the vice-president of the Czech Academy of Sciences and in the turbulent time after the fall of the Communist regime, even became a minister for science and technological development for a while. He disliked working in politics, however, and resigned after a few months.

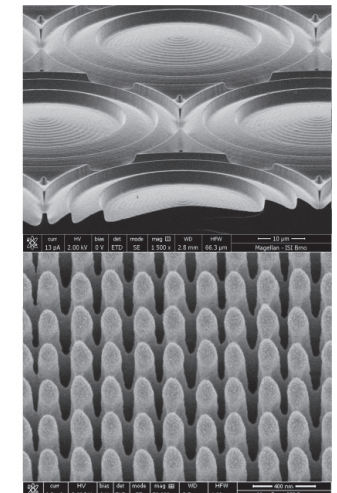
After the downfall of the Communist regime, the TESLA company disintegrated and several new, privately owned companies sprung up in its ashes. Each of them had Armin Delong's students in prominent positions, and one even chose his name as a badge of honor: Delong Instruments. Even though the company was not owned by Armin Delong, he worked in it at an emeritus position, helping more electron microscopy developments see the light of the day.

He was however a very modest man in private. Married to his high school sweetheart, he had a daughter (a professor at the Brno Academy of Music) and a son (an architect). He loved walking every day, and especially enjoyed the romantic nooks in the woods near Brno. He was a genial presence among his students, who would keep him company at lunch every day. He loved jokes and fun, and enjoyed going for a drink with his collaborators.

He was a regular participant at the Recent Trends seminar at Skalsky Dvur, mingling with students and senior researchers alike, cup of wine in hand, exchanging humorous remarks and serious scientific advice. This year's Wednesday hike mimics closely the one in 2012 when he last took part in the Recent Trends seminar.



Armin Delong, 1925–2017.  
Planar optical device composed of light-scattering and light-absorbing building blocks.  
*ISI Brno, EBL and SEM team.*



## SIXTY YEARS OF THE INSTITUTE OF SCIENTIFIC INSTRUMENTS

I. Müllerová<sup>1</sup>

<sup>1</sup>Institut of Scientific Instruments v.v.i., Czech Academy of Sciences, Královopolská 147, 61264 Brno, Czech Republic  
e-mail: ilona@isibrno.cz

The Institute of Scientific Instruments (ISI) was established in 1957 as an institution providing instrumental equipment for other institutes of the Academy of Sciences, mainly in the field of electron microscopy, nuclear magnetic resonance and coherent optics. Three examples are shown in Figure 1. In the beginning the institute had only 83 employees, including the workshop which produced the electronics and all mechanical parts of the instruments. During the process of post-Communist transformation of the Academy of Sciences, which began in 1989, the development of entire instruments and devices was brought to a halt and scientific activities of our Institute focused on the methodology of probing the physical properties of matter in the above-mentioned main fields. New components of scientific instruments were developed that help push the limits of what had previously been possible, continuing the long tradition of the Institute in these topics.

The history of electron microscopy at ISI is closely connected with prof. Armin Delong, its long-time director (1961-1990), who is also the founding father of Electron Microscopy research in Brno. During his tenure, many new electron optical devices were developed at the ISI.

During the history of electron microscopy, the energy of electrons illuminating the sample and also those bearing image information has ranged from units of electronvolts up to millions of electronvolts. For a long time, energy as high as reasonably possible was preferred because it offered superior resolution and suppression of some spurious effects. However, it was later recognized that fast electrons interact too weakly with the solid and the information they generate is averaged throughout too broad a region. The idea of slowing down the electron beam just with negative potential on the sample appeared in the 1960s and led to the development of Low Energy Electron Microscopes (LEEM) - dedicated, complicated and expensive devices. The Institute of Scientific Instruments took interest in this technique too, at the beginning of the 1970s [1].

The possibility of employing the same principle in the scanning electron microscope, in order to get an instrument much more flexible and also much cheaper, had been examined several times during the following three decades without much success. Then at the beginning of the 1990s, the ISI launched the Scanning LEEM (SLEEM) project without much fanfare [2-7] and by 2006, all the major producers of electron microscopes introduced the SLEEM method developed here into their products under various trade names (Beam Deceleration, Gentle Beam, etc.).

A huge part of the work at ISI was done in the field of Charged Particle Optics theory and software development [8-9]. A very popular type of detector was developed at the ISI in 1978, when Autrata et al. introduced a very sensitive BSE scintillation detector using the original YAG:Ce<sup>3+</sup> (yttrium aluminium garnet, Y<sub>3</sub>Al<sub>5</sub>O<sub>12</sub> doped with Ce<sup>3+</sup>) for the study of the material contrast of samples with a high sensitivity [10]. The first environmental scanning electron microscope (ESEM) in the Czech Republic (AQUASEM-I) was introduced at ISI in 1995.

Nowadays the Department of Electron Optics at the ISI concentrates on the development of Time-of-Flight spectroscopy at low primary beam energies [11], creation of vortex beams in r SEM [12], quantitative detection of secondary electrons [13], quantitative study of biological specimens in transmitted mode at low energies [14], cryo techniques [15], etc. Significant progress was done in the development of various types of ESEM detectors [16].

The mission of the ISI nowadays is the development of new diagnostics methods, novel instrumental principles and advanced technologies on all levels, from macro scale to quantum level. We aim for significant progress in understanding both inanimate and living nature and on employing this knowledge in practice. The principal activities of the ISI concentrate especially on multidisciplinary research and advanced engineering, combining the fields of magnetic resonance spectroscopy and tomography, electron microscopy and microanalysis, laser based spectroscopy, imaging, manipulation, and nanometrology, acquisition and processing of biosignals and large data, electron and laser beam technologies.

Some bare numbers concerning the ISI (as of 2017) are as follows: 173 FTE (full time equivalent) employees, 71 FTE researchers, 26 FTE PhD students, 76 papers with IF, 40 solved projects, 42 field patents or utility models, revenue from contractual research reached the sum of 11 800 kCZK. [17].



**Figure 1** Desktop electron microscope BS242, which obtained the Gold Medal at the Expo 58 World exhibition in Brussels (*left*). 30 MHz Nuclear Magnetic Resonance Spectrometer from 1961 (*middle*). First Czechoslovak gas laser from October 1963 (*right*).

## References:

- [1] Delong A., Drahoš V., Nature Physical Science **17** (1971) 196.
- [2] Lenc M., Müllerová I., Ultramicroscopy **45** (1992) 159.
- [3] Müllerová I., Frank L., Scanning **15** (1993) 193.
- [4] Frank L., Müllerová I. and Delong A., Czech. J. Phys. **44** (1994) 195.
- [5] Frank L., Müllerová I., J. Electron Microsc. **48** (1999) 205.
- [6] Müllerová I., Frank L., in: Advances in Imaging and Electron Physics, ed. P.W. Hawkes, **128**, Elsevier 2003, 309-443.
- [7] Frank L., et al, Materials **5** (2012) 2731.
- [8] Lencová B., Lenc M. and Hawkes P.W., Ultramicroscopy **108** (2008) 737.
- [9] Lencová B., Lenc M., Scanning Electron Microscopy, Chicago (1986) 897.
- [10] Autrata R., et al., Journal of Physics E: Scientific Instruments **11** (1978) 707.
- [11] Daniel B., et al., in this book of Proceedings
- [12] Řiháček T., et al., in this book of Proceedings
- [13] Mika, F., et al., in this book of Proceedings
- [14] Novotná V. et al., Microscopy and Microanalysis **20** (2014) 1270.
- [15] Samek O. et al., Journal of Biomedical Optics **20** (2015) 1.
- [16] Neděla, V., et al., Ultramicroscopy **184** (2018) 1.
- [17] This work was supported by the TE01020118 project of the Technology Agency of the Czech Republic (Competence centre: Electron Microscopy).

## CONTENTS

RING CATHODE ELECTRON BEAM PROJECTION LITHOGRAPHY <u>W. K. Ang</u> and A. Khurshheed	10
<hr/>	
OPTICAL BINDING OF POLYSTYRENE PARTICLES IN TRACTOR BEAM <u>J. Damková</u> , L. Chvátal, J. Oulehla, J. Ježek, O. Brzobohatý and P. Zemánek	12
<hr/>	
VERY LOW ENERGY ELECTRON TRANSMISSION SPECTROMICROSCOPY <u>B. Daniel</u> , T. Radlička, J. Piňos, E. Mikmeková, I. Konvalina, L. Frank and I. Müllerová	14
<hr/>	
OPTIMIZATION OF THE EDGE REGION OF A QUADRUPOLE MASS ANALYZER <u>M.V. Dubkov</u> , V.V. Ivanov, M.A. Burobin and A.V. Nikolaev	16
<hr/>	
ELECTRON BEAM WELDING AT ISI BRNO <u>L. Dupák</u> , M. Zobač, I. Vlček, J. Zobačová	18
<hr/>	
MULTI-REFLECTION TIME-OF-FLIGHT ION TRAP WITH ISOCHRONOUS DRIFT <u>D. Grinfeld</u> , C. Hock, H. Stewart, A. Makarov	22
<hr/>	
OPTIMIZATION OF ELECTROSTATIC LENS SYSTEMS USING GENETIC ALGORITHMS <u>N. Hesam Mahmoudi Nezhad</u> , M. Ghaffarian Niasar, A. Mohammadi Gheidari, T. Janssen, C.W. Hagen, P.Kruit	24
<hr/>	
STRUCTURE INVESTIGATION OF HYDROGELS USING A CRYO-SEM K. Adamkova, <u>K. Hrubanova</u> , O. Samek, M. Trudicova, P. Sedlacek, V. Krzyzanek	26
<hr/>	
MONOCHROMATIZING WITHOUT FILTERING: PROPOSAL FOR A MICROWAVE BASED LOW LOSS MONOCHROMATOR FOR S(T)EM <u>R. Janzen</u>	30
<hr/>	
MAPPING MATERIAL SCIENCE PROPERTIES ON THE NANOSCALE BY SECONDARY ELECTRON ENERGY SPECTROMETERS IN THE SEM <u>A. Khurshheed</u> , H. Weiding, and A. Banerjee	32
<hr/>	
FIELD EMISSION FROM W5O14 NANOWIRES M. Saqib, <u>A. Knápek</u> , J. Jelenc, L. Pirker	34
<hr/>	
HIDING E-BEAM EXPOSURE FIELDS BY DETERMINISTIC APERIODIC 2D PATTERNING M. Horáček, <u>A. Knápek</u> , M. Matějka, S. Krátký, M. Urbánek, F. Mika, V. Kolařík	36
<hr/>	

SEM LEEM – NEW TYPE OF MIRROR MICROSCOPE <u>V. Kolařík</u> , P. Jánský and M. Mynář	38	CREATION OF ELECTRON VORTEX BEAMS USING THE HOLOGRAPHIC RECONSTRUCTION METHOD IN A SCANNING ELECTRON MICROSCOPE <u>T. Řiháček</u> , M. Horák, T. Schachinger, M. Matějka, F. Mika and I. Müllerová	66
STEM MODES IN SEM <u>I. Konvalina</u> , A. Paták, E. Mikmeková, F. Mika and I. Müllerová	40	SECONDARY ELECTRON HYPER SPECTRAL IMAGING IN HELIOS NANOLAB – MAPPING MATERIALS PROPERTIES OR ARTEFACTS? <u>C. Rodenburg</u> , R. Masters, K. Abrams, M. Dapor, S. Krátký & F. Mika	68
ULTRA-HIGH ENERGY RESOLUTION EELS <u>O.L. Krivanek</u> , A.L. Bleloch, G. Corbin, N. Dellby, M.V. Hoffman, and T.C. Lovejoy	42	PROSPECTS AND RESULTS OF ATOMIC-RESOLUTION LOW-VOLTAGE TEM <u>H. Rose</u> and U. Kaiser	70
STABLE Ce <sup>4+</sup> CENTRES – A TOOL TO OPTIMIZE CATHODOLUMINESCENCE PERFORMANCE IN GARNET SCINTILLATORS <u>O. Lalinský</u> , P. Schauer, M. Rathaiah, M. Kučera	44	GRAPHENE-BASED CATHODE COLD FIELD EMISSION SOURCES FOR ELECTRON MICROSCOPY AND LITHOGRAPHY <u>X. Shao</u> , W.K. Ang and A. Khurshed	72
POSSIBILITIES OF A SECONDARY ELECTRONS BANDPASS FILTER FOR STANDARD SEM <u>F. Mika</u> , Z. Pokorná, I. Konvalina and A. Khurshed	46	THICKNESS DETERMINATION OF A CATHODOLUMINESCENCE ACTIVE NANOPARTICLES BY MEANS OF QUANTITATIVE STEM IMAGING <u>R. Skoupy</u> and V. Krzyzaneck	74
ELECTRON OPTICS OF THE MULTI ELECTRON BEAM SOURCE (MBS) FOR AN MBSEM <u>A. Mohammadi-Gheidari</u> , X. Guo and P. Kruit	50	ORBITAL MOTION FROM OPTICAL SPIN: THE EXTRAORDINARY MOMENTUM OF CIRCULARLY POLARIZED LIGHT BEAMS <u>V. Svak</u> , O. Brzobohatý, M. Šiler, P. Jákl, P. Zemánek, S. Simpson	78
ANALYSIS OF LINEAR ION PAUL TRAPS USING 3-D FEM AND THE AZIMUTHAL MULTIPOLE FIELD EXPANSION <u>M. Oral</u> , O. Číp and L. Slodička	52	GRAZING INCIDENCE INTERFEROMETER FOR FORM MEASUREMENT OF HOLLOW CYLINDERS <u>M. Sarbort</u> , S. Rerucha, M. Hola and J. Lazar	80
OPTOFLUIDIC TECHNIQUES FOR DIRECTED EVOLUTION OF ENZYMES <u>Z. Pilát</u> , J. Ježek, O. Samek, P. Zemánek, T. Buryška, J. Damborský and Z. Prokop	56	IMAGING VIA MULTIMODE OPTICAL FIBER: RECOVERY OF A TRANSMISSION MATRIX USING INTERNAL REFERENCES <u>M. Šiler</u> , P. Jákl, J. Traegaardh, J. Ježek, H. Uhlířová, T. Tučková, P. Zemánek, and T. Čižmár	82
REAL TIME OBSERVATION OF STRAIN IN THE SEM SAMPLE <u>J. Piños</u> , L. Frank	58	LOCKING IN ON LARGE VOLUME LIGHT-SHEET MICROSCOPY <u>T. Vettenburg</u> , H.I.C. Dalgarno, J. Nylk, C. Coll-Lladó, D.E.K. Ferrier, T. Cižmár, F.J. Gunn-Moore, and K. Dholakia, A. Corral, A. Rodríguez-Pulido, C. Flors, and J. Ripoll	84
THERMAL DESORPTION SPECTROSCOPY IN PROTOTYPE FURNACE FOR CHEMICAL VAPOR DEPOSITION <u>L. Průcha</u> , B. Daniel, J. Piños, E. Mikmeková	60	INELASTIC MEAN FREE PATH FROM RAW DATA MEASURED BY LOW-ENERGY ELECTRONS TIME-OF-FLIGHT SPECTROMETER <u>M. Zouhar</u> , T. Radlička, M. Oral and I. Konvalina	86
DEVELOPMENT OF A COMPACT MASS SPECTROMETER FOR SPACE APPLICATIONS <u>R. Puretj</u> , H. Q. Hoang, and T. Wirtz	62		
ELECTRON OPTICAL PROPERTIES OF A NEW LOW-ENERGY SCANNING ELECTRON MICROSCOPE WITH A BEAM SEPARATOR <u>T. Radlicka</u> , <u>V. Kolařík</u> , <u>M. Oral</u>	64		

## RING CATHODE ELECTRON BEAM PROJECTION LITHOGRAPHY

W. K. Ang<sup>1</sup> and A. Khursheed<sup>1,2\*</sup>

<sup>1</sup>Department of Electrical and Computer Engineering, National University of Singapore, 4 Engineering Drive 3, Singapore 117583

<sup>2</sup>Engineering Science Programme, National University of Singapore, 9 Engineering Drive 1, Singapore 117575

\*e-mail: eleka@nus.edu.sg

Recently, a new cold field emitter has been fabricated, which consists of a graphene-coated ring-shaped cathode [1]. Preliminary experimental results show that it can produce high emission currents at relatively low applied electric field strengths in high vacuum (HV) conditions, as opposed to the usually required ultrahigh vacuum (UHV) conditions. This ring-cathode emitter has the potential to serve as a promising high brightness electron source suitable for electron lithography.

In this study, the novelty of writing a ring-shaped pattern directly from the cathode, as opposed to using a point source in combination with a patterned aperture, will be examined. Numerical simulations with direct ray tracing modelling are carried out to examine the ring image characteristics of a ring cathode column as compared to that of a conventional point source electron beam focusing column using an annular aperture. Figure 1 shows the schematic layout of the simple test columns suitable for this aim, which consists of an electron source, an appropriate aperture and a magnetic objective lens.

Simulation results show that a high resolution ring-shaped pattern can be obtained for the ring-cathode column with a conventional hole-aperture. Aberration analysis reveals third-order geometric aberrations in the in-plane direction for the projected ring patterns, which is an order of magnitude better than that predicted for the point source emitter with an annular aperture, which has second-order geometric aberrations. An image ring width resolution of 1.4 nm is predicted for emission from a 5  $\mu\text{m}$  diameter ring-cathode with an edge-thickness of 3 nm, a ring beam voltage of 5 kV, a ring image radius of 0.4  $\mu\text{m}$ , a final semi-angle of 2 mrad, and a working distance of 5 mm. In comparison, an ideal point source column using the same magnetic objective lens is predicted to have a resolution of 14.3 nm, an order of magnitude worse. Figure 2 shows the simulated ring widths versus final semi-angular spread for both columns. These simulations were carried out through the use of Lorentz-2EM [2], a boundary element software with an integrated fifth order Runge-Kutta time integration technique for electron trajectory paths plotting. These kinds of simulation results point towards the possible use of ring cathode emitters for ring pattern generation in electron beam lithography where high spatial resolution is combined with high throughput.

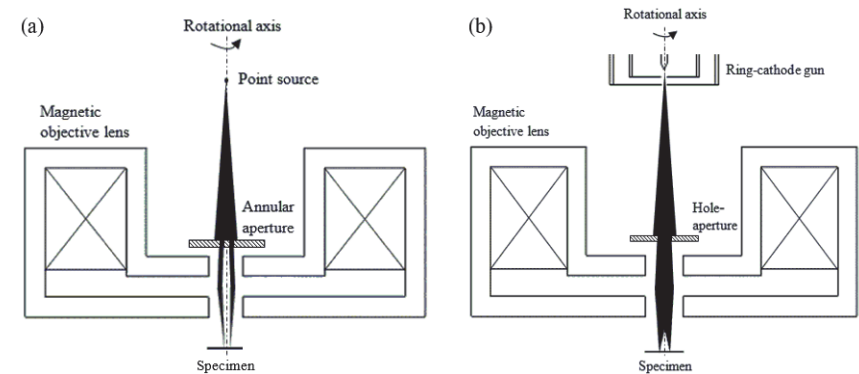


**Figure 1** Schematic diagram for ring pattern writing. (a) Conventional point electron source with an annular aperture. (b) Ring-shaped electron source with a conventional hole-aperture.

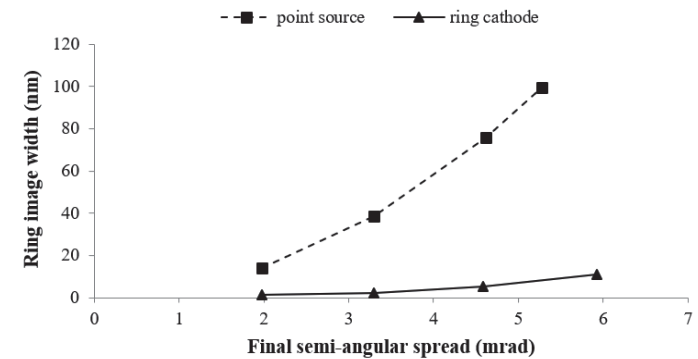


**Figure 2** Simulated focused ring widths as a function of the final semi-angular spreads.

This research is funded by National Research Foundation (NRF), Singapore Competitive Research Programme (CRP) award # NRF-CRP13-2014-04 titled “Micro-fabricated Ring Carbon Nanotube electron/ion sources”.

References:

- [1] X. Shao, A. Srinivasan, Y. Zhao and A. Khursheed, Carbon **110** (2016), p. 378-383.
- [2] Lorentz-2EM, Integrated Engineering Software Inc., Winnipeg (2016).

## OPTICAL BINDING OF POLYSTYRENE PARTICLES IN TRACTOR BEAM

J. Damková<sup>1\*</sup>, L. Chvátal<sup>1</sup>, J. Oulehla<sup>1</sup>, J. Ježek<sup>1</sup>, O. Brzobohatý<sup>1</sup> and P. Zemánek<sup>1</sup>

Institute of Scientific Instruments of the CAS, v.v.i., Královopolská 147, Brno 612 64, CZ

\*e-mail: jdamkova@isibrno.cz

The motion of a particle illuminated by a laser beam is usually driven by the photon flow due to the radiation pressure and therefore for particle trapping, one has to employ gradient forces. But in a tractor beam, objects are illuminated by the uniform light intensity and even so they can be pulled against the beam propagation. There have been developed several techniques how to create such a tractor beam. In our case, the tractor beam is created by two identical Gaussian beams that interfere under the defined angle [1], see Figure 1a. It creates the standing wave, where in the transversal plane the particle is trapped by means of the gradient force, but in the total beam propagation direction, the particle manipulation is driven by the non-conservative force. It is remarkable that this force can for the specific combinations of parameters pull the micro-particle against the beam propagation. This kind of behavior is because of the particle scattering where the majority of the incident photons is scattered in the forward direction and, based on the principle of action and reaction, the transfer of momentum leads to a backward movement of the object. The pushing and pulling force is sensitive to the polarization of the laser beam, its incident angle and the particle size so this technique can be used for example for sorting of objects of different sizes.

The acting on objects by the pushing / pulling force can be enhanced by particle self-arrangement due to optical binding [2]. The field scattered by an object interferes with the tractor-beam field and there are created suitable positions where the second particle can be preferably trapped due to the optical gradient force. In this way these objects interact mutually and organize themselves into various configurations.

We experimentally observed that under certain circumstances, the pulling force can be significantly enhanced comparing to a single particle in the tractor beam [3]. We analysed particle 3D trajectories utilizing the holographic video microscopy technique [4] during their forward and backward movement while all the beam parameters remaining unchanged, and we observed significant changes in their relative positions comparing those two directions of their motion. Our experimental observations were supported by numerical calculations based on the exact theory of multiple particle Mie scattering [5]. The theory perfectly agreed together with the experimental data in the stable positions of the particle pair and in the direction of the particle pair motion, see Figure 1b.

In addition to numerical calculations and experimental observations, we introduce an intuitive picture of the mechanism of pulling and pushing of the pair of particles. Due to the asymmetry in the system given by the angle of the tractor beam the particle pair is self-propelled parallel or anti-parallel to the tractor-beam propagation depending only on the internal configuration of the optically bound pair. Understanding the physical mechanism opens new opportunities in a controllable light-driven self-organization, sorting and transport of colloidal matter.

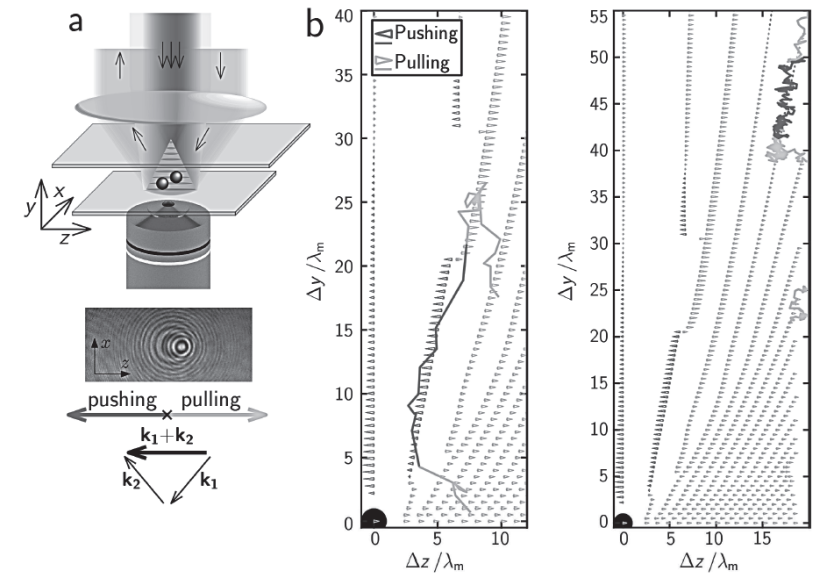


**Figure 1** a) Optical setup consisting of the tractor beam (bevel beam) and holographic video microscopy (beam perpendicular to the sample plane). The colloidal solution with polystyrene 820 nm particles is between the cover glasses. The typical hologram of two optically bound particles is shown under the objective lens. b) Numerically calculated stable positions of optically bound particles in the tractor beam, one placed at the coordinate origin, the possible positions of the second particle marked with arrowheads. The solid zigzag lines represent experimentally obtained trajectories of optically bound particles.

### References:

- [1] Brzobohatý, O., Karásek, V., Šiler, M., Chvátal, L., Čížmár, T. and Zemánek, P., *Nature Photonics* **7** (2013), p. 123-127.
- [2] Brzobohatý, O., Čížmár, T., Karásek, V., Šiler, M., Dholakia, K. and Zemánek, P., *Optics Express* **18** (2010), p. 25389-25402.
- [3] Damková, J., Chvátal, L., Ježek, J., Oulehla, J., Brzobohatý, O. and Zemánek, P., *Light: Science & Applications* **7** (2018), p. 17135
- [4] Lee, S.H. and Grier, D.G., *Optics Express* **15** (2007), p. 1505-1512.
- [5] Mackowski, D., Springer Berlin Heidelberg, Berlin (2012).

### Acknowledgement:

The research was supported by the projects of CSF (GA14-16195S), TACR (TE01020233) and its infrastructure by MEYS CR, EC, and CAS (LO1212, CZ.1.05/2.1.00/01.0017, RVO:68081731). JD was supported by Brno Ph.D. Talent program

## VERY LOW ENERGY ELECTRON TRANSMISSION SPECTROMICROSCOPY

B. Daniel\*, T. Radlička, J. Piňos, E. Mikmeková, I. Konvalina, L. Frank and I. Müllerová

Institute of Scientific Instruments of the CAS  
Královopolská 147, 612 64 Brno, Czech Republic  
\*e-mail: bdaniel@isibrno.cz

For more than 25 years, Scanning Low Energy Electron Microscopy (SLEEM) has been developed at the Institute of Scientific Instruments (ISI), with several commercially available SEMs adapted with a cathode lens for SLEEM use, as well as a dedicated self-built UHV SLEEM setup [1].

For a better understanding of contrast formation at low energies, especially at very low energies below 50 eV, where the local density of states plays an important role, more general knowledge about the interaction of (very) low energy electrons with solids is required. This will be achieved using a newly developed ultra-high vacuum (UHV SLEEM) setup which includes several enhancements compared to other available machines. Data processing is presented in [2], and processed data will be further used and tested with the Monte Carlo simulation package BRUCE, which is being developed by Werner et al. at TU Vienna.

A schematic overview of the new instrument is given in Figure 1 a). The UHV setup with a base pressure of  $10^{-9}$  mbar consists of a low voltage SEM with up to 5 keV primary beam energy developed by Delong Instruments, a home-built specimen stage including a manipulator with high voltage biased specimen stage, and several electron detectors. The latter consist not only of common SLEEM detectors, namely a disc-shaped YAG scintillator with a 300  $\mu\text{m}$  central bore for BSE detection, and a PIN diode for detection electrons transmitted through very thin specimens like graphene, transition metal dichalcogenides or ultra-thin metal films, but also of several new detectors which have been added to this system. The electron optical column is extended by magnetic prisms, which allow separation of reflected electrons on the beam axis from the incident electron beam (top part of Figure 1 a). This is especially important, since with decreasing landing energies and thus immersion ratios of the cathode lens, an increasing fraction of the secondary electrons is accelerated through the central bore of the BSE detector and thus cannot be detected without such an on- and near-axis detection system (see Figure 1 b). There is a scintillator available for integral detection of those electrons, as well as a segmented semiconductor detector that allows a rough separation of SE and BSE, where the trajectories are split up by the magnetic field.

For transmitted electrons there is developing a Timepix 2D pixel-detector implemented, which allows measurement of angular distribution. The second enhancement of TE detection is a time-of-flight (ToF) spectrometer for energy analysis of transmitted electrons. This enables the possibility of EELS measurements known from common high energy TEMs, and analysis of SE spectra. From information gathered by the new detectors, improvements on knowledge of inelastic mean free path (IMFP) at very low energies is expected, as well as enhancement of previous results of graphene electron reflectivity and transmissivity [3,4] (Figure 1 c).

Results from this new setup and the above mentioned cooperation with TU Vienna are expected to yield an improved understanding of electron – specimen interaction in general, with focus on IMFP and a further goal of progressing on the road towards SEM single image tomography by angle and energy analysis of reflected electrons.

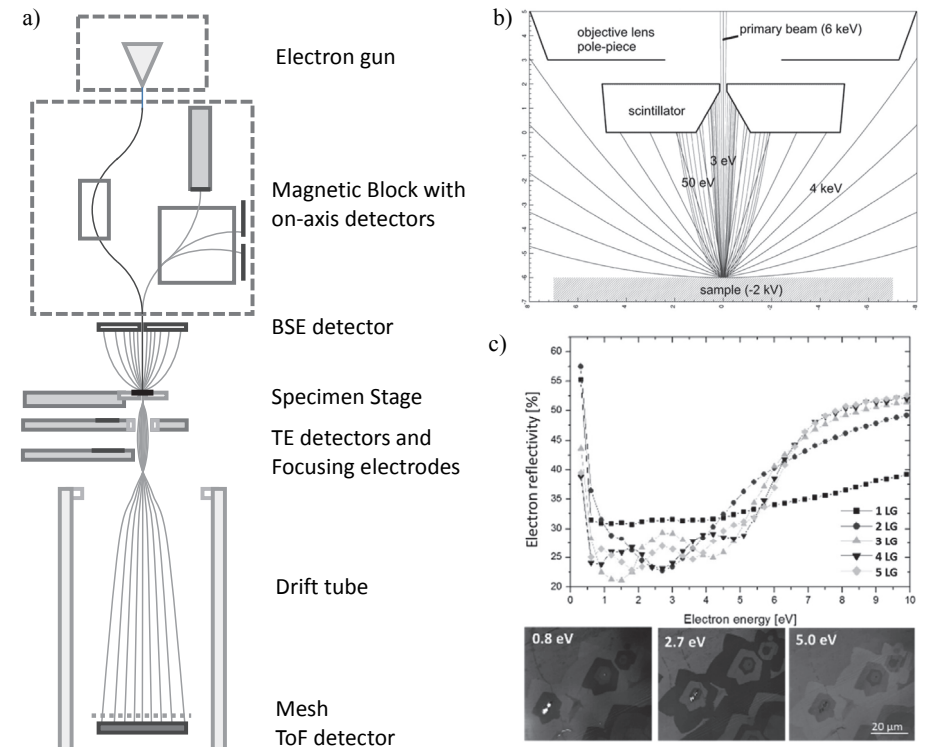


**Figure 1** a) Schematic drawing of the SLEEM – ToF system, b) Signal electron trajectories in SLEEM [5], c) electron reflectivity of supported graphene [4]

### References:

- [1] Müllerová I. and Frank L., *Adv. Imaging Electron Phys.* **128** (2003), p. 309-443
- [2] Zouhar, M., Radlička, T., Oral, M. and Konvalina I., *Recent Trends 2018*
- [3] Frank L., Mikmeková E., Müllerová I. and Lejeune M., *Appl. Phys. Lett.* **106** (2015), 013117
- [4] Mikmeková E., Frank L., Müllerová I., Li B.W., Rouff R.S., Lejeune M., *Diamond & Related Materials* **63** (2016) 136–142
- [5] Frank L., Hovorka M., Konvalina I., Mikmeková Š., Müllerová I., *Nuclear Instruments and Methods in Physics Research A* **645** (2011) 46–54

This project has received funding from the People Programme (Marie Curie Actions) of the European Union's Seventh Framework Programme FP7/2007-2013/ under REA grant agreement no 606988.

## OPTIMIZATION OF THE EDGE REGION OF A QUADRUPOLE MASS ANALYZER

M.V. Dubkov<sup>1</sup>, V.V. Ivanov\*, M.A. Burobin and A.V. Nikolaev

<sup>1</sup>Ryazan State Radio Engineering University, 390005, Ryazan, Gagarina str, 59/1  
\*e-mail: vladimir.nvi@gmail.com

The limited space leads to the formation of edge regions in the analyzer of the quadrupole mass filter. The electric potential distribution differs from the ideal quadratic one within these regions. The introduction of charged particles into the volume of the mass analyzer is usually carried out through the input diaphragm, located at some distance from the end surfaces of the electrodes. The region of the edge field thus formed has a negative effect on the parameters of the ion flux introduced into the analyzer. These ions move in a field whose equipotential lines are bent in the direction of the planar diaphragm at the inlet (Fig.1a). Such a field increases ion velocities in directions perpendicular to the axis of the mass analyzer. This leads to the settling of stable ions on the electrodes and a decrease in the transmittance of the mass spectrometer. It is known that the negative influence of the input region can be reduced by selecting the shape of the input diaphragm. This work is devoted to the choice of the design of the input diaphragm, which makes it possible to obtain a transmittance of the mass filter higher than in the case of “undistorted” fields.

We simulated the motion of charged particles through a quadrupole mass filter in order to determine the optimal design of the input diaphragm. It is obtained that the largest transmission capacity is provided by the use of an input diaphragm with two parallel rectangular projections entering the interior of the electrode system by an amount on the order of the characteristic field size. In this case, near the input diaphragm, an electric field is formed, which focuses the charged particles (Fig. 1b). The use of such a construction increases the transmittance of a quadrupole mass analyzer. In the case when a pulsed RF voltage is applied to the electrodes, the intensity of the mass peak increases by a factor of 1.5 with a resolution of 0.5, equal to 150, by a factor of 2 with a resolution of about 180 and by a factor of 3 or more with a resolution of more than 300. This increase in intensity is not accompanied by a significant change in the resolution of the device (Fig. 2). This indicates that the increase in the number of ions able to fly through the mass analyzer is due to stable ions, initial flight conditions which previously did not allow them to overcome the sensor area.

Thus, the proposed shape of the input diaphragm of the quadrupole mass filter makes it possible to significantly increase the intensity of the mass peak at a high resolution of the mass spectrometer. Such a design allows to achieve an increase in the analytic characteristics of the device to a greater extent than the proposed and used earlier designs of the input diaphragm.

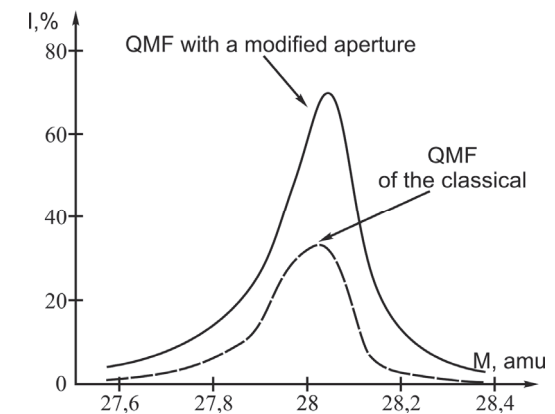


Figure 1 The forms of mass peak

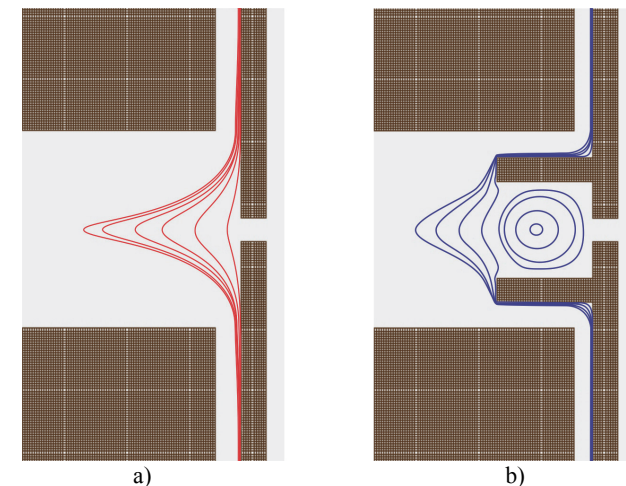


Figure 2 The electric field at the input area of the mass filter.

## ELECTRON BEAM WELDING AT ISI BRNO

L. Dupák<sup>1</sup>, M. Zobač<sup>1</sup>, I. Vlček<sup>1</sup>, J. Zobačová<sup>1</sup>

<sup>1</sup>Institute of Scientific Instruments of the CAS, Královopolská 147, 61264 Brno, Czech Republic

\*e-mail: Libor.Dupak@isibrno.cz, URL: ebt.isibrno.cz

In vacuum technology, and especially in UHV, we often encounter the necessity of joining parts of various metals in combination with the demand for perfect vacuum tightness, cleanness of joints and minimum deformations. Electron beam welding [1, 2] belongs to the best technologies capable of fulfilling such requirements.

The principle of electron beam welding is based on the transfer of the kinetic energy of the incident accelerated electrons to the welded material in the form of heat. The temperature in the spot rises with the beam power density. At power densities as high as  $10^4 - 10^6$  W/mm<sup>2</sup>, the melted material at the center of the focal point evaporates. This produces a vapor capillary surrounded by melted material that allows the beam to penetrate deeper and melt more material. The speed of the penetration can be much higher than the heat transfer by conduction into the surrounding material. This results in narrow melted area and typical knife-like profile of the weld (Figure 1). Thanks to this effect the thermal deformations of welded pieces are highly reduced to almost none. Small heat affected zone also allows welding near heat sensitive parts like sensors, ceramic feed-throughs (Figure 2) and brazed joints.

By electron beam welding, wide range of materials can be welded, from alloy and stainless steels, copper, aluminum and nickel alloys to refractory metals (tungsten, molybdenum). It is also possible to weld dissimilar metals even with very different properties. For example, combinations like Al-Cu, Al-Ti, stainless steel-tungsten or molybdenum and others can be joined, even though other welding methods lead to fragile welds.

As the electron beam is easy to control, either by focusing or by deflection, it is possible to guide the beam's energy to a specific spot on the work-piece with ease. Using computer control, the welding can be performed even with very complex trajectory. The beam can also "jump" very quickly among several points and weld at several places at the same time (multi-beam welding) thus reducing thermal stress further.

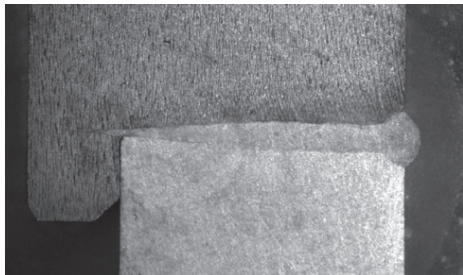


**Figure 1** Weld of alloy and stainless steel, 6 mm deep.



**Figure 2** Feedthroughs welded into flange, diameter cca 10 cm.

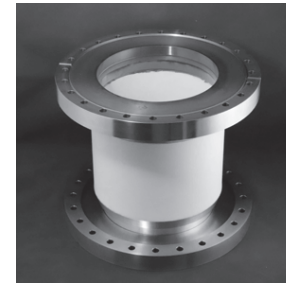


**Figure 3** Welded flanges to ceramic insulator, DN 200.

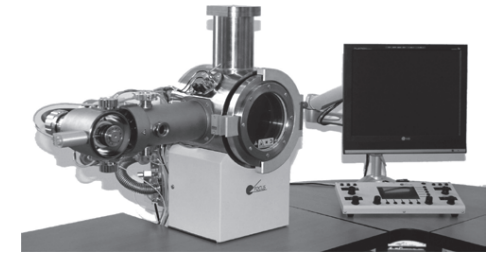


**Figure 4** Electron beam welder MEBW-60/2 developed at ISI Brno.

Disadvantage of the technology is the need for vacuum, which puts limitation on the size of the welded components. It also increases the cost of the equipment. However, the vacuum remelting in the weld zone produces high quality welds with high strength. It also allows welding of reactive metals (e.g. titanium, zirconium or tantalum) as vacuum serves better than shielding gas.

The beginnings of the electron beam welding at Institute of Scientific Instruments Brno are closely connected to development in vacuum and cryogenic technologies [3]. We are already the third generation of researchers in the field of electron beam welding at ISI. Some of the recent tasks were parts of electron microscopes like feedthroughs, membrane bellows, insulators (Figure 3) and other precise parts. Other fields of research like high strength welds of dissimilar metals (steels, inconel, nimonic, niobium, titanium, etc.) are connected to automotive, aerospace, power production and other branches of industry but also for other research organizations.

At the moment we have two devices at our disposal. The first one is an older ES-2U that has been recently upgraded with a new vacuum system. The working chamber is about 50 cm in diameter. Together with three manipulators it allows us to weld bigger pieces in various positions. The new electronics is also planned to give us the possibilities of advanced welding techniques like the second welder has.

The second welder is modernized desktop electron beam welder MEBW-60/2 (Figure 4, [4]). Its small working chamber (about 20 cm diameter) allows very short pumping times (about 2-3 minutes). However, despite its small dimensions, it is still very versatile, as the e-gun can be mounted in several configurations and thus allows welding of different types of welds. Sets of various extenders also give us the possibility of welding bigger or longer pieces than that would normally fit into the chamber (Figure 5).

The new improved electronics is completely digitized and allows easy control from computer. The power source allows operation up to 60 kV. The beam power is up to 2 kW (33 mA at 60 kV or 40 mA at 50 kV). This allows us to weld up to 15 mm of stainless steel. On the other hand, with precise control of the beam power and the welding spot we can do very precise

welding (tenths of millimeter), e.g. tiny pieces, membranes, thin wall tubes, and foils (Figure 6).

The control software allows image acquisition (SEM/TV mode), arbitrary shaped welding (welding over trajectory), micro-engraving techniques and other functions. The electron beam welder is also capable of drilling small holes (tenths of millimeter) into metal foils. It is also possible to drill holes or cuts up to several mm in diameter into quartz glass or ceramics [5].

#### References:

- [1] Schultz, H. Elektronenstrahlschweißen. DVS-Verlag, Düsseldorf, 2000.
- [2] Dupák L., Electron Beam Welding: Principles and Applications, Recent Trends in Charged Particle Optics 2008, p. 27-28.
- [3] Zobač M., Vlček I., Electron Beam Welding in ISI Brno: Past&Present, Recent Trends in Charged Particle Optics 2008, p. 109-110.
- [4] Vlček I., Desktop electron beam welder MEBW-60/52 (Czech), JMO, 53 (2008) 27-30.
- [5] Dupák, L, Zobač, M.: Electron Beam Micromachining. Recent Trends Charged Particle Optics 2008 2006. s. 15-16.

The research was supported by Ministry of Education, Youth and Sports of the Czech Republic (project LO1212). The research infrastructure was funded by Ministry of Education, Youth and Sports of the Czech Republic and European Commission (project CZ.1.05/2.1.00/01.0017) and by the Czech Academy of Sciences (project RVO:68081731).



**Figure 5** Welded heat exchanger, 4 m length, diameter of welds 3 mm.

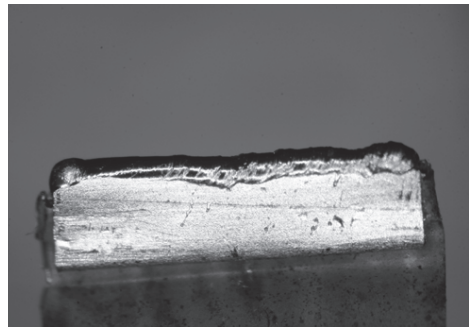


**Figure 6** Weld Ni (0.1 mm) and Cu (0.015 mm) foils, 4 mm long.

## MULTI-REFLECTION TIME-OF-FLIGHT ION TRAP WITH ISOCHRONOUS DRIFT

D. Grinfeld\*, C. Hock, H. Stewart, A. Makarov

Thermo Fisher Scientific, Hanna-Kunath Str. 11, DE-28199, Bremen, Germany

\*e-mail: dmitry.grinfeld@thermofisher.com

Time-of-flight mass spectrometry (ToF MS) employs separation of ions by mass-to-charge ratios during their motion in an electrostatic field from an ion source to a time-resolving impingement detector. The fundamental property of electrostatic fields is that the charged particles share the same paths but have mass-dependent times of flight, so that the detector's response represents the mass spectrum of a pulsed ion bunch. The mass resolving power of a ToF MS instrument is  $T/2\delta T$  where  $T$  is the flight time (for a specific mass-to-charge ratio) and  $\delta T$  is its dispersion. This formula suggests two ways to improve the mass resolving power: (i) increasing the total flight length and (ii) compensation of ToF aberrations giving rise to dispersion. Reflectron-type mass analyzers [1] exploit both of these opportunities – the ion mirror doubles the flight length and simultaneously compensates the chromatic ToF errors. To further improve mass resolving power, ToF MS instruments may be adapted for a multi-folded ion path [2]. It was proposed [3] to use a pair of opposing parallel elongated electrostatic mirrors to make the ions oscillate between them in an isochronous potential well  $\varphi_0(z)$  and simultaneously drift freely in the elongation direction  $y$ . An ion bunch injected with an angular spread  $\vartheta_{min} < \vartheta < \vartheta_{max} \ll 1$  expands quickly, however, and irreversibly overlaps after just a few reflections. This problem was addressed in [4-6] with incorporating drift-dependent field perturbations  $\delta\varphi(z, y)$ , which, however, tend to break the isochronism and make the time of flight  $\vartheta$ -dependent. In this research we theoretically consider the drift control schemes with two requirements: (1) spatial re-bunching of the ion trajectories and (2) ToF isochronicity for the ion trajectories with different injection angles.

Assume  $\varphi_0(0) = \delta\varphi(z, 0) = 0$  and the acceleration voltage  $U_0$  defines the ion's full energy when oscillating between two mirrors. The initial kinetic energy of the drift is  $eU_0 \sin^2 \vartheta$ . The following integral defines the *action* for an ion of mass  $m$ , charge  $e$ , and energy  $\varepsilon_z$ , that makes a full  $z$ -oscillation at a drift location  $y$ :

$$J(\varepsilon_z, y) = \sqrt{8m} \int \sqrt{\varepsilon_z - e\varphi(z, y)} dz \cong J_0(\varepsilon_z) + \Delta J(\varepsilon_z, y)$$

where  $J_0$  is the action is the unperturbed field and  $\Delta J$  is the first order perturbation:

$$J_0(\varepsilon_z) = \sqrt{8m} \int_{z_1}^{z_2} \sqrt{\varepsilon_z - e\varphi_0(z)} dz, \quad \Delta J(\varepsilon_z, y) = -\sqrt{2me} \int_{z_1}^{z_2} \frac{\delta\varphi(z, y) dz}{\sqrt{\varepsilon_z - e\varphi_0(z)}}$$

The integrals are calculated between the two turning points  $z_{1,2}(\varepsilon_z)$ . As the potential  $\varphi_0$  is assumed isochronous, the unperturbed period  $T_0 = J'_0(\varepsilon_z)$  constant at least in a range of energies containing  $eU_0$ . The derivative  $\Delta T(\varepsilon_z, y) = \partial\Delta J/\partial\varepsilon_z$  defines the period's perturbation.

The action is an adiabatic integral of motion whose differential  $T_0 d\varepsilon_z + J'_y dy = 0$  on the trajectories. Keeping the energy conservation  $d\varepsilon_z = -d\varepsilon_y$  in mind, where  $\varepsilon_y = m\dot{y}^2/2$  is the

kinetic energy's drift component, we arrive at the drift equation  $d\varepsilon_y/dy = -e\nabla_y\Phi(y)$ . The function  $\Phi(y) = -\Delta J(eU_0, y)/eT_0$  represents the effective drift potential. We shall assume that there is a drift turning point  $y_D(\vartheta)$  defined by the equation  $\Phi(y_D) = eU_0 \sin^2 \vartheta$ , where the drift is reversed and the spatial spread is reduced on the return path in analogy with the energy focusing in a reflectron. The perturbation  $\delta\varphi(z, y)$  can be engineered to make  $\Phi(y)$  isochronous, in which the return time

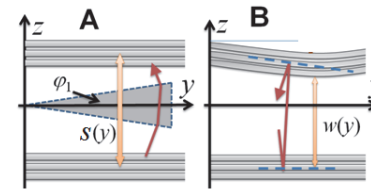
$$T_D(\vartheta) = \frac{T_0}{W_0} \int_0^{y_D(\vartheta)} \frac{\sqrt{U_0}}{\sqrt{U_0 \sin^2 \vartheta - \Phi(y)}} dy, \quad W_0 = T_0 \sqrt{\frac{eU_0}{2m}}$$

will be confined in the interval  $(K_0 \pm 0.5)T_0$  where  $K_0$  is a number of oscillations after which the ion bunch should be re-focused without overlapping with adjacent ones. The parameter  $W_0$  is the effective distance between the mirrors. The side effect of the potential perturbation  $\delta\varphi(z, y)$  consists in the  $y$ -dependent period deviation  $\Delta T(y) = \partial\Delta J(\varepsilon_z, y)/\partial\varepsilon_z$ , which makes the full time of flight function of the injection angle:

$$\tau(\vartheta) = T(\vartheta) - K_0 T_0 = \frac{1}{W_0} \int_0^{y_D(\vartheta)} \frac{\sqrt{U_0}}{\sqrt{U_0 \sin^2 \vartheta - \Phi(y)}} \frac{\partial\Delta J(y)}{\partial\varepsilon_z} dy$$

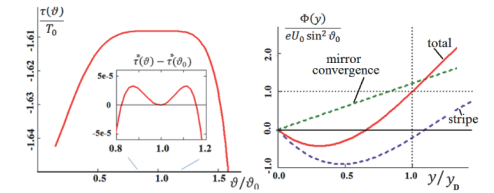
Therefore, the field perturbation should be also optimized to give a plateau to  $\tau(\vartheta)$ .

Fig. 1 shows two methods to generate an effective drift potential with (A) an electrically biased 'stripe',  $\varphi_1 \ll U_0$ , or (B) a slight mirror non-parallelism with effective inter-mirror distance  $w(y) \leq W_0$ . It may be shown that these two methods result in the period errors with opposite signs, i.e.  $\Delta T(y) = \pm T_0 \Phi(y)/2U_0$  where plus comes in variant A and minus in variant B. A combination of the two methods allows optimization of a system with two *non-parallel* ion mirrors and a specially shaped stripe to make the multitude of reflections practically isochronous within a 40% range of injection angles. The numerical results (Fig. 2, normalized) may be used to confine a many meters long ion flight length in a table-size high-resolution mass spectrometer.



**Figure 1.** Variant of drift control.

A: an electrically biased stripe,  
B: non parallel mirrors.



**Figure 2.** Optimized isochronous system with ion mirrors converging at a small angle and a 'stripe' with a specific shape and bias.

References:

- [1] Mamyrin B., Int. J. Mass Spectrom. **206** (2001), p. 251-66.
- [2] Wollnik H. and Przewloka M., Int. J. Mass. Spectrom. Ion Proc. **96** (1990), p 267-74.
- [3] Nazarenko L.M. et al. / Soviet Patent No. SU1725289 (1989)
- [4] Yavor M., Verentchikov A. et al., Physics Procedia **1** (2008), p. 391-400
- [5] Ristroph T., Flory C.A., US patent application US2011/0168880 A1 (2011).
- [6] Sudakov M. and Kumashiro S., Nucl. Instr. Meth Phys Res. **A645** (2011), p. 210-5

## OPTIMIZATION OF ELECTROSTATIC LENS SYSTEMS USING GENETIC ALGORITHMS

N. Hesam Mahmoudi Nezhad<sup>1\*</sup>, M. Ghaffarian Niasar<sup>2</sup>, A. Mohammadi Gheidari<sup>1</sup>, T. Janssen<sup>3</sup>, C.W. Hagen<sup>1</sup>, P.Kruit<sup>1</sup>

<sup>1</sup>Delft University of Technology, Fac. Appl. Sciences, Dept. Imaging Physics, Charged Particle Optics Group, Lorentzweg 1, 2628 CJ Delft, The Netherlands

<sup>2</sup>Delft University of Technology, Faculty of Electrical Engineering, DC systems, Energy conversion and Storage, Mekelweg 4, 2628 CD Delft, The Netherlands

<sup>3</sup>Delft University of Technology, Faculty of Applied Mathematics, Optimization, Mourik Broekmanweg 6, 2628 XE, The Netherlands

\*e-mail: n.hesammahmoudinezhad@tudelft.nl

To optimize the design of a system of electrostatic lenses can be quite challenging. Especially when many lens electrodes are involved, the number of design parameters, such as electrode thickness, radius, gaps between electrodes and voltage, increases rapidly. Therefore, it would be really helpful when optimization routines can be used. There have been some attempts to develop optimization programs, such as Szilagy et al. [1] and Adriaanse et al. [2], but they used to be not very accurate. In the meantime, computers have become much more powerful, making it attractive to revisit the problem. In this work we apply a Genetic Algorithm [3] for the optimization, and MATLAB was chosen for coding. We started out to calculate the axial potential using the so-called Second Order Electrode Method (SOEM) [2]. In this method, for rotationally symmetrical systems, the solution of the Laplace equation is approximated by omitting terms above third order:

$$\varphi(r, z) \approx \varphi(0, z) - r^2 \varphi''(r, z)/4$$

By applying a cubic spline approximation, the potential can be calculated all along the optical axis by solving a linear equation of  $a_i \varphi_{i-1} + b_i \varphi_i + c_i \varphi_{i+1} = d_i$ , where the coefficients  $a_i$ ,  $b_i$ ,  $c_i$  and  $d_i$  are only dependent on the geometry of the lenses and their potentials. This way the axial potential can be calculated very fast (~0.1 sec). Ray tracing is done using a Runge-Kutta approximation [4] and the spherical and chromatic aberrations are calculated from aberration integrals [5]. The optimization, for instance, minimizes an objective function, such as the probe size of a focused beam of charged particles, and constraints can be added, such as the position of the focus plane and maximum allowable fields between electrodes.

To evaluate this approach we compared, for a three-electrode design (see Figure 1), the calculated axial potential with the potential calculated using the electron optics design package EOD [6] as well as the potential calculated with COMSOL [7]. The result is shown in Figure 2. At first sight, the potentials compare quite well, but when the first and second derivatives are plotted (Figure 3) the differences become clear. These will influence the aberrations and thus the probe size of the focused beam, i.e. the objective function. Although EOD and COMSOL clearly give a more reliable axial potential than SOEM, the latter is much faster.

To improve the accuracy, we investigated the possibility to integrate COMSOL in our optimization routine. This way the potential calculation and the objective function calculation

is more accurate, but the optimization becomes more time consuming. We looked into ways to improve on the calculation time. As a compromise, we first do a rough optimization using the SOEM approach, resulting in a few approximately optimized systems. Then, using the parameters of the systems found, a new set of systems was defined using a small range of values around these parameters. Then the more accurate, but somewhat slower, COMSOL-based optimization was applied to this set of systems. We have tested our method on three-electrode systems. We succeeded to very accurately optimize these systems within a few hours, with the electrode radii and gaps and voltages as free parameters, and the focus position as a constraint. We are working to expand our work for a larger number of electrodes. We will present the optimization method and some initial results at the conference.

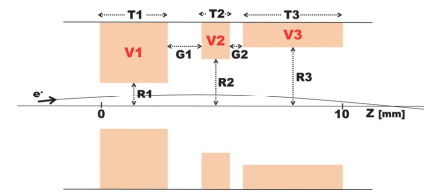


**Figure 1.** Schematic drawing of the three electrode lens design

([T1,T2,T3,R1,R2,R3,G1,G2] = [2.9,1.2,4.3,1,2,2.5,1.2,0.6] mm)

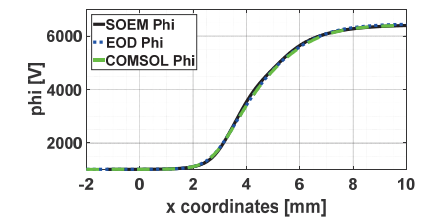


**Figure 2.** The axial potential for the system of Figure 1, with voltages [V1,V2,V3] = [1000,4913,6421] volts, calculated with SOEM, and simulated with EOD and COMSOL.

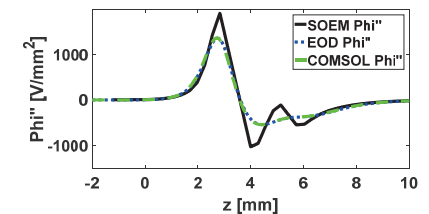
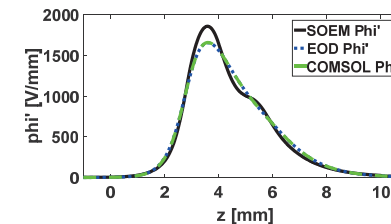


**Figure 3.** Left, the first derivative of the potentials in Figure 2, and right, the second derivatives.

### References:

- [1] M. Szilagi, Yakowitz and M. Duff, Appl. Phys. Lett. 44, pp. 7-9, 1984.
- [2] J.P. Adriaanse, H.W.G Van der Steen and J.E. Barth, J.Vac. Sci. Technol. B7, pp. 651-666, 1989.
- [3] Mitchell Melanie, An Introduction to Genetic Algorithms, The MIT Press, Cambridge, London, 1999.
- [4] W.H. Press et al., Numerical Recipes, Cambridge University, Cambridge, 1986.
- [5] H. Rose, Geometrical Charged Particle Optics, 2nd edition, Springer, 2013.
- [6] B. Lencova and J. Zlamal, EOD (Electron Optical Design package), version 4.008.
- [7] www.comsol.com, COMSOL Multiphysics, version 5.3a / 2017.

## STRUCTURE INVESTIGATION OF HYDROGELS USING A CRYO-SEM

K. Adamkova<sup>1</sup>, K. Hrubanova<sup>1</sup>, O. Samek<sup>1</sup>, M. Trudicova<sup>2</sup>, P. Sedlacek<sup>2</sup>, V. Krzyzanek<sup>1</sup>

<sup>1</sup> Institute of Scientific Instruments of the CAS, v. v. i., Kralovopolska 147, 612 64, Brno, Czech Republic

<sup>2</sup> Brno University of Technology, FCH, Purkynova 464/118, 612 00, Brno, Czech Republic  
\*e-mail: krzyzanek@isibrno.cz

Hydrogels can be characterized as elastic hydrophilic polymer chains connected in network which are able to swell notably when exposed to aqueous media by absorbing considerable amounts of water. Besides being a constituent of living organisms, nowadays, there are various fields hydrated polymers (e.g. polyvinyl alcohol, collagen, and starch) can be utilized – in both biological and non-biological form. Classic examples of such applications are human health and cosmetics (contact lenses, wound healing dressings and artificial replacement tissues – skin, arterial grafts, cornea and spinal disc replacement), pharmacy (drug delivery systems), bioengineering, food industry, agriculture etc. [1]. Also, hydrogels can reversibly change their shape when being exposed to a temperature change.

The aim of this study is to examine and describe the ultrastructure of a selected hydrogel, namely hyaluronic acid (Fig 1) and agarose (Fig 2). Hyaluronic acid or hyaluronan is a linear polymer, composed of a repeating disaccharide that can be found in many living structures (e.g. extracellular matrix, synovial fluids and vitreous humour), where it has a structural function, as well as functions in cell proliferation, migration and differentiation. Hyaluronic acid can be employed in medical applications because of its viscosity, elasticity biocompatibility and biodegradability, and for it is able to pervade some particular tissues – e.g. in ophthalmological surgery (cataract), joint disease therapy (arthritis) and wound healing. Agarose is a hydrophilic polysaccharide with gelling properties in solution that can be obtained by extraction from marine red algae [1]. The agarose hydrogel is of high elasticity and comprises a thick rigid network of agarose chains with incorporated large water pores. This polymer is similar to living tissue and extracellular matrix fluid, and for ability to penetrate to it is used for biophysical phenomena. Agarose gels can be employed in food sciences, pharmacology (drug delivery systems), tissue engineering, genetics etc.

Here we presented structural concentration dependant differences which were evaluated by means of cryo-SEM imaging [2]. Moreover, several types of low temperature sample preparation protocols were compared. Especially, the effect of various freeze-etching times was investigated [3]. In addition, besides the ultrastructural characterization by cryo-SEM the chemical analysis of selected samples was performed by Raman spectroscopy. Raman spectroscopy is an optical method enabling chemical analysis of a microscopic sample by laser beam [4]. Fast and reliable monitoring and identification of chemical additives specific for selected hydrogels is performed by a library of spectra in the so-called fingerprint area. This is a spectral region unique to each chemical component of hydrogels. Our experimental results can contribute to the widening of knowledge about the influence of hydrogel composition on its structure. The comparison of selected techniques can be recognized as suitable for the structural and chemical analysis applicable to other hydrogel systems as well.

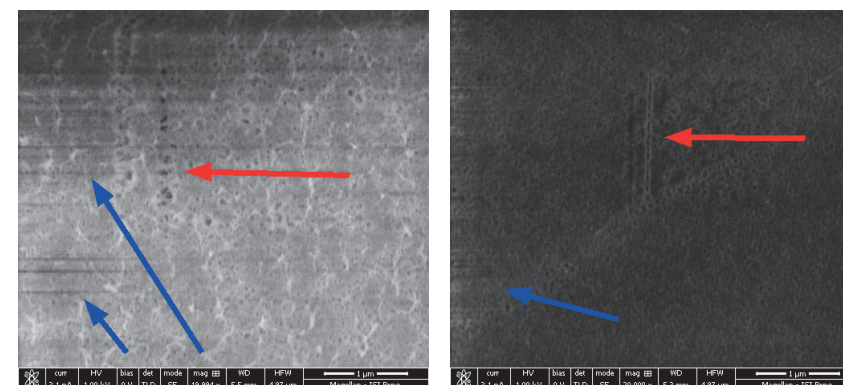


**Figure 1** HA hydrogel mixed with 50mM septonex. Red arrows mark the beam damage, blue arrows the charging effect.

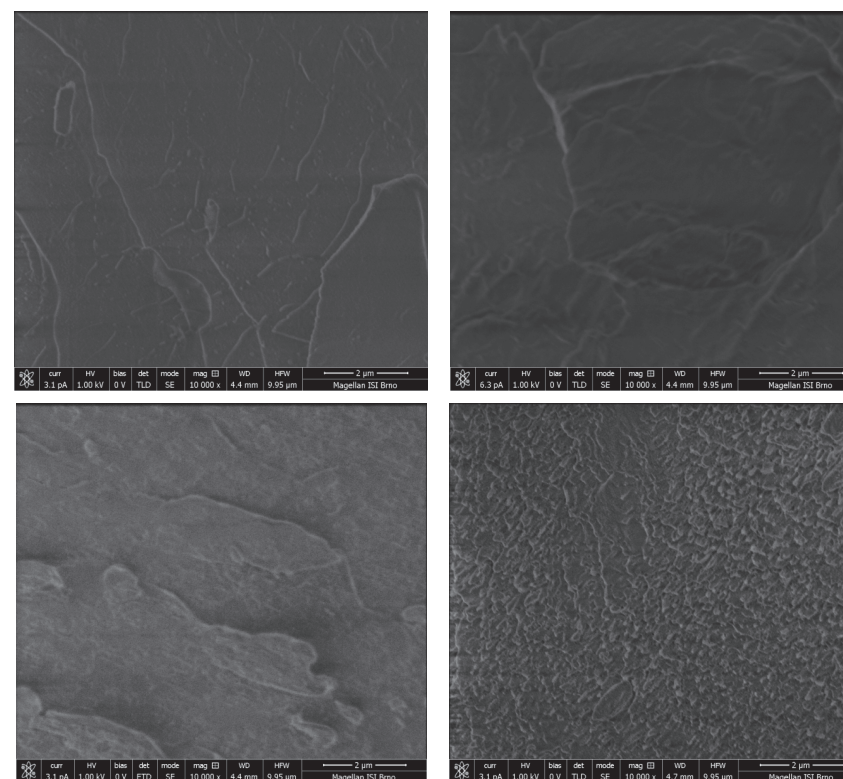


**Figure 2** Agarose hydrogel concentrations a) 0.5 %, b) 1.0 %, c) 2.0 % and d) 4.0 %

**Acknowledgement**

The research was supported by the Czech Science Foundation (projects GA16-12477S and 17-15451S), Ministry of Education, Youth and Sports of the Czech Republic (project LO1212). The research infrastructure was funded by Ministry of Education, Youth and Sports of the Czech Republic and European Commission (project CZ.1.05/2.1.00/01.0017) and by the Czech Academy of Sciences (project RVO:68081731).

**References:**

- [1] Pekar M. Hydrogels with Micellar Hydrophobic (Nano)Domains; *Front. Mater.*, 28 January 2015, volume 1, p 35.
- [2] Kuo, J. *Electron Microscopy – Methods and Protocols*; Springer Science & Business Media. 2007.
- [3] Hrubanova K., Nebesarova, J., Ruzicka, F., Krzyzanek, V. The innovation of cryo-SEM freeze-fracturing methodology demonstrated on high pressure frozen biofilm: *Micron* 2018, volume 110, p. 28–35.
- [4] Samek, O., Jonáš, A., Pilát, Z., Zemánek, P., Nedbal, L., Tríska, J., Kotas, P., Trtílek, M., Raman Microspectroscopy of Individual Algal Cells: Sensing Unsaturation of Storage Lipids *in vivo*; *Sensors*, 2010. volume 10, p. 8635–8651.

## MONOCHROMATIZING WITHOUT FILTERING: PROPOSAL FOR A MICROWAVE BASED LOW LOSS MONOCHROMATOR FOR S(T)EM

R. Janzen<sup>1</sup>

<sup>1</sup>Janzen Consulting, Heidelberger Str. 52, 64673 Zwingenberg, Germany  
\*e-mail: info@dr-janzen.de

Commonly used monochromators are energy filters. The majority of the particles with undesired energies is removed. Thus the output current diminishes with increasing degree of monochromatization. Monochromators in the original meaning of the word that would affect the energy of the particles by an energy selective acceleration can only be realized by use of dynamic fields.

Dynamic field applications without exception involve a condition between the phase of the dynamic field and the entrance point of time of the particle into the field. If this condition is fulfilled, the dynamic field application works exactly. Unfortunately the width of the time interval where the condition is fulfilled is mathematically zero. Thus up to now dynamic field applications in charged particle optics limit themselves to a small time interval around the periodically recurring point of optimum phase where the condition is fulfilled to a good approximation. For that purpose bunches are formed around the optimum phase point. Unfortunately bunch forming suffers from Liouville's theorem: The product of the bunch length and the energy spread within it is a constant.

In this work a concept is presented that circumvents this dilemma. A circularly polarized standing wave deflects the charged particle beam to a rotating orbital feeding the particles into a propagating wave that rotates within a toroidal wave guide (see figure 1). The circular deflection supplies a time coding. The entrance point of time of any particle is locked to its azimuthal position. Provided that the deflecting field and the rotating propagating wave (denoted by working field in the following) are synchronized correctly the optimum phase condition is fulfilled exactly and constantly. Time uncertainty vanishes within the limits of technical & practical implementing of the concept. The working field may be cascaded. It can be used for a large variety of applications such as monochromatizing, spread inversion (and not covered by this talk: time focusing, accelerating, pulse forming, spread amplification, and aberration correction). In the end the spiral orbital may be focused to an inverse circular deflector that undoes the action of the first circular deflector and thus leads the particles back to the original axis (see Figure 2.).

A monochromator based on circular deflection was demonstrated to work by computer simulation assuming theoretically ideal TE<sub>10</sub> mode microwaves as dynamic fields. The energy spread vanishes within the limits of technical & practical implementing of the concept without any loss of current. The working field acts like a cool thermodynamic reservoir absorbing heat from the electrons.

In this talk I focus on some details of circular deflection. Furthermore a simplified type of the circular deflection based monochromator for probe forming applications is proposed. In this

special case it is possible to economize on the undoing circular deflector by combining the crossing (of the deflected axis with the original axis) with an image of the electron source.

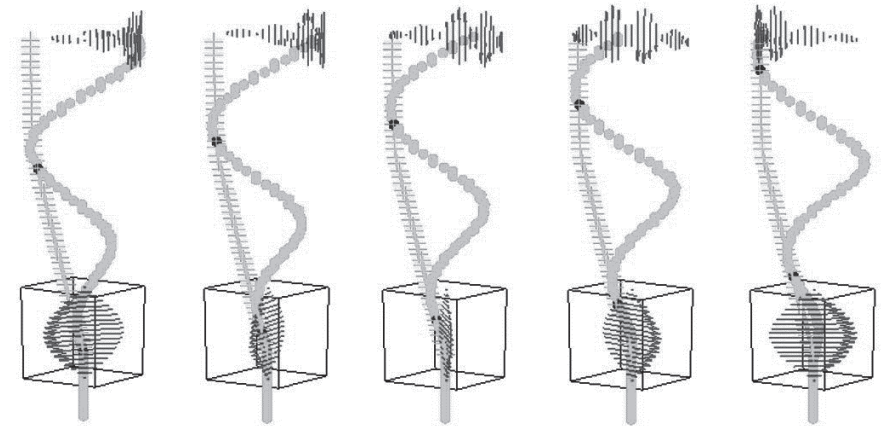


**Figure 1** Five snapshots of an animated schematic drawing illustrating the principle of a typical circular deflection application. The circular deflector wave is a circularly polarized standing wave within a cubic resonator. The electric field vector (shown by the lower group of arrows) rotates, always pointing perpendicularly to the direction of motion of the electrons (which is in this figure assumed to point upwards). The working field is represented by the upper group of arrows. It is a propagating wave that is rotating within a toroidal resonator (not shown).

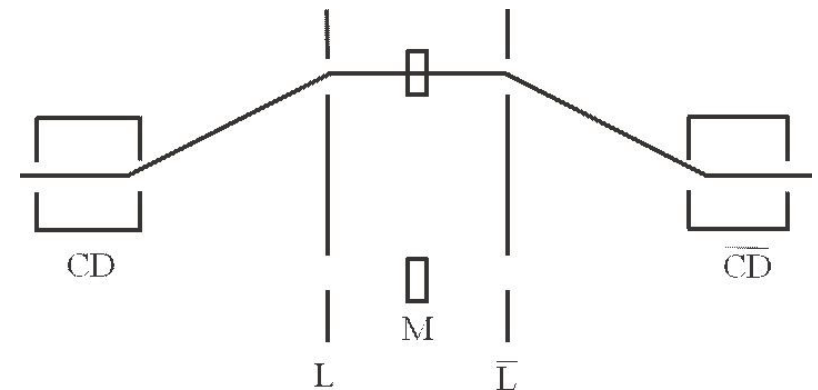


**Figure 2** Schematic drawing (cross sectional view) of a simplified monochromator design based on circular deflection. Note that in difference to figure 1 the electrons are assumed to move from left to right. They are deflected by the circular deflector CD, focused by some lens like element L, monochromatized by the working field inside the toroidal resonator M, focused again and deflected by an 'undoing' circular deflector in the end.

## MAPPING MATERIAL SCIENCE PROPERTIES ON THE NANOSCALE BY SECONDARY ELECTRON ENERGY SPECTROMETERS IN THE SEM

A. Khursheed\*, H. Weiding, and A. Banerjee

Department of Electrical and Computer Engineering, National University of Singapore, 4 Engineering Drive 3, Singapore 117583

\*e-mail: eleka@nus.edu.sg

Over a period of around 20 years, approximately between 1970 to 1990, a wide variety of Secondary Electron (SE) energy spectrometer designs were integrated into the Scanning Electron Microscope (SEM) for the purpose of Integrated Circuit Electron Beam Testing Circuits [1,2]. These SE energy spectrometers enabled SEMs to quantitatively monitor changes in surface potential, and they were combined with different types of objective lenses, conventional magnetic ones, the retarding field type, and the magnetic immersion type. However, demand for Electron Beam Test equipment sharply fell after Integrated Circuits started to have ground cover planes, and now days, the use of SE energy spectrometers with SEMs is rare.

At present, SEM manufacturer's do not make SE energy spectrometer attachment accessories available, and it is up to individual researchers to make them for themselves. However, recent research shows that there is a need to use SE energy spectrometers with SEMs for material science applications. Figure 1 shows a band-pass second-order electrostatic toroidal SE energy spectrometer attachment system for SEMs [3], and Fig. 2 presents experimental SE energy spectral signals captured from it on a test specimen having *p*-doped stripes in a *n*-doped silicon substrate, which was etched and then allowed to grow a 15 nm native oxide layer under controlled conditions. The results demonstrate how the SE energy spectral signal changes shape according to the dopant regions and the presence of the native oxide layer. These results point towards the development of a new possible method for mapping material science properties on the nano-scale in the SEM.

This talk will review different types of SE energy spectrometer designs, highlighting those that are most suitable to operate as SEM attachments, and it will also give some examples of the kinds of contrast mechanisms that can be monitored by them.

### References

- [1] J. T. L. Thong, *Electron Beam Testing Technology*, ch. 5, Plenum Press, 1993.
- [2] A. Khursheed, *Scanning Electron Microscope Optics and Spectrometers*, ch. 5, World Scientific, 2011.
- [3] A. Khursheed and H. Hoang, *Ultramicroscopy*, Vol. 109, pp104-110.

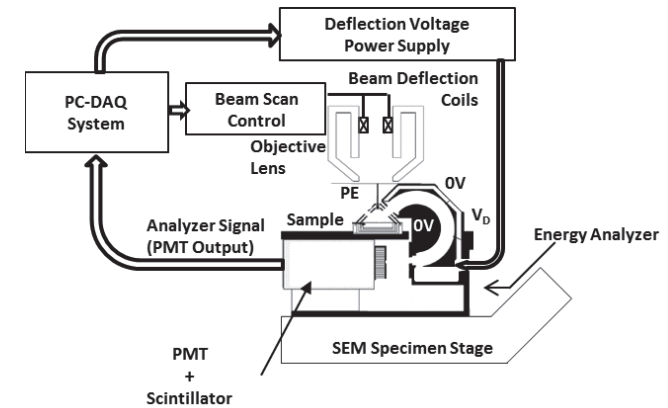


Figure 1: A second-order toroidal SE energy spectrometer inside a SEM

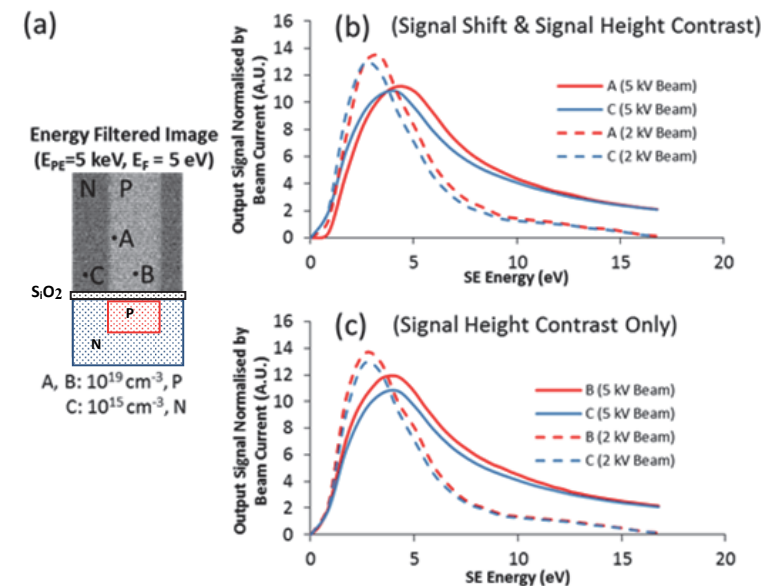


Figure 2: Experimental results on a *p*-doped stripe in a *n*-doped silicon substrate test specimen in the presence of a 15 nm native oxide layer

(a) SEM image (b) At the stripe edge (point A) (c) At the stripe centre (point B)

## FIELD EMISSION FROM $W_5O_{14}$ NANOWIRES

M. Saqib<sup>1</sup>, A. Knápek<sup>2\*</sup>, J. Jelenc<sup>1</sup>, L. Pirker<sup>1</sup>

<sup>1</sup>Solid State Physics Department, Jozef Stefan Institute, 1000 Ljubljana, Slovenia

<sup>2</sup>Institute of the Scientific Instruments of the Czech Academy of Sciences, v. v. i., Královopolská 147, 612 64 Brno, Czech Republic

\*e-mail: knapek@isibrno.cz

The  $W_5O_{14}$  (O/W=2.8) nanowires are metallic oxides with specific resistivity of  $25 \mu\Omega\text{cm}$  and diameters below 100 nm [1]. They were synthesized by iodine transport method using nickel as a growth promoter and  $WO_3$  as source of tungsten and oxygen. The field emission characteristics of single nanowires [2] and the films composed of these nanowires have been reported [3]. The emitting current densities up to  $6.4 \text{ mA/cm}^2$  have been obtained at relatively low average electric field of about  $3 \text{ V}/\mu\text{m}$ . The samples were allowed to emit for more than 100 hours without showing significant decays of the emitting current and without substantial current oscillations. Here, we present field emission properties of single  $W_5O_{14}$  nanowires exposed to two ranges of average electric fields ( $0.7\text{--}0.85 \text{ V}/\mu\text{m}$  and up to  $37\text{--}39 \text{ V}/\mu\text{m}$ ).

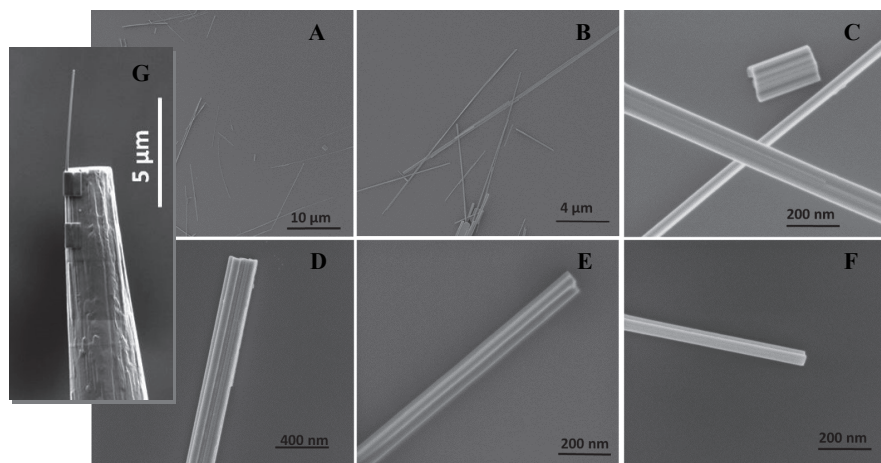


**Figure 1** Scanning electron microscopy of the  $W_5O_{14}$  nanowires (insets A-F). Bonded wire is illustrated in an inset G; a single nanowire is bonded on a tungsten tip.

Work function was measured on a single nanowire by Kelvin probe using non-contact atomic force microscopy. Decrease of the work function at the longitudinal terminations of the nanowires and along surface corrugations was observed. Contact atomic force microscopy using conductive tip has shown higher specific conductance at these sites, which could represent the emission sites. The work function values of the  $W_5O_{14}$  nanowires were found lower ( $4.29\text{--}4.34 \text{ eV}$ ) than for a  $W_{18}O_{49}$  nanowires ( $4.55 \text{ eV}$ ) or for pure tungsten ( $4.47 \text{ eV}$ ).

Field emission properties of bonded  $W_5O_{14}$  nanowires (Fig. 1) have been evaluated both in STM mode and in a triode configuration [4] using extracting electrode as it is illustrated in Fig. 2.

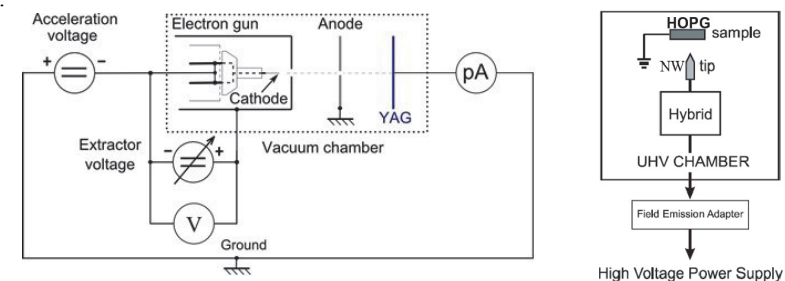


**Figure 2** (left) Measurement set-up based on original Müller's field emission microscope- the triode configuration; (right) the STM (diode) configuration intended for imaging tests.

The results of a two various samples in the STM mode yielded I-V characteristics and a Fowler-Nordheim plot proving a presence of the quantum tunnelling (Fig. 3). Measurements in the triode mode have been additionally used for determination of the field enhancement factor and long-time stability of the beam.

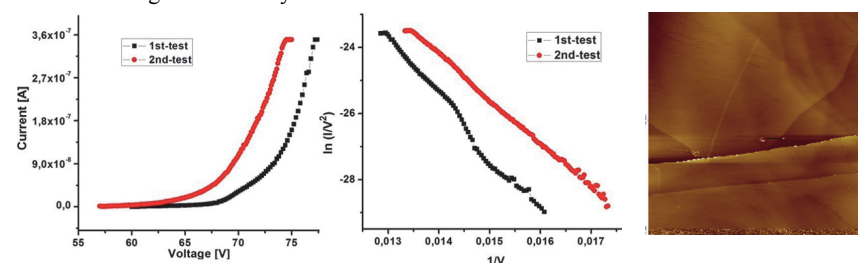


**Figure 3** Field emission measurements of  $W_5O_{14}$  nanowires in the STM mode (from the left): 1) I-V characteristics, 2) Fowler-Nordheim plot and 3) the STM image of HOPG sample obtained by the nanowire at the voltage = 1 V and current = 0.1 nA.

### Acknowledgments

The work was financially supported from the European Commission for the Marie Curie Initial Training Network (ITN) SIMDALEE2: Grant No. 606988 under FP7- PEOPLE-2013-ITN). The research was also supported by the Technology Agency of the Czech Republic project no. TE01020118, the MEYS CR (LO1212), its infrastructure by the MEYS CR and the EC (CZ.1.05/2.1.00/01.0017) and by the CAS(RVO:68081731).

### References:

- [1] M. Remškar et al., *Adv. Funct. Mater.* **117** (2007) p. 1974.
- [2] M. Žumer et al., *J. Phys. Chem. C* **112** (2008) p. 5250.
- [3] U. Gallo, et al., *Microelectron. Eng.* **170** (2017) p. 44.
- [4] A. Knápek, et al., *Microelectron. Eng.* **173** (2017), p. 46.

## HIDING E-BEAM EXPOSURE FIELDS BY DETERMINISTIC APERIODIC 2D PATTERNING

M. Horáček<sup>1</sup>, A. Knápek<sup>1</sup>, M. Matějka<sup>1</sup>, S. Krátký<sup>1</sup>, M. Urbánek<sup>2</sup>, F. Mika<sup>1</sup>, V. Kolařík<sup>1\*</sup>

<sup>1</sup>Institute of Scientific Instruments CAS, Královopolská 147, 612 64 Brno, Czech Republic

<sup>2</sup>Tomas Bata University, Centre of Polymer Systems, tř. Tomáše Bati 5678, 760 01 Zlín, CZ

\*e-mail: Vladimir.Kolarik@isibrno.cz

The high stability and good current homogeneity in the spot of the e-beam writer is crucial to the exposure quality, particularly in the case of large-area structures when gray-scale lithography is used. Even though the deflection field distortion is calibrated regularly and beam focus and beam astigmatism is dynamically corrected over the entire deflection field [1], [2], we can observe disturbances in the exposed relief.

Recently, we presented a method that makes use of e-beam exposure imperfection by introducing marginally visible high-frequency diffraction gratings of variable pitch that fill in separate orthogonal exposure fields [3]. The actually presented approach follows up our research on aperiodic arrangements of optical primitives [4], especially on the phyllotactic-like arrangement of sub-micron relief optical elements. This approach is extended from the diffraction element arrangement to the higher level of exposure fields arrangements.

The benchmarking DOVID (Diffractive Optically Variable Image Device), presented here as an example (Figure 1), makes use of the aperiodic arrangement at three different hierarchical levels. First, at the visual level, it consists of small visible planar objects (referenced hereafter as *seeds*), that are considered to be separated exposure fields (there is a movement of the patterning system stage between exposures of two adjacent seeds). This imposes an interesting task of the exposure field sequencing, as discussed below. Second, at the microscopic level, the aperiodic arrangement is used to determine two complementary areas filled in with a different diffractive patterns. Third, at the sub-micron level, the phyllotactic arrangement of diffractive elements is filling selected areas of the benchmarking image device (Figure 2).

The seeds in the arrangement are ordered along a primary spiral (*cf.* the coordinates model in [5], [6]); this is, by the way, the ordering used by the Nature. However, plants grow up slowly into this arrangement within an appropriate time span. The use of this sequencing while trying to mimic the final state of the arrangement seems to be quite inefficient. The summary path (which is related to the length of the primary spiral) linking all the seeds, depends not only on the number of seeds but also on the diameter of the arrangement. Schematically, this is illustrated in Figure 3 (left), denoted as 1D sequencing (as the ordering depends just on one independent variable, the primary angle in this case). One can imagine several approaches to decrease the discussed path that would make it possibly to be related only to the number of seeds. Actually, we are studying various approaches and we are trying to evaluate their tradeoff attributes. Here, we propose just one of them: a simple sequencing along the secondary (or derived) spirals that are visible in the arrangements of a medium size (approximately in the order of  $10e2$ – $10e4$ ). This type of sequencing is denoted as a 2D

sequencing, because the order of seeds goes along the first selected spiral from a selected secondary spiral set, then continuing along the second spiral of the mentioned set and so on, until all the seeds are ordered. Schematically, this 2D sequencing approach (with oversampling ration of 8:1) is depicted in the Figure 3 (right). In this simple example arrangement of 90 seeds, the full path is  $18.2c$  and  $4.0c$  in the case of 1D and 2D sequencing algorithm, respectively ( $c$  being the scale parameter of the aperiodic arrangement).

### References:

- [1] Bok J. *et al.*, J. Vac. Sci. Technol. B 31 (2013) 031603.
- [2] Bok J. *et al.*, Microelectronic Eng. 149 (2016) 117–124.
- [3] Kolařík V. *et al.*, Large–Area Gray–Scale Structures in E–Beam Writer versus Area Current Homogeneity and Deflection Uniformity, *In: Recent Trends in CPO and SPI, Proc's of 15<sup>th</sup> Int'l Seminar, 2016*, pp. 26–27.
- [4] Meluzin P, *et al.*, Some Other Gratings: Benchmarks for Large-Area E-Beam Nanopatterning, *In: Proc's of NANOCON, 6<sup>th</sup> Int'l Conference, 2014*, pp. 246–251.
- [5] Horáček M., *et al.*, Phyllotactic model linking macro and nano world, *In: Proc's of NANOCON, 8<sup>th</sup> Int'l Conference, 2016*, pp. 680–684.
- [6] Horáček M., *et al.*, Phyllotactic arrangements of Optical Elements, *In: Holography: Advances and Modern Trends V. (Proc's of SPIE 10233)*, 102331G, 2017.
- [7] The research was partially supported by the TACR (projects TE 01020233 and TG03010046), by MEYS CR (projects LO1212 and LO1504), its infrastructure by MEYS CR and EC (CZ.1.05/2.1.00/01.0017) and by CAS (RVO:68081731). The help and advices of Professor V. Tryhuk from the Brno University of Technology is highly appreciated.



Figure 1. Benchmarking DOVID: scheme / sample (left); specimen photo (right).

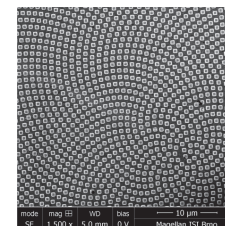


Figure 2. SEM detail: central part of the aperiodic arrangement.

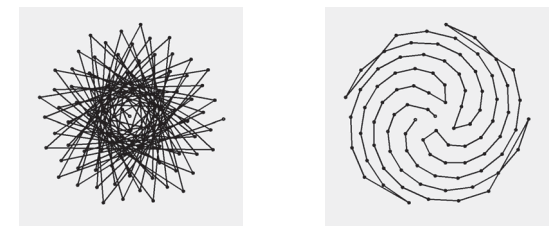


Figure 3. Sequencing algorithm: 1D sequencing (left); 2D sequencing (right).

## SEM LEEM – NEW TYPE OF MIRROR MICROSCOPE

V. Kolařík\*, P. Jánský and M. Mynář

Research laboratory, DELONG INSTRUMENTS a.s., Palackého třída 3019/153 b,  
612 00 Brno, Czech Republic

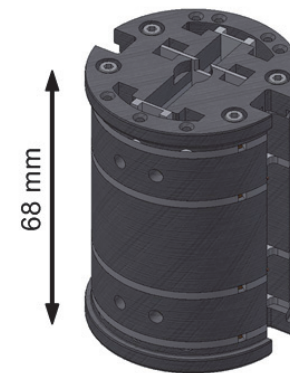
\*e-mail: vladimir.kolarik@delong.cz

LEEM is a well established method for the imaging of surfaces of materials using the impact of very slow electrons (down to zero energy - mirror microscopy). On the other hand, scanning electron microscopy has not consistently solved the detection of electrons in the mirror mode, i.e. in the incident energy range of 3 to 0 eV. In contrast to LEEM, which forms an integral image of the specimen surface and projects it onto an image screen, the scanning method relies on the detection of signals from individual pixels of the specimen. Since mirror microscopy can be realized only when using immersion lenses (either electrostatic, or combined with magnetic immersion), the detector has to capture the fast electrons with energies in principle of the same value as of the primary beam. Such “signal” electron beam moves back through the optical system very close to its optical axis and standard rotationally symmetric electron optics is in principle not able to provide their detection, and signal electrons return towards the source. The higher magnification is used, the more signal electrons are lost.

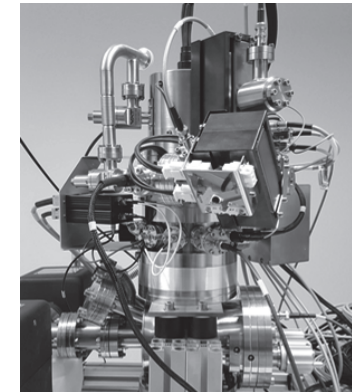
One solution is to use a rotationally asymmetric imaging and detection system that provides separate beam lines of primary and signal beams [1]. Any separation of these two beams requires their deviation from the optical axis. Given that the energy of signal electrons is high (close to the energy of the primary electrons) in the mirror microscopy mode, the deflection of signal electrons without influencing the primary beam quality is not a simple problem. One of possible solutions is to use a Wien filter, which does not change the trajectory of the primary beam, but only of the signal beam. However, only relatively small deflection angles of the signal beam are achievable for fast electrons. Larger deflection angles cause non-correctable defects of the primary beam. Another solution is to use magnetic prisms, which are able to compensate for any aberrations of the second order and also for energy dispersion in a symmetrical arrangement [2]. In the asymmetric arrangement, we can reach sufficiently large beam deflection angles ( $90^\circ$ ) having the energy dispersion on the order of units of micrometers per volt. By proper combination of homogeneous magnetic fields, the beam separator stigmatically transfers the primary beam back to the optical axis, while simultaneously allowing the detection of either energy non dispersed or dispersed signal electrons (for example of secondary or backscattered). Such a through-the-lens detector has zero optical power in the primary beam direction. In the “standard” operation mode with grounded specimen the through-the-lens detector can be (but does not have to be) switched off. The primary beam then passes through the detector rectilinearly. Signal electrons can be collected with any other standard detectors for SEM microscopy.

The first experiments verifying the correctness of the concept were made with the help of an assembly consisting of an (Schottky) electron source equipped with a magnetic gun lens followed by detector unit and electrostatic triode objective lens. The specimen is connected to a variable high voltage supply floating on the cathode potential. This arrangement allows to

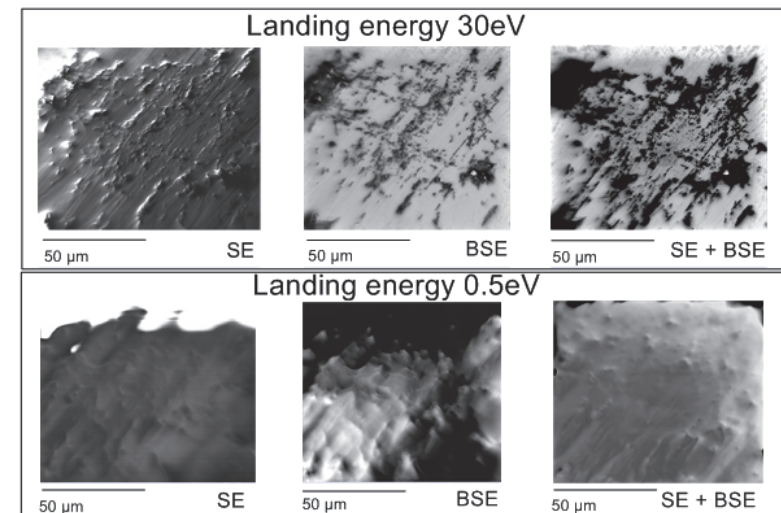
compensate the instability of the main high voltage supply in such a way that the incident energy remains well defined. Here we present the system with only electrostatic immersion objective lens. Experiments with a combination of electrostatic-magnetic immersion lens are under preparation. The results presented here are demonstrating the ability of the detector to distinguish between BSE and SE electrons for landing energies as low as 0.5 eV. The integral detector is mixing both signals and shows the mirror character of the image.



Model of the detector.



Experimental setup of the mirror microscope.



Micrographs demonstrating the energy selectivity of the detector. Even for landing energy 0.5 eV both SE and BSE electrons can be distinguished.

### References:

- [1] Kruit P., in *Advances in Optical and Electron Microscopy*, vol. 12, ed. by Mulvey T. (Academic, London, 1991), p. 93-137
- [2] Kolarik V., Mankos M. and Veneklasen L. H., *Optik* 87, No. 1 (1991) 1 – 12

## STEM MODES IN SEM

I. Konvalina\*, A. Paták, E. Mikmeková, F. Mika and I. Müllerová

Institute of Scientific Instruments of the CAS, v. v. i., Královopolská 147, 612 64, Brno, Czech Republic

\*e-mail: konvalina@isibrno.cz

The segmented semiconductor STEM detector in the Magellan 400 FEG SEM microscope (<https://www.fei.com/>) is used to detect transmitted electrons (TEs) and allows observing samples in four imaging modes. Two modes of objective lens, namely high resolution (HR) and ultra-high resolution (UHR), differ by their resolution and by the presence or absence of a magnetic field around the sample [1]. If the beam deceleration (BD) mode is chosen, then an electrostatic field around the sample is added and two further microscope modes HR + BD and UHR + BD, become available. Trajectories of TEs are studied with regard to their angular and energy distribution in each mode in this work.

There is no magnetic field around the sample in the HR and HR + BD modes. The electrostatic field between the sample and the STEM detector collimates TEs toward the optical axis. We can detect signal electrons transmitted at large polar angles with respect to the optical axis.

On the other hand, the sample is placed in a strong magnetic field in both UHR and UHR + BD modes. The electrons have spiral trajectories because of the magnetic field and they can cross the optical axis plane several times before they reach the detector. Thus the angular distribution is not simply interpretable as in the case of the HR mode.

We focus on the capability of the STEM detector to collect signal electrons by its individual segments (BF, DF1, DF2, DF3, DF4 and HAADF) depending on their energy, initial polar  $\theta_0$  and azimuthal angles under which the electrons leave the plane of the sample. EOD [2] simulations of the UHR mode, see Fig. 1, allow us to map the initial polar angle to radius in the detection plane. This information is not directly accessible in the STEM measurement. The simulations in Fig. 1 do not include the influence of the sample material,  $\theta_0$  ranges from  $0^\circ$  to  $90^\circ$  with a constant step  $1^\circ$ . If we want to compare the simulated results with the experimental data, then it is desirable to model the energy and angular distribution of the outgoing electrons for a given material.

Carbon based film of 20 nm thickness was imaged by the STEM detector in the above mentioned four modes. The landing energy was always 4 keV. We used the stage bias -4 kV in the BD mode (the primary beam energy of 8 keV). We collected images using each of the six segments of the detector and measured the average brightness of a defined image area to determine the signal intensity.

Monte Carlo simulations of electron propagation through thin foils of graphite were performed in the program Geant4 [3]. The trajectories of the electrons in the magnetic and electrostatic fields below the foil were traced using the software package EOD.

The results of both simulations and experiments for the carbon based film are shown in Fig. 2. The outcome of the simulation and the experiment is affected by many factors to a different degree. A good comparison of the experiment and the simulation needs to consider e.g. the sample purity, the actual sample thickness, simulation models used, detection parameters for each detector segment, etc. Our simulated and experimental results are in good agreement for all four microscope modes.

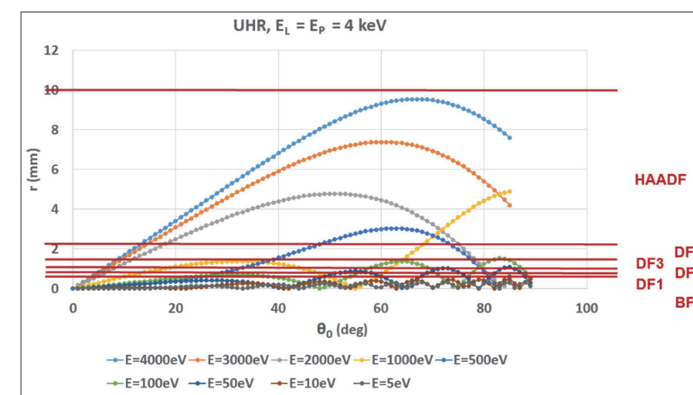


**Figure 1** EOD simulated radius  $r$  measured from the optical axis of the impact position of TE in the STEM detector plane as a function of the initial polar angle  $\theta_0$ , under which the TEs leave the sample; UHR mode, energy of TEs  $E_{TE} = 4000, 3000, 2000, 1000, 500, 100, 50, 10$  and  $5$  eV.

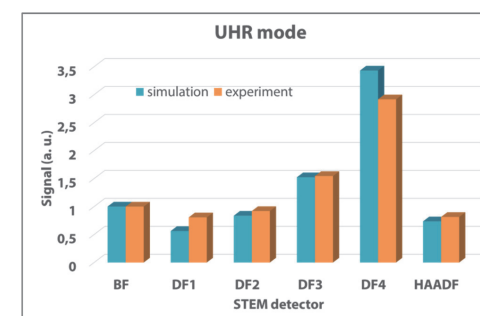


**Figure 2** Normalized signal from each segment; UHR mode.

### References:

- [1] Walker C.G.H., Konvalina I., Mika F., Frank L. and Müllerová I., Nucl. Instrum. Methods Phys. Res., Sect. B **415** (2018) 17-24.
- [2] Zlámál J. and Lencová B., Nucl. Instrum. Methods Phys. Res., Sect. A **645** (2011) 278-282.
- [3] Kief E. and Bosch E., J. Phys. D: Appl. Phys. **41** (2008) 215310.
- [4] The research is supported by the TA CR (TE01020118), MEYS CR (LO1212), its infrastructure by MEYS CR and EC (CZ.1.05/2.1.00/01.0017) and by CAS (RVO:68081731). The authors would like to thank Dr. M. Unčovský (FEI Czech Republic) for useful discussions.

## ULTRA-HIGH ENERGY RESOLUTION EELS

O.L. Krivanek<sup>1,2</sup>, A.L. Bleloch<sup>1</sup>, G. Corbin<sup>1</sup>, N. Dellby<sup>1</sup>, M.V. Hoffman<sup>1</sup>, and T.C. Lovejoy<sup>1</sup>

<sup>1</sup>Nion R&D, 11511 NE 118th St, Kirkland, WA 98034, USA

<sup>2</sup>Department of Physics, Arizona State University, Tempe, AZ 85287, USA

\*e-mail: krivanek@nion.com

EELS in the electron microscope has progressed greatly in recent years. The best energy resolution reached prior to 2013 was about 40 meV in a 30 msec exposure (full-width at half-maximum of the zero loss peak (FWHM of ZLP) at 200 kV) and the ZLP “tail” intensity was about 1/1000 of the ZLP maximum at an energy loss of 300 meV [1]. The introduction of the Nion ground-potential monochromator in 2013 improved the energy resolution to 16 meV in a 55 msec exposure (at 60 keV) [2], and allowed the exploration of vibrational (phonon) signals in the electron microscope to begin [3]. The introduction of the Nion EEL spectrometer in 2017 improved the resolution to 6 meV in a 100 msec exposure at 60 keV (Fig. 1), and reduced the ZLP tail to the 1/1000 level at 40 meV loss [4].

Our design has:

- Eliminated the deleterious effects of high tension (HT) instabilities, by putting the monochromator (MC) at ground potential, a design in which HT instabilities displace the ZLP incident on the energy-selecting slit, but do not change the energy selected by the slit.
- Eliminated the effects of instabilities in the prism current, by connecting the three MC prisms plus the spectrometer prism in series. The result is that instabilities in the prism current do not affect the position of the spectrum on the EELS camera.
- Improved the stability of the HT by sensing the beam intensity falling on each half of the MC’s energy-selecting slit, and using the difference signal for HT stabilization.
- Improved the stability of the EELS by a careful design of its multipoles, avoiding schemes that lead to substantial dipole-like instabilities that randomly displace the spectrum.
- Decreased the sensitivity of the system to stray magnetic fields, by putting quadruple mu-metal shielding around the monochromator and triple shielding around the EELS.
- Decreased the sensitivity to mechanical vibrations, by strengthening the EELS with robust anti-vibration bracing.

Another key ingredient is high-order aberration correction. As shown by Fig. 2, there are small crossovers containing images of the electron source in many planes in the microscope, including the MC slit, the sample, and the EELS. At each of these places, higher performance (better energy or spatial resolution) becomes possible by minimizing the size of the image. We minimize the size by performing 3<sup>rd</sup> order aberration correction in the monochromator, and correcting all aberration up to 5<sup>th</sup> order in the probe corrector and the spectrometer.

Examples of recent applications include momentum-resolved vibrational spectroscopy that provides similar information to neutron scattering and inelastic X-ray spectroscopy, but from much smaller volumes [5], measuring the temperature of small sample areas by energy gain/energy loss spectroscopy [6], and vibrational spectroscopy of water (Fig. 3) that also detected isotopic substitution [7]. These and other examples will be presented in the talk.

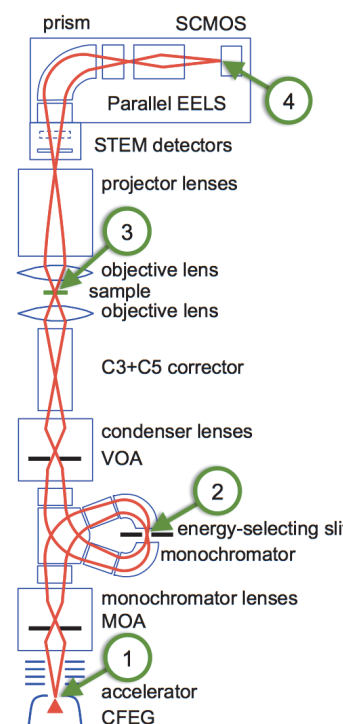


**Figure 2** Schematic diagram of the electron trajectories through the Nion Ultra-High Energy Resolution Monochromated EELS-STEM (U-HERMES). The most important beam crossovers containing an image of the electron source are:

- 1 = CFEG virtual crossover
- 2 = monochromator slit crossover
- 3 = sample-level crossover
- 4 = EEL spectrum crossover

References:

- [1] E Essers et al., *Ultramicroscopy* **110** (2010) 971–980.
- [2] OL Krivanek et al., *Microscopy* **62** (2013) 3–21.
- [3] OL Krivanek et al., *Nature* **514** (2014) 209–213.
- [4] <https://www.stem.lps.u-psud.fr/chromatem-delivers-site-sub-5-mev-30-kev>
- [5] FS Hage et al., *Science Advances* (2018) in print.
- [6] J-C Idrobo et al., *Phys. Rev. Lett.* **120** (2018) 095901.
- [7] JR Jokisaari et al., in preparation (2018).

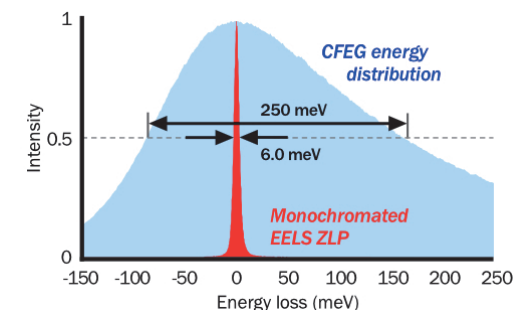


**Figure 1** Zero loss peak (ZLP) obtained at 60 keV primary energy with 100 ms acquisition time and  $\sim 11$  mrad half angle collection ( $\beta/2$ ) compared to unmonochromated CFEG energy distribution.

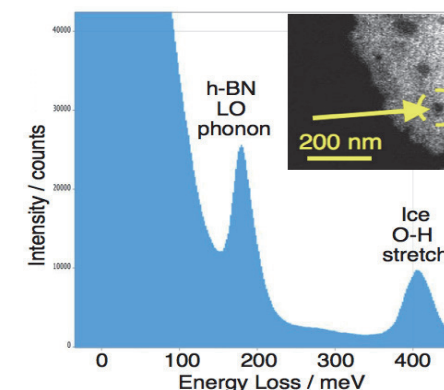


**Figure 3** Vibrational spectrum of ice adsorbed onto an h-BN flake. Insert shows the h-BN flake, coated with about 30 nm of ice, with a hole made by the beam (arrowed). The probed area is indicated by the dashed yellow circle.

## STABLE Ce<sup>4+</sup> CENTRES – A TOOL TO OPTIMIZE CATHODOLUMINESCENCE PERFORMANCE IN GARNET SCINTILLATORS

O. Lalinský<sup>1</sup>, P. Schauer<sup>1</sup>, M. Rathaiah<sup>2</sup>, M. Kučera<sup>2</sup>

<sup>1</sup>Institute of Scientific Instruments of the CAS, Královopolská 147, 612 64 Brno, Czech Republic

<sup>2</sup>Charles University, Faculty of Mathematics and Physics, 121 16 Prague, Czech Republic

\*e-mail: xodr@isibrno.cz

Garnet single crystals are widely used as scintillators in electron detectors. Cerium activated lutetium aluminum garnet Ce<sub>x</sub>:Lu<sub>3-x</sub>Al<sub>5</sub>O<sub>12</sub> (LuAG:Ce) is a promising example of such material for these applications. This is mainly due to its high light yield (LY) of 25 kph/MeV, short decay time of 60–80 ns, high atomic density (6.7 g/cm<sup>3</sup>), and high radiation stability with no hygroscopicity. The cathodoluminescence (CL) performance can be improved by Ga and Gd doping the garnet matrix. Proper admixture of these elements can increase the LY to 50–60 kph/MeV in addition to eliminating unwanted slower decay components. There was an idea that further decay acceleration can be achieved by doping the garnet with monovalent (Li<sup>+</sup>) or divalent ions (Mg<sup>2+</sup>, Ca<sup>2+</sup>). This should increase the valency of some Ce<sup>3+</sup> centres to Ce<sup>4+</sup> which should better compete with electron traps, and thus accelerate the decay. Our previous work proved the same decay trend [1], however, at a price of the LY. Such LY loss may induce the idea, if the stable Ce<sup>4+</sup> centres are really participating in Ce<sup>3+</sup> emission.

To verify this idea, Mg-rich LuAG:Ce,Mg and LuGAGG:Ce,Mg single crystalline films were prepared. They were grown by the liquid phase epitaxy from lead-free BaO-B<sub>2</sub>O<sub>3</sub>-BaF<sub>2</sub> flux on bulk single crystal LuAG substrates. As a result, thin films with thickness around 10 μm with different concentration of Mg were prepared. This preparation method was chosen because the LuAG:Ce single crystals usually contain various unwanted structural defects (mainly antisite defects). These defects can result in nonradiative recombination (losses of LY) and in delayed luminescence decay (afterglow). It was shown previously [2] that the concentration of these defects decreases with the decreasing temperature of the crystal growth. Therefore, single crystalline epitaxial films were preferred to the bulk ones because the growth temperature of the films is about a half (1000 °C) of the bulk ones (2000 °C). This ensured the structural defects elimination.

Cathodoluminescence (CL) was selected as an optimal tool for the luminescence study. E-beam ensures enough energy to excite over bandgap (contrary to photoluminescence) with sufficiently low penetration depth (contrary to radioluminescence) to prevent the substrate excitation. Moreover, CL is a native tool for the research of electron detectors. Specialized CL apparatus located at our institute was used for this purpose [3].

Absorption properties (Fig. 1), CL spectra (Fig. 2) and CL decays (Fig. 3) were studied at the presented specimens. The general trend of decreasing LY and accelerating decay to only units of ns was observed. The explanation of these trends follows: Without Mg-doping, the decay is relatively slow (50–80 ns decay time). Here, the CL is mainly caused by the radiative recombination on Ce<sup>3+</sup>, trap states or slow energy transfer from trap states to Ce<sup>3+</sup> (delayed recombination). Because Ce<sup>2+</sup> is an unstable configuration, firstly, the Ce<sup>3+</sup> has to capture the hole to form Ce<sup>4+</sup>. Secondly, the free electron is captured, so the radiative recombination, finally, can occur. Increasing concentration of Mg atoms induces more stable Ce<sup>4+</sup> centres that are immediately prepared to capture free electrons, thus Ce<sup>4+</sup> centres better protect electrons

to be captured by traps. This lowers the negative effect (delayed recombination, afterglow) of the traps. After all, hole is captured by Ce<sup>3+</sup> to form a stable Ce<sup>4+</sup> centre again. On the other side, the LY generally decreases (Fig. 2) with increasing Mg-content. This might be caused by an oxygen vacancy formation or O<sup>-</sup> centre stabilization which might cause nonradiative recombination centres. However, this is still contentious.

Nevertheless, it was shown that characteristic 5d-4f emission at Ce<sup>3+</sup> still occurs, even at high concentrations of Mg (> 7000 ppm). This is a very important result in comparison to optical absorption spectra because these Mg-rich films don't show any of the two characteristic absorption bands (Fig. 1) belonging to 4f-5d transfer at Ce<sup>3+</sup>, so all of the Ce<sup>3+</sup> centres are already converted into Ce<sup>4+</sup> ions. In addition to still visible Ce<sup>3+</sup> emission, this means, that Ce<sup>4+</sup> ions must play a significant role in Ce<sup>3+</sup> emission mechanism.

**Acknowledgements:** The research was supported by the Technology Agency of the Czech Republic (TE01020118), by Czech Science Foundation (projects GA16-05631S, GA16-15569S), by Ministry of Education, Youth and Sports of the Czech Republic (project LO1212) and by European Commission (project CZ.1.05/2.1.00/01.0017).

### References:

- [1] P. Schauer, O. Lalinsky, M. Kucera, Z. Lucenicova, and M. Hanus, Opt. Mater., 72 (2017), 359-366.
- [2] M. Nikl, E. Mihokova, J. Pejchal, A. Vedda, Y. Zorenko, and K. Nejezchleb, Phys. Status Solidi B 242 (2005) R119-R121.
- [3] J. Bok, P. Schauer, Rev. Sci. Instrum. 82 (2011) 113109.

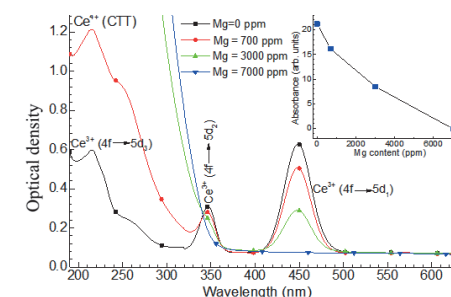


**Figure 1:** Optical density (sum of optical absorption + scattering + reflection) of LuGAGG:CeMg film with different Mg-content. Inset graph: Height of the Ce<sup>3+</sup> (4f → 5d)<sub>1</sub> absorbance peak at 450 nm as a function of Mg-content.

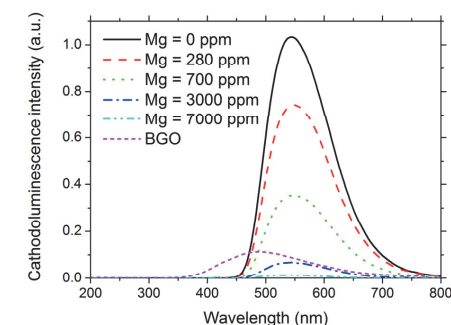


**Figure 2:** The cathodoluminescence emission spectra of LuGAGG:CeMg with different Mg-content. The spectra are compared with the one of the BGO bulk single crystal. Spectra were corrected for the apparatus transmissivity and detector spectral sensitivity.

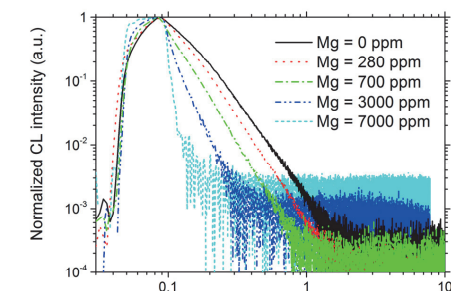


**Figure 3:** The cathodoluminescence (CL) decays of LuGAGG:CeMg with different Mg-content. The excitation pulse was 50 ns long.

## POSSIBILITIES OF A SECONDARY ELECTRONS BANDPASS FILTER FOR STANDARD SEM

F. Mika<sup>1</sup>, Z. Pokorná<sup>1</sup>, I. Konvalina<sup>1</sup> and A. Khurshed<sup>2</sup>

<sup>1</sup>Institute of Scientific Instruments of the CAS, Královopolská 147, Brno, Czech Republic

<sup>2</sup>Department of Electrical and Computer Engineering, National University of Singapore, 4 Engineering Drive 3, Singapore 117583

e-mail: fumici@isibrno.cz

Secondary electron filtering in Scanning Electron Microscope (SEM) has been in use for over a decade. This technique uncovers interesting contrasts in an otherwise ordinary SEM image which can possibly be used for dopant concentration mapping [1] or for discerning the slight molecular weight differences in apparently homogeneous organic materials [2]. Secondary electron filtering of semiconductor samples seems very promising as it may shed light on the mechanism of SEM image contrast between p-doped and n-doped semiconductors, possibly allowing to determine dopant concentration from SEM image alone.

The first experiments using secondary electron filtering were conducted using a through-the-lens detector (TLD) located inside the SEM column, which detects low-energy signal electrons re-entering the column through the narrow nozzle of the last lens. A set of biased electrodes (suction, push, mirror, and the sample itself) is used to draw the signal electrons back inside the column and then bend their paths toward the off-axis detector. This allows the respective voltage biases to be set in such a way that the resulting electrostatic field allows only specific energy and angle ranges to be detected.

TLD filtering can be employed in a standard commercial SEM and has been used e.g. by [3] and [4]. In our case, the Ultra-High Resolution SEM Magellan 400L from FEI was used to conduct our first proof-of-concept experiments (Figure 1). Electron optical calculations were made to determine the appropriate voltage biases of the TLD electrodes and the sample [5]. The sample was a custom-made silicon wafer with areas of differing, incremental dopant concentration.

For some specific uses we however find the TLD to be a rather crude tool as it doesn't allow setting the width of the bandpass filter with a very fine step. Especially for semiconductor applications the energy window has to be very narrow, set in steps of 0.1 eV instead of 1 eV as available with TLD. This is why we decided to incorporate a standalone analyzer into our UHR SEM instead and opted for an energy analyzer of the [6] design. The first experiment with this type of analyzer was made on the same doped structure as previously and Figure 2 shows the first preliminary results which maps the signal dependence on the detected energy of SE from heavily doped and substrate region of the semiconductor (N-type heavily doped patterns of the dopant concentration  $1 \times 10^{19} \text{ cm}^{-3}$ , made on an p-type Si substrate with dopant concentration  $1 \times 10^{15} \text{ cm}^{-3}$ ). The measured SE signal from n-type is higher than signal from p-type substrate for interval 0 – 1 eV. This experiment confirms that, the contrast strongly depends on energy of detected secondary electrons. For better understanding of this phenomenon further investigation with different dopant concentration and dopant types of semiconductor is needed.

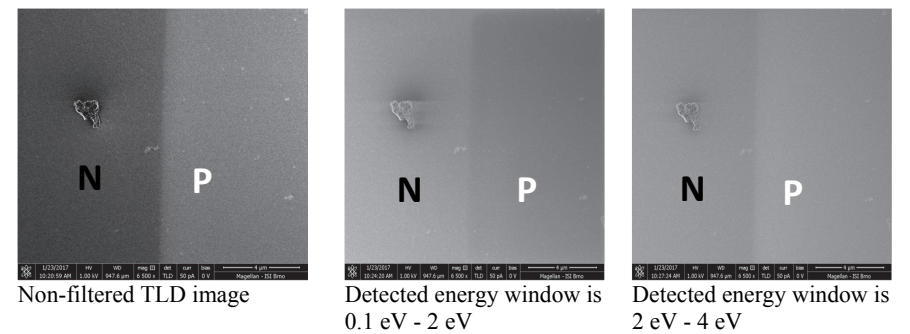


**Figure 1:** N-type doped patterns of the dopant concentration  $1 \times 10^{19} \text{ cm}^{-3}$ , made on an p-type Si substrate (dopant concentration  $1 \times 10^{15} \text{ cm}^{-3}$ )

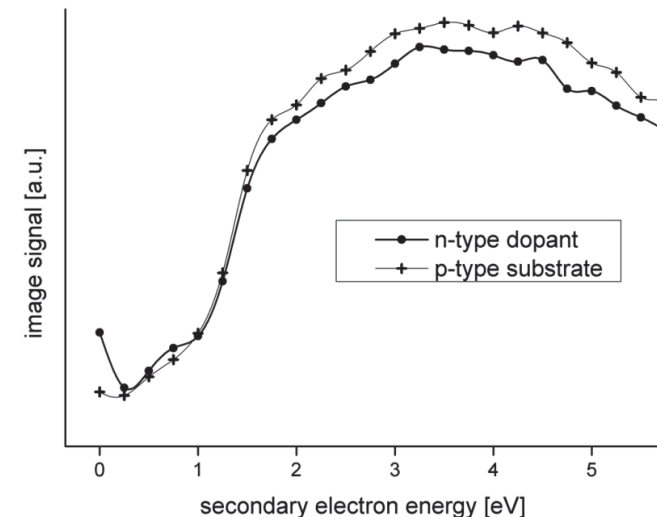


**Figure 2:** Secondary electron energy spectra from doped and substrate region of the sample imaged in Figure 1.

### References:

- [1] Kazemian, P., Mentink, S. A. M., Rodenburg, C., & Humphreys, C. J. (2007). Quantitative secondary electron energy filtering in a scanning electron microscope and its applications. *Ultramicroscopy*, 107(2-3), p. 140-150.
- [2] Masters, R. C., Pearson, A. J., Glen, T. S., Sasam, F. C., Li, L., Dapor, M., ... & Rodenburg, C. (2015). Sub-nanometre resolution imaging of polymer-fullerene photovoltaic blends using energy-filtered scanning electron microscopy. *Nature communications*, 6, p. 6928.

- [3] Dapor, M., Masters, R. C., Ross, I., Lidzey, D. G., Pearson, A., Abril, I., ... & Mika, F. (2018). Secondary electron spectra of semi-crystalline polymers—A novel polymer characterisation tool?. *Journal of Electron Spectroscopy and Related Phenomena*, 222, p. 95-105.
- [4] Mika F., Konvalina I., Kratky S. and Mullerova I., 15th International Seminar on Recent Trends in Charged Particle Optics and Surface Physics Instrumentation, Brno (2016), p. 36-37.
- [5] Konvalina I., Mika F., Kratky S. and Mullerova I. , 15th International Seminar on Recent Trends in Charged Particle Optics and Surface Physics Instrumentation, Brno (2016), p. 28-29.
- [6] Hoang, H. Q., and A. Khurshheed. *Journal of Vacuum Science & Technology B: Microelectronics and Nanometer Structures Processing, Measurement, and Phenomena* **27.6** (2009) p. 3226–3231.
- [7] The research was supported by Ministry of Education, Youth and Sports of the Czech Republic (project LO1212). The research infrastructure was funded by Ministry of Education, Youth and Sports of the Czech Republic and European Commission (project CZ.1.05/2.1.00/01.0017) and by The Czech Academy of Sciences (project RVO:68081731).

## ELECTRON OPTICS OF THE MULTI ELECTRON BEAM SOURCE (MBS) FOR AN MBSEM

A. Mohammadi-Gheidari<sup>1,2\*</sup>, X. Guo<sup>1</sup> and P. Kruit<sup>1</sup>

<sup>1</sup>Department of Imaging Physics, Delft University of Technology, Lorentzweg 1, 2628 CJ Delft, The Netherlands

<sup>2</sup>Advanced Technology group, Thermo-Fisher Scientific, Achtseweg Noord 5, 5651 GG Eindhoven, The Netherlands

\*e-mail: a.m.gheidari@tudelft.nl, Ali.Gheidari@fei.com

In electron optical systems used for imaging or patterning, a beam of electrons is focused onto a probe whose smallest obtainable size is a good indication of the best resolution of the system. More than 50 years of research and development have been devoted into improving the resolution of these systems; making the electron probe as small as possible. Present day instruments can easily provide sub nm probe size, but the probe current is only tens of Pico-Amps. Such a small probe current restricts the throughput of these instruments remarkably. Multi electron beam systems, in which not one but many electron beams are focused onto the sample simultaneously, can enhance the throughput to a great extent. A Multi Beam Scanning electron Microscope (MBSEM) based on the FEI Nova-Nano 200 SEM column was designed and built in our research group at Delft University of Technology. It delivers 196 focused beams onto a sample [1-3]. Figure 1 shows a schematic overview of the electron optical configuration of the MBSEM. One of the essential components of this instrument is the multi beam source unit (MBS) which replaces the standard single beam source unit of the Nova Nano SEM. In the MBS, the emission cone of a high brightness Schottky source is split into an array of focused beams by an aperture lens array (ALA). The MBS possesses unique electron optical properties: the zero-strength macro lens and field curvature compensating aperture lenses. The two macro electrodes (E-1 and E-2) in combination with the extractor electrode (Ext.) and the aperture plate create a so called “zero-strength lens (ZSL)” (Fig. 2a). The task of the ZSL is to create an electrostatic field on the aperture array which turns the apertures into single-electrode micro-lenses without causing a macro-lens effect between the electron source and ALA. Moreover, by careful manipulation of the shape of the field at the aperture plate, which is actually done by adjusting the voltages of the E-1 and E-2, it is possible to correct the field curvature, so the array of micro-beams focuses in a flat plane (Fig. 2b). The MBS with its, above mentioned, two unique electron optical properties was first introduced by Kruit et al [5] and a detailed aberration calculation was presented by Zhang et al [6]. Both Kruit and Zhang assumed that the “zero-strength” effect of the ZSL is guaranteed if the design is set such that the angular deflection at the plane of the aperture array is zero. However, in recent further theoretical investigations and simulations, it was found that this assumption is incorrect. The macro ZSL is not a “thin” but a “thick” lens; even if the angular deflection at the aperture array plane is zero, its axial spherical and chromatic aberrations aren't necessarily zero or even small. In fact, these aberration coefficients could be very large leading to an unacceptable astigmatism and extra contributions to the field curvature in the image plane of the array. Therefore, in the design of the zero strength lens, it is not the zero deflection at the aperture plane that should be respected but its axial spherical and chromatic aberration coefficients should be made as small as possible, close or even equal to zero! The

latter is possible because in the design of the MBS, there is no central aperture in the ALA plane: for the macro lens it can be considered a closed electrode. This leaves the possibility for a charge on the optical axis of the ZSL and according to the Scherzer theorem; it should then be possible to configure a lens with axial spherical and chromatic aberration coefficients equal to zero or even negative. A comprehensive and detailed analysis and design of the MBS will be presented.

### References:

- [1] A. Mohammadi-Gheidari, PhD Thesis, Delft University of Technology, Nov. 2013.
- [2] A. Mohammadi-Gheidari, C.W. Hagen and P. Kruit, JVST B 28(6) 2010.
- [3] A. Mohammadi-Gheidari and P. Kruit, NIMA 645 60-67, 2011.
- [4] B. Lencova and J. Zlamal, EOD (Electron Optical Design package), version 4.008.
- [5] P. Kruit et al, US 8 598 545 B2, Dec. 3, 2013.
- [6] Y. Zhang and P. Kruit, Physics Procedia 1 553, 2008.

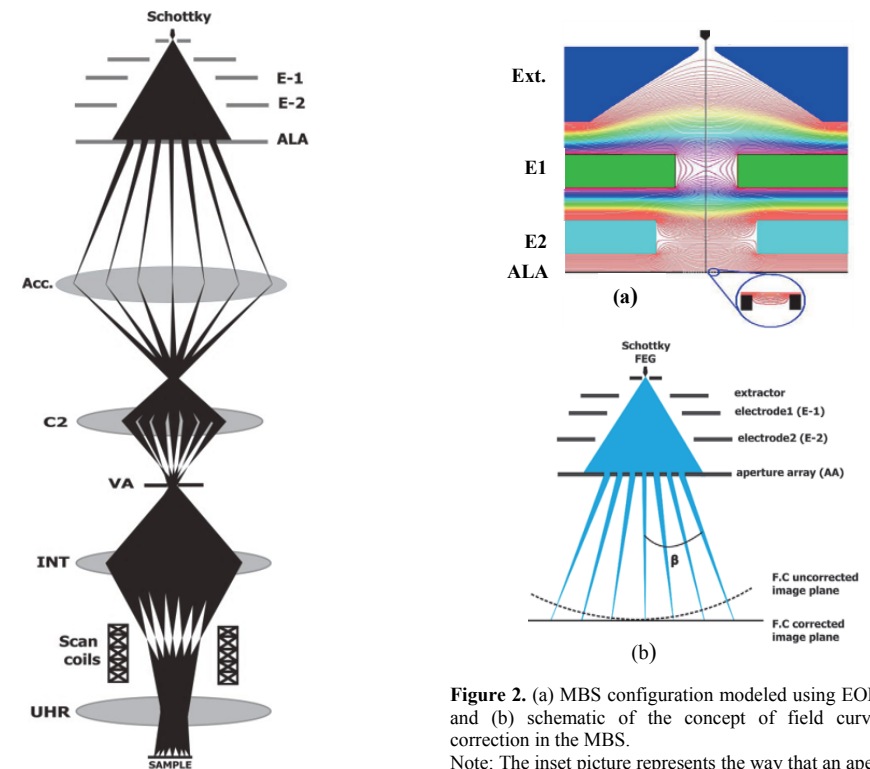


Figure 1. Schematic overview of the MBSEM electron optics column.

Figure 2. (a) MBS configuration modeled using EOD [4] and (b) schematic of the concept of field curvature correction in the MBS.

Note: The inset picture represents the way that an aperture lens effect is created.

## ANALYSIS OF LINEAR ION PAUL TRAPS USING 3-D FEM AND THE AZIMUTHAL MULTIPOLE FIELD EXPANSION

M. Oral<sup>1\*</sup>, O. Číp<sup>1</sup> and L. Slodička<sup>2</sup>

<sup>1</sup>Institute of Scientific Instruments of the CAS, v.v.i., Královopolská 147, 616 64 Brno, Czech Republic

<sup>2</sup>Department of Optics, Palacký University, 17. listopadu 12, 771 46 Olomouc, Czech Republic

\*e-mail: oral@isibrno.cz

Radiofrequency (RF) Paul traps are valuable in the design and in the operation of highly stable optical atomic clocks based on suitable trapped ions [1]. The traditional setup involves a single ion in an RF trap irradiated with a laser beam. The frequency of the laser light is then fine-tuned to match that of photons coming from an electronic transition in the atomic shell. The achievable frequency stability is about  $10^{-17}$  for laser-cooled ions. However, the stability can be further improved by using heavy atoms (such as Thorium) and the more stable frequencies of their nuclear transitions, and by setting up so-called Coulomb crystals, to improve the frequency measurement statistics by increasing the number of reference atoms [2]. These techniques and their combination could reach relative stabilities beyond  $10^{-20}$ .

Fig. 1 shows the trap operated at the Institute of Scientific Instruments (ISI). It was obtained through a cooperation with the Institute for Quantum Optics and Quantum Information of the Austrian Academy of Sciences. It is a linear quadrupole RF trap. The ion confinement around the z-axis is facilitated by an RF electric field generated by the quadrupole electrodes, the field contribution from the axial endcap electrodes then stabilizes the ions along the z-axis. The endcap electrodes have axial openings to allow a laser beam to pass through them.

We used Comsol Multiphysics to calculate the electric field in the trap shown in Fig. 1. The geometry has several symmetry and antisymmetry planes, which allows to reduce the whole simulated problem to 1/16 of the design by applying the Dirichlet and Neumann conditions on the appropriate boundaries (besides the Dirichlet conditions at the electrode surfaces). Furthermore, the field can be expressed as a superposition of two basis fields  $P_{+-}(x, y, z)$  and  $P_{++}(x, y, z)$  a computed for the following unit electrode potential assignments (Fig. 1b):  $P_{+-} : U_x = -U_y = 1V, U_c = 0$  and  $P_{++} : U_x = U_y = 1V, U_c = 1V$ . These functions are scaled to the actual electrode potentials, including the time-dependent part of the RF potentials. Fig. 2 shows the computed basis potential functions on the simulated section of the design.

During the experiment two circuit arrangements are used. In the first, non-symmetric RF wiring there is a DC voltage between one pair of quadrupole electrodes and the two endcap electrodes, in which the potential is expressed as  $-\frac{1}{2}U_{DC}(P_{++} + P_{+-}) + \frac{1}{2}U_{RF}(P_{++} - P_{+-}) \cos \omega_{RF}t$ . In the second, symmetric quadrupole wiring, the endcap electrodes are at a DC bias relative to a common ground, and each pair of the quadrupole electrodes is driven at a RF voltage in the counterphase relative to ground. This corresponds to  $U_{DC}(1 - P_{++}) + U_{RF}P_{+-} \cos \omega_{RF}t$ . The symmetric wiring, albeit electrically more complex, eliminates the RF micromotion on the z-axis, which is more suitable for the experiments.

A FEM simulation of the electric potential produces its values in a mesh of points scattered in the space. Then an accurate interpolation in the mesh is needed, especially in the region close

to the z-axis, where the ions are confined. The situation resembles that in charged particle optics, where accurate field evaluation is needed for reliable calculation of optical properties and real particle trajectories. A suitable representation of the electric potential in the vicinity of the z-axis is the sum of multipole components  $\Phi_m(r, z) = r^m \Re\{U_m(z, r^2)e^{im\phi}\}$ , where the two-dimensional functions  $\Phi_m(r, z)$  can further be expanded into power series expansions in the radial distance  $r$ . The whole field is then expressed in terms of axial multipole functions (depending on  $z$ ) and their derivatives [3]. The analytic model of the potential then can be fitted to the numerical FEM values to obtain the axial multipole functions [4]. The formula with the known analytic function than serves as the interpolation function.

In order to determine values of the axial multipole functions at certain z-coordinates by fitting, the FEM mesh points within a certain distance from the axis are arranged in a set of planes perpendicular to the z-axis. This way the axial multipole functions are determined as their values for a set of z-coordinates. To evaluate the values of the axial functions in an arbitrary z, the spline interpolation is used. For the fitting of the axial multipole functions we used a series expansion containing powers of the radial distance  $r$  up to 6. Within this approximation,  $P_{+-}$  consist only of the multipoles with  $m = 2$  and 6, and  $P_{++}$  only of those for  $m = 0$  and 4. An example of a fit is in Fig. 3.

The multipole series expansion serves as the starting point for semi-analytic computations of other important quantities of the trap in terms of the electrode voltages, the amplitude of the RF potential and its frequency: the secular potential (describing the time-averaged action of the confining field), eigenfrequencies of the secular ion motion, the conditions of confinement, the amplitude of the micromotion, stability and adiabaticity conditions, etc. [5]. That allows a straightforward determination of the optimum operating conditions of the trap for a given ion. We expect the multipole analysis will be advantageous in simulation of more complicated setups, involving, for example, the Coulomb crystals.

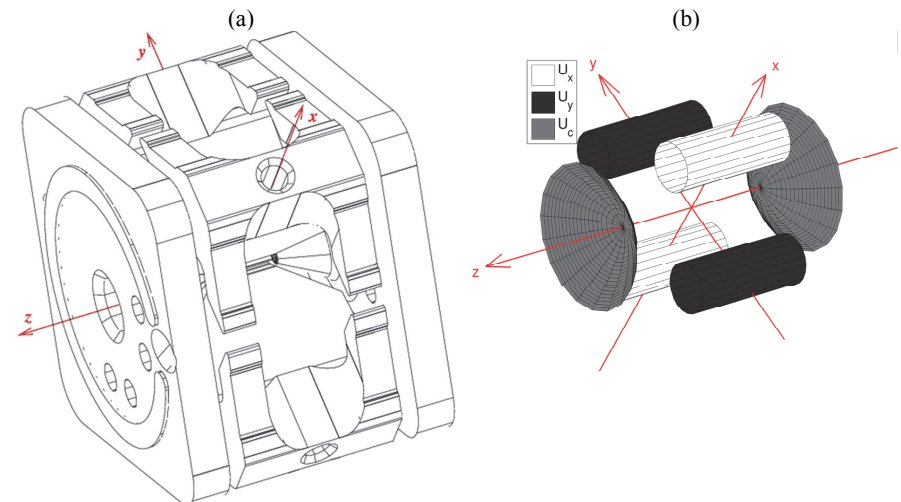


**Figure 1:** A drawing of the complete trap assembly (a), and the schematic drawing showing the quadrupole electrode pairs and the axial endcap electrodes (b).

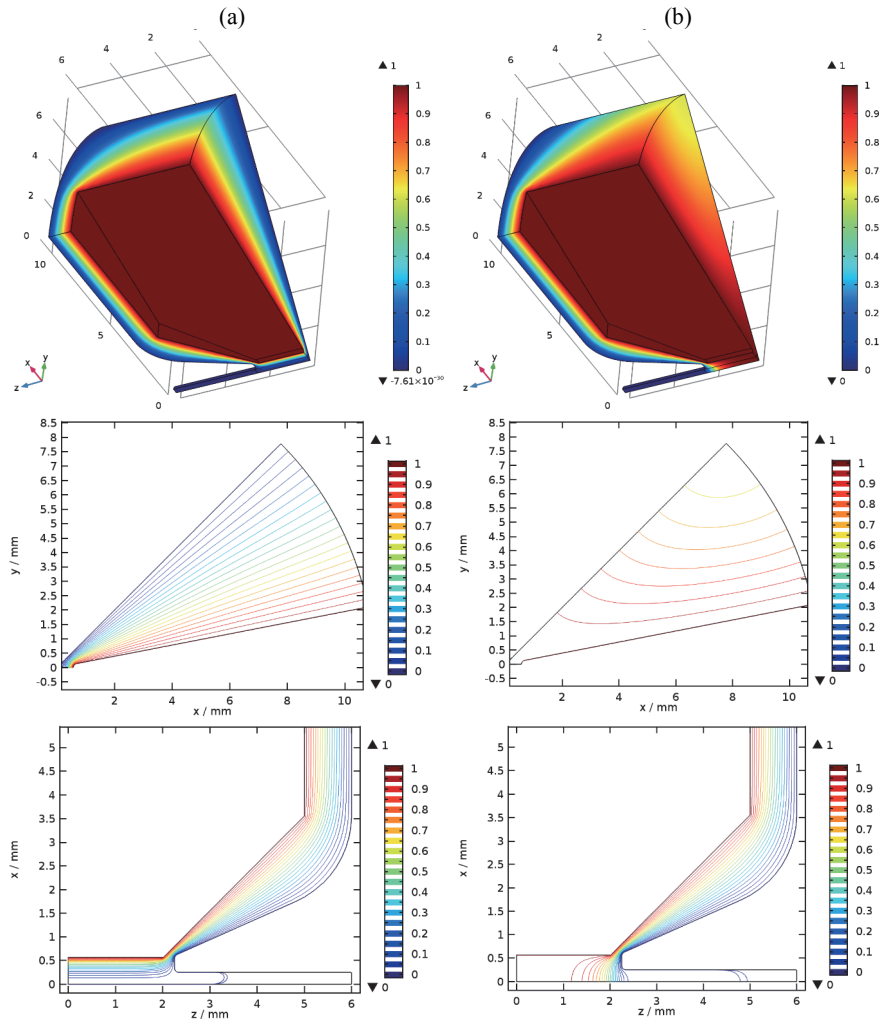


**Figure 2:** Computed basis potential distributions on the simulated 1/16 of the trap geometry, potential in the whole geometry can be obtained by mirroring the shown sections by the planes of symmetry or antisymmetry (planes  $x = \pm y, x = 0, y = 0, z = 0$ ). Column (a): basis function  $P_{\pm-}$ , column (b): basis function  $P_{++}$ . On the rows there is the potential on the surface of the simulated section, the equipotentials in the section  $z = 0$  and in the section  $y = 0$ , respectively.

For example, the first-order stiffness factors of the secular trapping force on the  $z$ -axis can be expressed for an ion with mass  $M$  and charge  $q$  in the corresponding directions as  $k_{x,y,z}(x) = q^2 U_{RF}^2 f_{x,y,z}(z) / 4M\omega^2 + qU_{DC} g_{x,y,z}(z)$ , where the functions  $f(z)$  and  $g(z)$  are expressed in terms of the multipole axial functions  $p_{m,n}$ . For the symmetric RF driving they are  $f_x = f_y = 2p_{2,0}^2, f_z = 0, g_x = g_y = p_{0,2}/4, g_z = -p_{0,2}/2$ . They are shown in Fig. 4. The requirement of

a positive stiffness factors then leads to conditions for a basic trap stability in terms of the ion parameters, the voltages  $U_{DC}$  and  $U_{RF}$ , and the RF frequency.

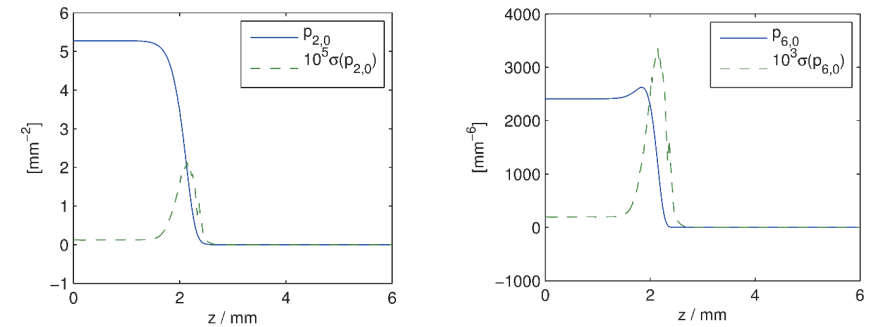


**Figure 3:** Axial functions for the basis potential function  $P_{+-}$ , with  $p_{2,0}$  being the quadrupole axial function and  $p_{6,0}$  the dodecapole function, the next non-zero multipole component for that basis function. The dashed curves are the standard deviations (note the scaling) and they demonstrate the high accuracy of the FEM calculation and the fit of the analytic model.

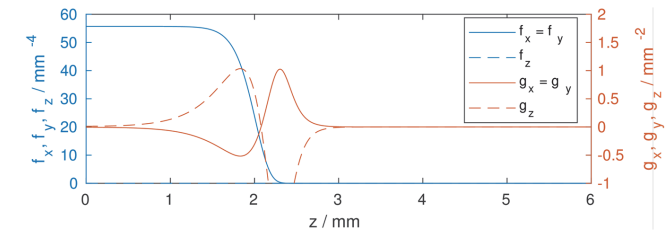


**Figure 4:** The functions appearing in the formulas of the secular stiffness factors for the case of the for the symmetrical RF quadrupole driving.

#### Acknowledgements:

We acknowledge the kind technological support from the group of Rainer Blatt including the contribution of Yves Colombe and Kirill Lakhmankiy to the construction of the employed linear Paul trap.

This work is supported by grant No. GB14-36681G of the Czech Science Foundation, and by the project EMPIR 17FUN07 CC4C of the European Association of National Metrology Institutes (EURAMET).

#### References:

- [1] A. D. Ludlow, M. M. Boyd, J. Ye, E. Peik, P. O. Schmidt, Rev. Mod. Phys. **87** (2015)
- [2] P. Obsil, L. Lachman, T. Pham, A. Lesundak, V. Hucl, M. Cizek, J. Hrabina, O. Cip, L. Slodicka and R. Filip, Phys. Rev. Let. (2018), accepted for publication
- [3] P. W. Hawkes, E. Kasper: Principles of Electron Optics, Vol. **1** (1994), Academic Press
- [4] M. Oral, B. Lencová, Nucl. Instr. Meth. A, Vol. **645**, (2011), p. 130-135
- [5] D. Gerlich, Inhomogeneous RF Fields: A Versatile Tool for the Study of Processes with Slow Ions, in C.-Y. Ng and M. Baer (ed.): Advances in Chemical Physics Series, Vol. **LXXXII** (1992), ISBN 0-471-53258-4

## OPTOFLUIDIC TECHNIQUES FOR DIRECTED EVOLUTION OF ENZYMES

Z. Pilát<sup>1\*</sup>, J. Ježek<sup>1</sup>, O. Samek<sup>1</sup>, P. Zemánek<sup>1</sup>, T. Buryška<sup>2</sup>, J. Damborský<sup>2</sup> and Z. Prokop<sup>2</sup>

<sup>1</sup>Institute of Scientific Instruments of the CAS, v.v.i., Czech Academy of Sciences, Kralovopolska 147, 612 64 Brno, Czech Republic

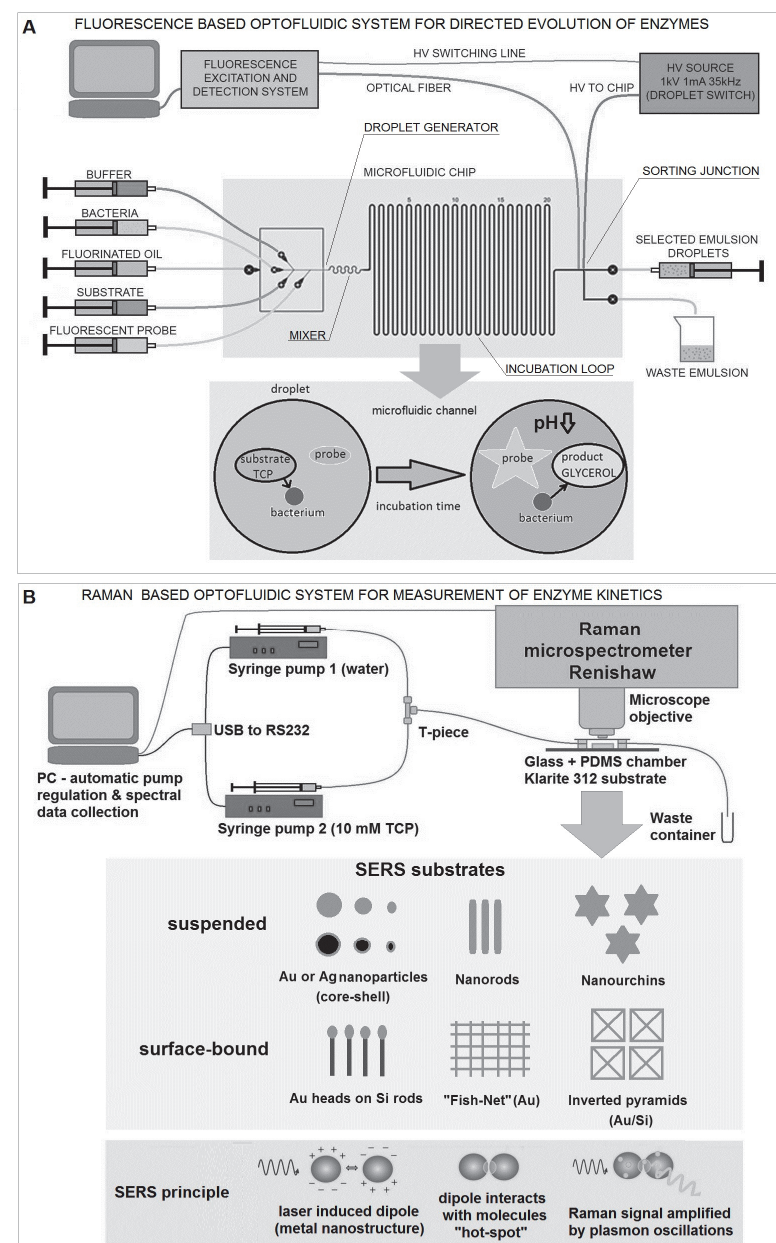
<sup>2</sup>Loschmidt Laboratories, Department of Experimental Biology & RECETOX, Faculty of Science, Masaryk University, Kamenice 5/A13, 625 00 Brno, Czech Republic

\*e-mail: pilat@isibrno.cz

Enzymes are highly versatile and ubiquitous biological catalysts. They can greatly accelerate large variety of reactions, while ensuring appropriate catalytic activity and high selectivity. These properties make enzymes attractive biocatalysts for a wide range of industrial and biomedical applications. Over the last two decades, directed evolution of enzymes has transformed the field of protein engineering.

We have devised microfluidic systems for directed evolution of haloalkane dehalogenases in emulsion droplets. In such a device, individual bacterial cells producing mutated variants of the same enzyme are encapsulated in microdroplets and supplied with a substrate. The conversion of a substrate by the enzyme produced by a single bacterium changes the pH in the droplet which is signaled by pH dependent fluorescence probe, see Figure 1A. The droplets with the highest enzymatic activity can be separated directly on the chip in a sorting junction by dielectrophoresis and the resultant cell lineage can be used for enzyme production or for further rounds of directed evolution. The developed platform is applicable for screening of large libraries in directed evolution experiments requiring mutagenesis at multiple sites of a protein structure.

In a system for evaluation of the enzyme kinetics of the dehalogenase reactions, we use Raman microspectroscopy and surface enhanced Raman spectroscopy (SERS) in microfluidic systems for detection of the reaction substrate and metabolites, see Figure 1B. The apparatus used for sequential dilution of glycerol and haloalkane TCP (1,2,3-trichloropropane) consisted of two microfluidic piston pumps with manual and computer controlled regime (via USB to RS232 converter and LabView GUI). In the calibration experiments, the syringes were filled with glycerol or TCP solutions or water respectively and the ratio of the pumping speeds was used to dilute the solutions in a stepwise manner. The resultant solution was pumped into a chamber with SERS substrate, or into a square glass capillary and measured by Raman spectroscopy. We were able to measure glycerol and TCP concentrations at millimolar concentrations. We used PCA (principal component analysis) for evaluation of the Raman spectra. We aim to use the calibrated apparatus to gauge the rate of catalysis for individual dehalogenase enzymes and enzyme mixtures in various reaction conditions. This is useful for mapping the optimal reaction conditions.



## REAL TIME OBSERVATION OF STRAIN IN THE SEM SAMPLE

J. Piňos, L. Frank

Institute of Scientific Instruments of the CAS, v. v. i., Královopolská 147, 612 64, Brno, Česká republika  
e-mail: pinos@isibrno.cz

The SEM with various detector arrangements and analytical attachments represents an irreplaceable tool in material research. One of the techniques available in most contemporary microscopes is the scanning low energy electron microscopy (SLEEM) with biased specimen [1], marketed as the beam deceleration mode, gentle beam and others. The SLEEM allows controlling the information depth of the backscatter electron (BSE) imaging within a wide range by altering the landing energy of electrons.

The BSE micrographs show, among others, crystallographic contrast distinguishing grains in polycrystals. On non-deformed (relaxed) samples we get the image signal homogeneous within a grain while with heavily deformed metal samples gradual signal variations appear even inside grains [2,3] – see Fig. 1.

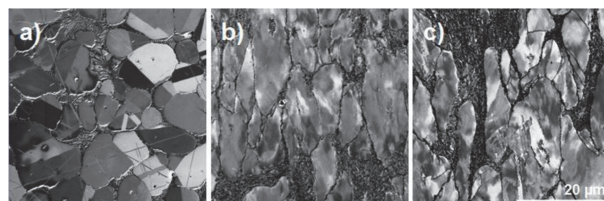


Fig. 1: Tixofomed X210Cr12 steel shown in BSE micrographs at 500 eV in the SLEEM mode: non-deformed sample (a), deformed and air cooled (b), and deformed and quenched (c) (reproduced from [3]).

Micrographs in Fig. 1 were taken at unloaded samples after their processing. Clearly visible effects of deformation raise a question about possible correlation of appearance of the SLEEM micrographs and the instant distribution of the material strain, i.e. about possibility of observing the sample deformation in real time including possible quantification.

In order to perform pilot experiments of this kind we have adapted the miniaturized tensile tester DEBEN Microtest for operation in the SLEEM mode with biased sample. The tester offers various load capacity adjustable by interchangeable gearboxes and load cells; our version has the load capacity of 300 N and travel of 10 mm in length. Original metallic clamps have been replaced with insulating ones that would enable to bias the sample in the kV range. The clamps (see Fig. 2) were fabricated from polyetheretherketone (PEEK), acceptable as regards both electrical and mechanical parameters.

With the given load capacity of the tensile tester and necessity to secure a sufficiently large planar equipotential surface of the sample, we were restricted to testing thin foils with cross-section in low units of  $\text{mm}^2$ . For the load capacity of 300 N and the cross-section of  $1 \text{ mm}^2$ , we get maximum stress of 300 MPa, which is sufficient for deformation of pure metals up to destruction of the foil.

Material of choice was copper and samples were made as 10 mm wide strips of a 0.35 mm thick foil, perforated with a 2 mm hole in the center. Sample was ground and polished upon

standard metallographic recipes. Deformation was localized around the hole, which facilitated preliminary adjustment of the field of view.

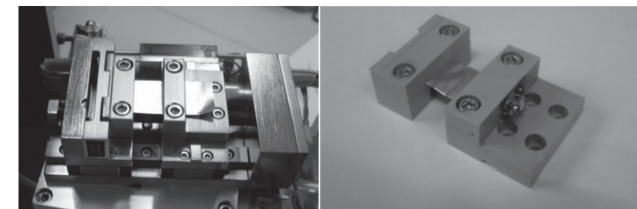


Fig. 2: The tensile tester with original clamps (left), insulating clamps made from the PEEK (right).

Experiments were conducted in the TESCAN Vega SEM equipped with a conventional thermo-emission gun, side mounted Everhart-Thornley detector (ETD) and a scintillator based BSE detector coaxially placed below the objective pole-piece. In the SLEEM mode the above-sample electric field prevents secondary electrons (SE) from impinging the ETD detector so image series in SE and BSE signals had to be collected in separate cycles, i.e. with different fields of view.

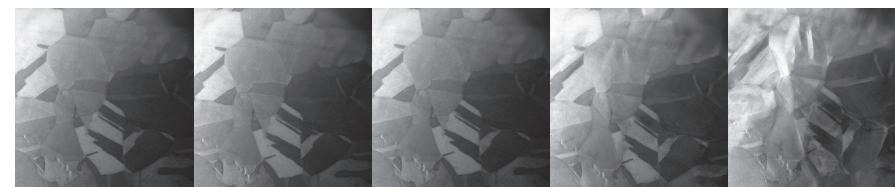


Fig. 3: Series of the BSE micrographs with loads of 0, 30, 70, 110, and 150 N.

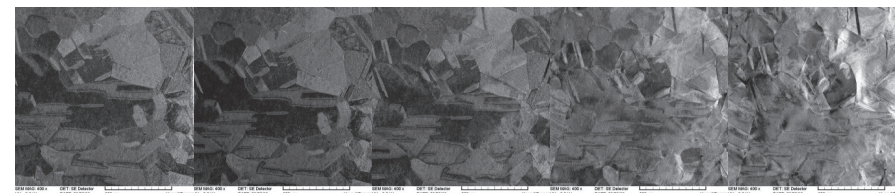


Fig. 4: Series of the SE micrographs with loads of 0, 65, 130, 195, and 260 N.

Both series in Figs. 3 and 4 reveal effects of deformation: at low loads the elastic deformation is only slightly apparent while when plastic deformation commences, homogeneous brightness of grains converts into a mixture of shades and the SE images reveal generation of changes in surface topography.

Study is still in progress with future concentration on quantification of the deformation and correlation with the structure appearance. Next experimental phase is planned in a device enabling the BSE and SE images to be recorded within a single deformation cycle.

[1] I. Müllerová, L. Frank, *Advances in Imaging and Electron Physics* **128** (2003) 309-443.

[2] Š. Mikmeková et al., *Key Engineering Materials* **465** (2011) 338-341.

[3] Š. Mikmeková et al., *Applied Surface Science* **275** (2013) 403-408.

## THERMAL DESORPTION SPECTROSCOPY IN PROTOTYPE FURNACE FOR CHEMICAL VAPOR DEPOSITION

L. Průcha<sup>1\*</sup>, B. Daniel<sup>1</sup>, J. Piňos<sup>1</sup>, E. Mikmeková<sup>1</sup>

<sup>1</sup>Institute of Scientific Instruments of the Czech Academy of Sciences, v.v.i., Královopolská 147, 612 64 Brno, Czech Republic

\*email: prucha@isibrno.cz

Cleaning of the sample surfaces is crucial for scanning electron microscopy [1], especially for low energy electron microscopy or for the deposition of thin layers, such as graphene [2], where surface has to be well prepared. In the best case, every unwanted particle should be cleaned from the sample surface for best low energy electron microscopy observation or thin film deposition. Unfortunately, the standard cleaning procedures can leave residues on the sample surface [3]. This work is focused on thermal desorption spectroscopy (TDS). TDS is a method of observing desorbed molecules from a sample surface during the increase of temperature of the sample. The aim of this study was to determine optimum conditions: temperature and time, to achieve clean surfaces in the shortest time.

Our prototype furnace combines the possibility of doing thermal desorption spectroscopy, chemical vapor deposition and also annealing of the samples with a high temperature (up to 1100°C) in ambient atmosphere or in a vacuum. The system is able to reach a pressure of  $10^{-4}$  Pa within minutes and a pressure of  $10^{-5}$  Pa within hours. There are two gauges connected to the system to control the pressure change during the experiment, adjusted for more different gasses. The low pressure in the furnace is crucial for the thermal desorption spectroscopy and the CVD of graphene. The increase of temperature and the time for annealing can be programmed through the digital panel on the furnace, which makes the whole experiment much easier to handle and makes it possible to adjust the parameters during the experiment.

This work is focused on the thermal desorption of selected gasses (mainly hydrocarbons –  $C_xH_x$ ) from the silicon surface, which was cleaned before the TDS measurement by the standard procedure. In our case, the standard cleaning procedure of silicon wafers consisted of ultrasound cleaning in acetone ( $CH_3-CO-CH_3$ ), ethanol ( $CH_3-CH_2-OH$ ) and deionized water ( $H_2O$ ). We have cleaned the samples separately with selected solution to get different spectra for each measurement. To obtain a better overview we have measured the spectra also for the samples cleaned with all three solutions and for different annealing temperatures (100°C, 200°C and 300°C). The resulting spectra clearly showed desorption of different gasses for each of the cleaning procedure. The strongest signal came from the mass (m/e) 18, which is the water molecule. Mass numbers 28, 29 and 43 are hydrocarbons mainly originated from acetone and ethanol, and 17 is molecule OH, which is a fragment of ethanol.

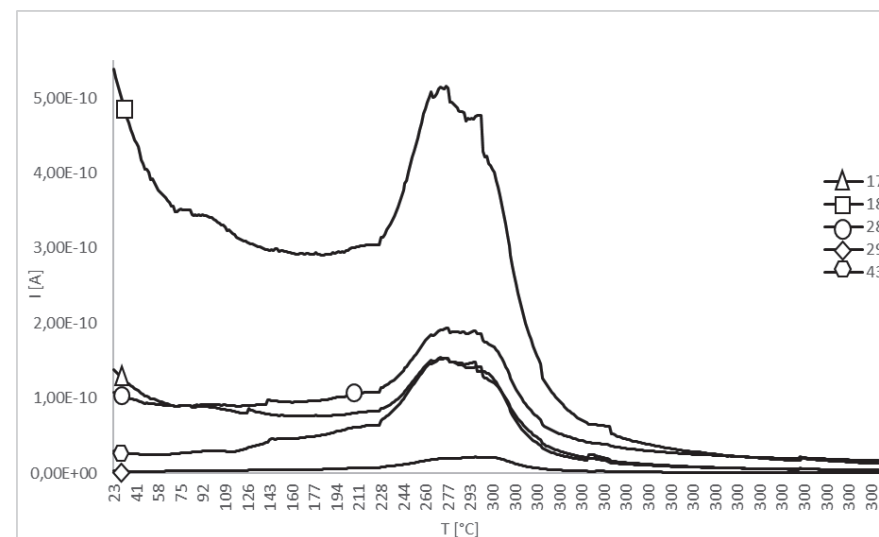


**Figure 1** The TDS spectrum for mass numbers (m/e) 17, 18, 28, 29 and 43. The current represents the concentration of the given molecules.

The results showed that the annealing of a silicon sample with temperatures of 100°C and 200°C is not efficient, since the signal of selected desorbed gasses is still dominant after hitting the maximal temperature. However, the temperature growth to 300°C shows the desorption spectrum peak placed at 277°C (Figure 1). After reaching this temperature the signal from the spectrum decreased even though the temperature still increased to 300°C. This indicates, that this temperature is high enough to dissociate the bonds of molecules attached to the surface and the sample surface is free of the residues originated from the cleaning procedure.

This work clearly shows the possibilities of our prototype furnace for annealing and the TDS analyses. The results correspond with expected outcome, since the spectrum shows dissolved molecules originated from acetone, ethanol and distilled water.

### References:

- [1] Reimer, L., *Scanning Electron Microscopy, Physics of Image Formation and Microanalysis*, ISBN 3-540-63976-4 2<sup>nd</sup> edition, Springer-Verlag Berlin Heidelberg 1998.
- [2] Li, X., et. al, *Large-Area Synthesis of High-Quality and Uniform Graphene Films on Copper Foils*, *Science* **324** (2009), 1312-1314.
- [3] Reinhardt, L., Kern, W. *Handbook of Silicon Wafer Cleaning Technology*, ISBN 978-0-8155-1554-8 2<sup>nd</sup> edition, Elsevier 2008.

The research is supported by the TA CR (TE01020118), MEYS CR (LO1212), its infrastructure by MEYS CR and EC (CZ.1.05/2.1.00/01.0017) and by CAS (RVO:68081731).

## DEVELOPMENT OF A COMPACT MASS SPECTROMETER FOR SPACE APPLICATIONS

R. Pureti\*, H. Q. Hoang, and T. Wirtz

Advanced Instrumentation for Ion Nano-Analytics (AINA), MRT Department, Luxembourg Institute of Science and Technology, 41 rue de Brill, L-4422 Belvaux Luxembourg

\*e-mail: rathaiah.pureti@list.lu

In-situ compositional analysis of the surface and the atmosphere of a planetary object is vital to understand the formation and evolution of solar systems, to find the evidence of the past or present life on Mars and other planets, to investigate the origin of life on Earth, and to evaluate the commercial and economic viability of the planetary materials. Recently, there has been an enormous interest in in-situ resource utilization (ISRU) of the lunar surface materials especially in terms of their commercial aspects [1]. The in-situ utilization of lunar materials allows us to explore the Moon further, to create and start scientific/economic operations from the lunar surface, and to export the lunar resources to the Earth [2]. As the assessment of the surface and atmospheric composition is critical for all these technological and economic feasibility studies, having a high sensitivity and larger mass range coverage mass spectrometer could be a suitable analytical instrument to characterize/map the lunar resources by rover/orbiter missions.

In the last 7 decades, many space missions utilized mass spectrometers for chemical composition and isotopic ratio analyses [3]. Amongst them, the magnetic sector based mass spectrometers either provide high performance but complex ion optical systems with a serial mass spectral acquisition or low performance but simple ion optical systems (based on Mattauch-Herzog configuration) with a multi-collector acquisition system. Recently, Luxembourg Institute of Science and Technology (LIST) has developed a high performance compact magnetic sector mass spectrometer (with dimensions of  $\sim 72 \times 27 \times 17 \text{ cm}^3$  and a weight of  $\sim 50 \text{ kg}$ ) for hydrology applications, which is capable of acquiring the wide range mass spectra simultaneously with high mass resolution. Its design is based upon a double focusing magnetic sector configuration, which consists of an electrostatic sector, a magnetic shunt, and a permanent magnet. This instrument is flexible for a wide range of applications, including the chemical composition identification and isotopic ratio measurement. As such, a detailed study has been performed to investigate potential space applications for the mass spectrometer, and to define the requirements and specifications that need to be adopted to the mass spectrometer to make it space deployable instrument.

As an outcome of the study, a lunar rover mission is chosen as a notional target mission for LIST's mass spectrometer to investigate the surface and subsurface chemical and isotopic compositions to evaluate the lunar ISRU. As such, based on the available data on lunar surface materials from previous lunar missions (Apollo [4], Chandrayan-1 [5], and LCROSS [6]) and on the mass spectrometers that contributed in various space missions, we have defined the physical and performance specifications for LIST's mass spectrometer according to the requirements of a lunar ISRU mission (Table 1). Accordingly, the mass spectrometer is designed to meet the requirements and specifications by scaling down its dimensions to fit into a volume of  $30 \times 15 \times 15 \text{ cm}^3$  and its weight to be less than 5 kg, with a mass range ( $m_{\text{max}}/m_{\text{min}}$ ) of about 35.

A schematic overview of our development is shown in Figure 1, in which the ion trajectories of 9 masses (from 2 to 70 amu) generated inside a dedicated electron impact ion source are traced through the ion source column, the electrostatic sector, the magnetic sector to its focal plane detector. The simulation was performed with SIMION simulation package [7].

Table 1: The physical performance and technical specifications of a mass spectrometer to be used for Lunar ISRU mission.

Physical specifications	Performance specifications	Technical specifications
Mass: < 5 kg Volume: $30 \times 15 \times 15 \text{ cm}^3$	Mass range: 2-70 amu Mass resolution: 2000 Sensitivity: $1\text{E-3}$ to $2\text{E-2}$ cts/mol/ $\text{cm}^3$ Dynamic range: $1\text{E+6}$ to $1\text{E+9}$	Operation temperature range: 243-313 K

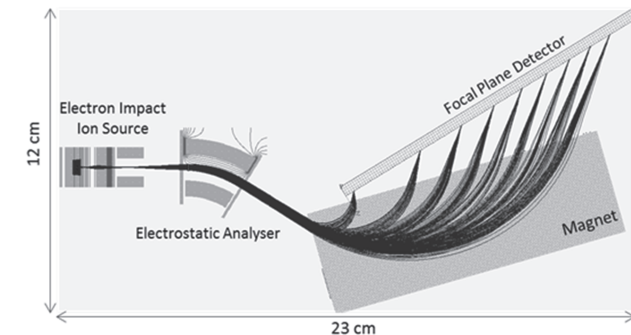


Figure 1. Schematic of the magnetic-sector mass spectrometer.

## References

- [1] I. A. Crawford, "Lunar Resources: A Review", *arXiv:1410.6865v1*, 2014.
- [2] G. B. Sanders and W. E. Larson, "Progress Made in Lunar In-Situ Resource Utilization Under NASA's Exploration Technology and Development Program", 2012.
- [3] J.H. Hoffman *et al.*, "Space applications of mass spectrometry. chapter 31", in *Applied Mass Spectroscopy Handbook*, John Wiley and Sons, 2010.
- [4] J. Fegley and T. D. Swindle, "Lunar volatiles: Implications for lunar resource utilization", in *Resources of Near-Earth Space*, University of Arizona Press, 1993, pp. 367-426.
- [5] R. Sridharan *et al.*, "'Direct' evidence for water (H<sub>2</sub>O) in the sunlit lunar ambience from CHACE on MIP of Chandrayaan I", *Planetary and Space Science*, vol. 58, p. 947-950, 2010.
- [6] A. Colaprete *et al.*, "Detection of Water in the LCROSS Ejecta Plume", *Science*, vol. 330, no. 6003, pp. 463-468, 2010.
- [7] SIMION ® 8.1, Scientific Instrument Services, Inc., 1027 Old York Road, Ringoes, NJ 08551-1054, USA., Available: <http://www.simion.com.>, 2018.

## ELECTRON OPTICAL PROPERTIES OF A NEW LOW-ENERGY SCANNING ELECTRON MICROSCOPE WITH A BEAM SEPARATOR

T. Radlicka<sup>1\*</sup>, V. Kolařík<sup>2</sup>, M. Oral<sup>1</sup>

<sup>1</sup>Institute of Scientific Instruments of the CAS, v.v.i., Královopolská 147, 616 64 Brno, Czech Republic

<sup>2</sup>Delong Instruments a.s., Palackého třída 3019/153b, 612 00 Brno, Czech Republic

\*e-mail: radlicka@isibrno.cz

### Introduction

The low energy scanning electron microscope (SEM) which is currently at the Institute of Scientific Instruments, suffers from low resolution and suboptimal detection systems. In the cathode lens regime, signal electrons are accelerated by the electric field between the sample and the objective lens, getting collimated. Those with low emission angles get through the bore in the BSE detector into the objective lens and cannot be detected by the available detectors now [1]. The information about the sample provided by these electrons is lost, which limits our microscopy methods.

These two limitations are to be overcome with a new low-energy SEM, which was developed at Delong Instruments. It consists of a field emission gun with the energy width of 0.8 eV, a magnetic condenser lens, and an electrostatic triode objective lens. The acceleration voltage is 5 kV. The sample stage can be biased at up to -5 kV to provide low landing energy without strong decrease of the resolution – the effect of the cathode lens [2]. A beam separator is placed in front of the deflection system for the detection of the signal electrons that get to the column. In a combination with standard detectors and cathode lens, it allows detecting all kinds of signal electrons.

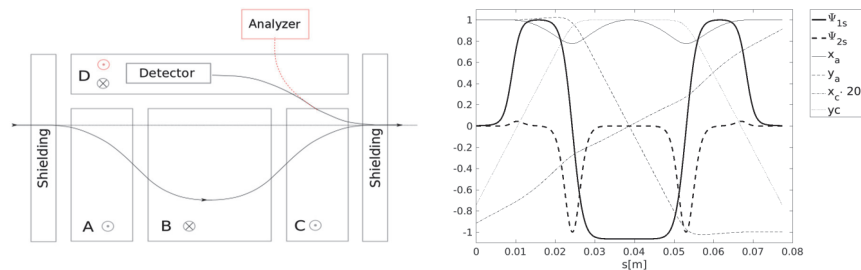


**Figure 1** Schematic drawing of the beam separator and the first-order properties of the separator computed for the 2D field (dependency of the field on the  $x$  coordinate is neglected)

### Beam separator

The separator was designed to be simple, yet effective, and compact in size. The requirements for the system resolution were not as critical as in the case of high-resolution microscopes. The system has only the first order correction, the second order aberrations are currently uncorrected. The separator shown in Fig. 1, consists of four magnetic prisms of rectangular shape. The prisms A, B, and C influence the primary beam. The outer ones have the same length  $L = 12$  mm, and the middle one has the length  $2L$ . The last prism is placed next to those three ones. The dipole field of the prism A deflects the beam from the axis, the prism B

has the opposite excitation and it bends the axial trajectory back to the axis. The prism C with the same excitation as the prism A deflects the axial trajectory such that it is again on the optical axis behind the separator. The signal electrons coming from the sample are deflected by the prism C in the opposite direction than the primary beam. Then they enter the prism D and they are collected on the detector or they are directed to the energy and angular analyzer, depending on the field orientation.

The presented system has the midsection symmetry [3], the dipole field has a focusing effect only in the  $x$ -direction but the quadrupole field influences the trajectories in both  $x$  and  $y$  components. The strength of the quadrupole field is given by the angle at which the axial particle enters the fringing field region between the prisms A, B and C. If the derivative of the magnetic field with respect to the  $x$  coordinate can be neglected, the focal length of the quadrupoles is given by the curvature  $\Gamma$  of the axial ray in the prisms and their length:

$$\frac{1}{f_x} = -\frac{1}{f_y} = \frac{2\Gamma^2 L}{\sqrt{1 - \Gamma^2 L^2}}.$$

The quadrupoles defocus in the  $x$ -direction and focus in the  $y$ -direction. The focal length has such a value that the quadrupole compensates the focusing effect of the prism. The ray  $x_a$  entering the separator with zero slope is locally symmetrical with respect to the plane of the local antisymmetry of the dipole field, and the ray  $x_c$  crossing the axis in the center of the separator is antisymmetric with respect to the symmetry plane of the dipole field. That eliminates dispersion. The separator acts as a drift region with the length  $2L/\sqrt{1 - \Gamma^2 L^2}$ .

The stigmaticity of the system can be simply fulfilled when the ray entering with the zero slope with respect to the separator is focused to the center of the separator (the system behaves as a lens doublet in the  $y$ -direction). Then the focal lens of the quadrupoles equals  $f_x = -f_y = L\varphi$ , where  $\varphi = \text{asin } \Gamma L$  is the central angle of the circular trajectory in the prisms. The situation is shown in the Fig. 1. The system with a parallel beam in front of the separator is stigmatic with equal absolute values of magnification in  $x$  and  $y$ -directions.

### Resolution of the system

The electron optical properties of the system were simulated using a general 3D calculation of the field in combination with the differential algebraic method [4], which is more general than the simplified basic description of the separator operation. We identified two main effects of the separator influencing the resolution of the whole system. The first one is given by the effect of the small size of the separator which makes the derivative of the magnetic field with respect to the  $x$  coordinate relatively large in magnitude, which then alters the focal lens of the quadrupole field components. The trajectory  $x_a$  has not a symmetry which would result in zero dispersion of the system. The second influence is due to the uncorrected second-order aberration, mainly the axial coma and the three-fold astigmatism. These effects decrease the resolution by a factor of about 2.

### References:

- [1] I. Mullerova, L. Frank, Adv Imaging Electron Phys. 128 (2003), p. 309-443.
- [2] T. Radlicka, Microscopy and Microanalysis **21**(S4), (2015) p. 212-217
- [3] H. Rose, Geometrical Charged-Particle Optics, Springer-Verlag (2009)
- [4] T. Radlicka, Adv. Imaging. Elect. Ph. **151** (2008), p. 241 – 362
- [5] The research was supported by VASE GRANTY, MEYS CR (LO1212), its infrastructure by MEYS CR and EC (CZ.1.05/2.1.00/01.0017) and by ASCR (RVO: 68081731).

## CREATION OF ELECTRON VORTEX BEAMS USING THE HOLOGRAPHIC RECONSTRUCTION METHOD IN A SCANNING ELECTRON MICROSCOPE

T. Řiháček<sup>1\*</sup>, M. Horák<sup>2</sup>, T. Schachinger<sup>3,4</sup>, M. Matějka<sup>1</sup>, F. Mika<sup>1</sup> and I. Müllerová<sup>1</sup>

<sup>1</sup>Institute of Scientific Instruments of the CAS, Královopolská 147, 612 64, Brno, Czech Republic

<sup>2</sup>Central European Institute of Technology, Brno University of Technology, Purkyňova 123, 612 00, Brno, Czech Republic

<sup>3</sup>Institute of Solid State Physics, TU Wien, Wiedner Hauptstraße 8-10, 1040, Wien, Austria

<sup>4</sup>University Service Centre for Transmission Electron Microscopy, TU Wien, Wiedner Hauptstraße 8-10, 1040, Wien, Austria

\*e-mail: rihacek@isibrno.cz

Electron vortex beams (EVB) were theoretically predicted in 2007 [1] and first experimentally created in 2010 [2,3]. Although they attracted attention of many researchers, their investigation takes place almost solely in connection with transmission electron microscopes (TEM). On the other hand, although scanning electron microscopes (SEM) may provide some advantages for EVB applications, only little attention has been dedicated to them. Therefore, the aim of this work is to create electron vortices in SEM at energies of several keV.

The first reproducible technique of EVB creation was a holographic reconstruction (HR) using an amplitude diffraction mask [3], which is relatively simple and straightforward. Moreover, HR produces a vortex beam of high purity of modes, which is very useful for SEM, where the spot shape detection is nontrivial. However, it also suffers from a few drawbacks. These are namely the requirement of a highly coherent primary beam, and a large current loss (about 95%) due to the absorption in the mask and the distribution of the current into multiple spots. Both limitations are the main problems in implementing this method in SEM. Since the SEM operates at a rather low energy, the potential use of phase holographic masks [5] is ruled out, while only the amplitude ones are applicable. Since such a diffraction experiment is highly nonstandard in SEM, one may encounter configurations where the optical aberrations become very strong. Therefore, one must set the system parameters carefully. For lower energies, the chromatic aberration may become important not only for imaging, but also for the coherence width determination, as can be shown by a direct calculation [6].

Some modifications of the standard SEM FEI Magellan 400L were made to achieve the setup shown in Figure 1. Namely an additional aperture strip with a set of vortex masks was put in the column and the standard electron beam aperture was modified to enable the beam separation (selection aperture - SA). The primary beam, after being diffracted by a vortex mask, is deflected in such a way that the selected vortex is passing through the SA, while the others are removed. The beam is then focused on a specimen by the objective lens. Using scanning coils above the SA, this aperture can be visualized by the diffracted beam, as it is shown at the brightness series in Figure 2. This may give a rough information about the beam itself. The images of tin balls acquired by the entire beam are shown in Figure 3, where we can see triple images separated by 1  $\mu\text{m}$ , which should be sufficient for some applications, even without the separation by the SA.

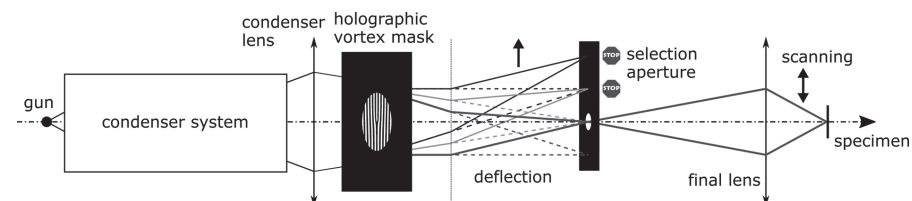


**Figure 1:** Optical setup of EVB creation – holographic reconstruction in SEM Magellan 400L.

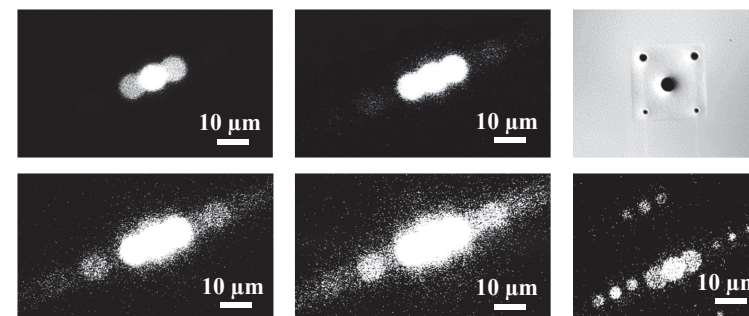


**Figure 2:** 1<sup>st</sup> and 2<sup>nd</sup> column: brightness series of the selection aperture illuminated by a diffracted beam. 3<sup>rd</sup> column: modified aperture and its image by a diffracted beam.  $E = 5$  keV.

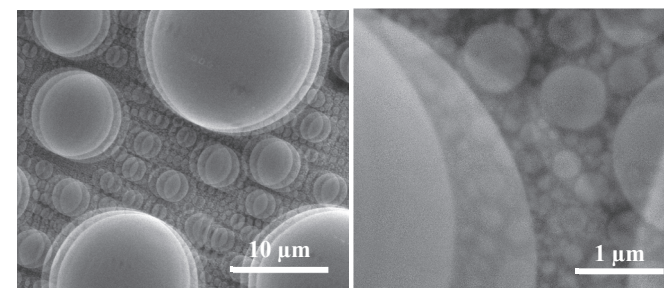


**Figure 3:** Images of tin balls acquired by the entire diffracted beam; primary energy of 5 keV.

### References:

- [1] Bliokh K., et al., Phys. Rev. Lett. **99** (2007) 190404.
- [2] Uchida M., Tonomura A., Nature **464** (2010) 737.
- [3] Verbeeck J., et al., Nature **467** (2010) 301.
- [4] Béché A., et al., Ultramicroscopy **178** (2017) 12.
- [5] Grillo V., Appl. Phys. Lett. **104** (2014) 043109.
- [6] Řiháček T. and Müllerová I., SIMDALEE2017, Pula (2017) 50.
- [7] We thank Bohuslav Sed'a and Libor Novák (Thermo Fisher Scientific) for help with experimental realization.
- [8] Financially supported by the TA CR (TE01020118), MEYS CR (LO1212), its infrastructure by MEYS CR and EC (CZ.1.05/2.1.00/01.0017). Partially supported by CEITEC Nano RI (MEYS CR, LM2015041).

## SECONDARY ELECTRON HYPER SPECTRAL IMAGING IN HELIOS NANOLAB – MAPPING MATERIALS PROPERTIES OR ARTEFACTS?

C. Rodenburg<sup>1\*</sup>, R. Masters<sup>1</sup>, K. Abrams<sup>1</sup>, M. Dapor<sup>2</sup>, S. Krátký & F. Mika<sup>3</sup>

<sup>1</sup>University of Sheffield, Material Sci. & Eng., Mappin Street, S1 3JD, Sheffield, UK

<sup>2</sup>European Centre for Theoretical Studies in Nuclear Physics and Related Areas (ECT\*-FBK) and Trento Institute for Fundamental Physics and Applications (TIFPA-INFN), Trento, Italy

<sup>3</sup>Institute of Scientific Instruments of the CAS, Královopolská 147, Brno, Czech Republic

\*e-mail: c.rodenburg@sheffield.ac.uk

A link between peaks in secondary electron (SE) spectra and Electron Energy Loss Spectra (EELS) was shown decades ago [1]. Also, materials properties (bulk modulus, band gap) correlate with the bulk plasmon position in EELS, and local modulus maps in carbon fibres have been presented [2]. If any features as result of plasmon decay into SE can be identified, SE spectroscopy combined with hyperspectral imaging could transform the SEM into a tool for mapping materials properties with ground-breaking potential for nanotechnology. To become a reality, we first need to establish SE collection conditions spectra that represent a material reliably. Second, we need to gain a better understanding of the processes involved in the SE emission processes.

Experimental SE spectra collection (primary beam energy of 1 keV) described in [3] was used on thin films (Ag & Cr) [4]. The Ag/Cr regions, identified by their width, are labelled in Fig.1 (a). A transition region, distinct due to its variation in grain structure is visible also in the BSE image (inset in Fig. 1(b)). Ag/Cr grains are surrounded by a low-density material. The SE spectrum covering all regions are shown in Fig. 1(a) as dashed line. In order to identify the low density material and obtain spectra representative of the metals, we plasma cleaned the specimen and collected the SE spectra of the same area (solid line, Fig. 1a). Peaks appearing with reduced intensity after plasma cleaning (in-chamber, 5 min) should reflect the contaminating material, while peaks with increased intensity should reflect the metals. Based on published SE spectra for C [5], Ag(110/111/100) [6] and Cr(110) [7] we identify contamination as C and attribute any fine structure to Ag and Cr (see labels in Fig. 1a). The peak at 7.8 eV is not affected at all and might be an artefact of the ‘spectrometer’. The origin of such artefacts will be discussed.

In Fig. 1b we present SE spectra from the Ag, Cr and interface region (after plasma cleaning). We find the best agreement (increased SE emission at the very low energy range) attributable to Ag(110/100). This contradicts the Monte Carlo (MC) data in [4], probably due to oxidation, or because the model does not account for crystal orientation. Orientation matters - the dashed spectrum in Fig.1(b) was obtained from the transition region and exhibits high intensity around 11.8 eV consistent with Ag(111). This feature is absent in the SE spectrum of the transition region before plasma cleaning, which instead has strong features above 13.1 eV that could stem from Cr or Ag(100) [7,8]. This change could have occurred if the SE spectra were collected from slightly different areas, as SE emission in the transition region strongly varies with location (see Fig.1a). To establish the origin of these effects and discrepancies between MC model and experiment requires further experiments and modelling taking account of crystal orientation effects.

That the molecular orientation (MO) is reflected in SE and was shown in [9]. Such effects can be included in the MC model [10] to some degree via suitable electron affinity, band gap and plasmon loss peak values. Fig.2(a) demonstrates that some of the observed MO effects on the peak appearance/ position can be explained in this way. Figure 2(b) demonstrates that the higher energy range, is expected to contain a weak signature of the sigma+pi plasmon peak, but further systematic modelling and experiments are needed to confirm this. Given all of the above we believe that further studies as outline above are necessary and justified in order to transform the SEM into a local materials properties test lab.

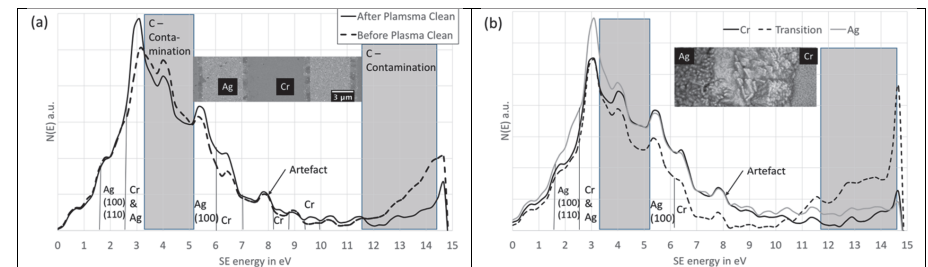


**Figure 1** Experimental SE spectra collected from Ag/Cr as described in text.

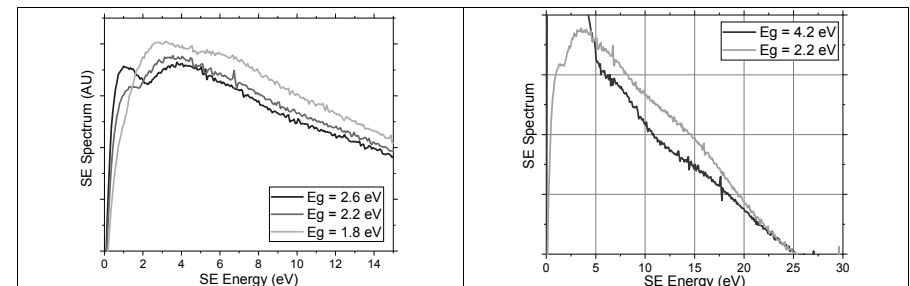


**Figure 2** MC Modelled SE spectra of P3HT, see text for details.

### References:

- [1] M.S. Chung & T.E. Everhart, *Physical Review B* **15** (10) (1970), p. 4699
- [2] R.H. Daniels, et al., *Ultramicroscopy* **96** (2002) p. 547
- [3] K. J. Abrams et al., *Phys. Status Solidi C* **14** (2017), p.1700153
- [4] F. Mika et al., *Proceedings 15th Int. Seminar, Skalský dvůr, Czech Rep., 2016*, p.36
- [5] K. Uneo, et al, *Japenese Journal of Applied Physics* **27** (5) (1988), p.L759
- [6] A. Otto, et al., *Physical Review B* **41** (14) (1990), p. 9752
- [7] H. Kato, et al., *Surface Science* **107** (1981), p. 20
- [8] V. A. Novolodski et al., *Technical Physics* **44** (7) (1999), 828
- [9] C. Rodenburg et al., *Proceedings 15th Int. Seminar, Skalský dvůr, Czech Rep., 2016*, p.58
- [10] M. Dapor, et al. *Journal of Electron Spectroscopy and Related Phenomena* **222** (2018), p. 95

## PROSPECTS AND RESULTS OF ATOMIC-RESOLUTION LOW-VOLTAGE TEM

H. Rose and U. Kaiser

Ulm University, Group of Electron Microscopy of Materials Science, Germany

The ultimate goal of low-voltage atomic-resolution analytical electron microscopy is the acquisition of quantitative data about the atomic structure, the chemical composition, and the local electronic states of thin electron-beam-sensitive objects including organic molecules. In order to prevent or reduce radiation damage, the microscope must operate at accelerating voltages below the knock-on threshold which is in the range between 20 kV and 80 kV for most radiation-sensitive objects. In order to obtain atomic resolution at such low voltages, it is mandatory to correct the spherical aberration of the objective lens and to either reduce the chromatic aberration by means of a monochromator or to eliminate it by Cc correction. Correction of Cc and Cs has been achieved by means of the novel corrector which is the principal component of the Sub-Angstrom Low-Voltage Electron (SALVE) microscope operating at electron energies in the range between 80 and 20 keV. The application of such low voltages increases the contrast and avoids (a) knock-on damage even in the case of low-Z materials and (b) prevents an appreciable reduction of resolution at lower electron energies. We will demonstrate this behaviour by showing that sub-Å resolution is achieved down to 40 keV in a wide field of view of 4000×4000 pixels. A resolution of 1.3 Å at 20 keV has been obtained making the tool predestined for in-situ studies of dynamic effects in low-dimensional materials at the atomic level. The correction of both spherical and chromatic aberration allows the use of most elastically and inelastic scattered electrons for image formation without loss of beam intensity resulting from monochromation. In combination with an imaging energy filter it is possible to form atomic-resolution EFTEM images using plasmon-loss or core-energy-loss electrons. The correction of spherical and chromatic aberrations opens up new opportunities for analytic imaging because inelastic scattered electrons within large energy windows are almost equally well focused at the image plane. Without chromatic correction the inelastic scattered electrons would be defocused according to their energy loss resulting in a strong loss of contrast and resolution.

Experimental results of the SALVE microscope will be presented which show that the interaction of the incident electrons with low-dimensional materials often results in changes of the atomic structure due to ionisation effects, which either prevent the imaging of the pristine state of the material or can be utilized for manipulating the structure on the atomic scale. Especially non-conducting materials suffer from ionization effects, which usually increase at lower voltages. Sophisticated sample preparation methods are then needed to reduce these effects. Promising means are the production of clean surfaces and sandwiching the radiation-sensitive material between two single sheets of graphene. First results show the feasibility of these object-protecting procedures.

The information limit of 90 pm at 40 kV corresponds to a maximum usable aperture angle of 67 mrad. Between 40 kV and 80 kV, sub-Angstrom resolution has been obtained. At 30 kV, the stability and resolution of the complete system (microscope and corrector) is more than sufficient to resolve single atoms in raw TEM images. At the current lowest-possible voltage of 20 kV the SALVE microscopes provides a resolution better than 0.14 nm which enables

near-atomic or even atomic imaging. This is a huge step forward towards materials analysis on delicate, beam-sensitive objects; the SALVE microscope now combines simultaneously the desired resolution with the use of beam energies below the knock-on threshold. Images of free-standing monolayers of graphene and MoS<sub>2</sub> taken at 30 kV show a strongly improved single-atom contrast in good agreement with simulations, as shown in Fig.1. In the raw experimental images (1s exposure time, 2048 × 2048 pixels frame size) the accumulated electron doses are 2.5·10<sup>6</sup> e<sup>-</sup>/nm<sup>2</sup> for graphene and 3·10<sup>5</sup> e<sup>-</sup>/nm<sup>2</sup> for MoS<sub>2</sub>, respectively.

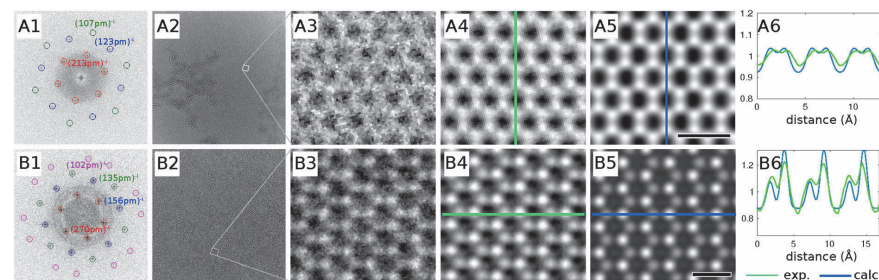


**Fig. 1:** Experimental and calculated Cc/Cs-corrected 30 kV HRTEM images of graphene (A) and MoS<sub>2</sub> (B). The resolution is determined from the diffractograms (A1 and B1) of the experimental raw images of graphene (A2) and MoS<sub>2</sub> (B2) in bright-atom contrast (field of view 40 nm × 40 nm). The magnified raw images (A3 and B3) identify the atomic structure. The averaged experimental images (A4 and B4) yield a strong improvement of the signal-to-noise and are in good agreement with the simulated images (A5 and B5) shown in the corresponding line profiles (A6 and B6). The size of the scale bars in A5 and B5 is 0.5 nm.

The SALVE microscope has recorded for the first time an image of an edge configuration in graphene shown in Fig. 2 by using a voltage of 30 kV. Because the edge configuration has a much lower knock-on threshold than graphene it cannot be imaged at appreciably higher voltages such as 80 kV. The superior performance of the SALVE microscope compared to present spherically corrected TEMs is documented in Fig. 3.

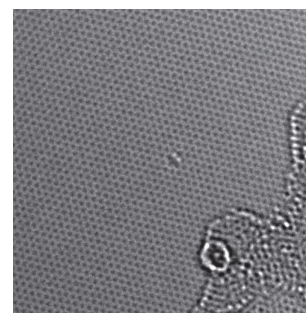


**Fig. 2:** Image of an edge of graphene recorded with the SALVE microscope at an acceleration voltage of 30 kV.

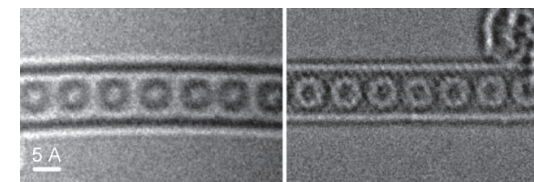


**Fig. 3:** High-resolution TEM images of C<sub>60</sub> molecules (fullerenes) embedded in single-walled carbon nanotubes, (left): image recorded in the Cs-corrected Titan at 80 kV, (right): image obtained Cs/Cc-corrected SALVE III TEM at 30 kV with an electron dose of 10<sup>6</sup> e<sup>-</sup>/nm<sup>2</sup> (J. Biskupek).

## GRAPHENE-BASED CATHODE COLD FIELD EMISSION SOURCES FOR ELECTRON MICROSCOPY AND LITHOGRAPHY

X. Shao<sup>1</sup>, W.K. Ang<sup>1</sup> and A. Khurshed<sup>1,2\*</sup>

<sup>1</sup>Department of Electrical and Computer Engineering, National University of Singapore, 4 Engineering Drive 3, Singapore 117583

<sup>2</sup>Engineering Science Programme, National University of Singapore, 9 Engineering Drive 1, Singapore 117575

\*e-mail: eleka@nus.edu.sg

Over the past decades, the extensive research work carried out on carbon-based cathodes for cold field emission, such as Carbon Nanotubes (CNTs), has not as yet, led to new viable electron sources for electron microscopy/lithography. Their most successful layout has typically been in the form of dots arrays for large area field emission applications. Nano size emitter single point cathodes have proven to have even more severe problems than conventional single-crystal tungsten cathodes: unmanageably stringent UHV requirements, relatively large current stabilities, and rapid emission decay. These difficulties have prevented the widespread use of cold field emission electron sources for electron microscopy and lithography applications.

This paper reports a cold field emission electron source which overcomes these problems based upon using a graphene-coated nickel (Graphene-Ni) wire point-cathode in the sub-micron to micron size [1]. Figure 1a shows a typical scanning electron microscope (SEM) image of the Graphene-Ni field emitter. Preliminary results, as shown in Figure 1b, show that graphene coated on a Ni sharpened tip dramatically lowers the work function of graphene (by over a factor of 4), enabling it to both provide stable field emission at cathode-tip electric field strengths as low as  $0.5 \text{ V nm}^{-1}$ , an order of magnitude lower than conventional single crystal tungsten point cathodes. This makes it possible to both operate the cathode in high vacuum (HV) conditions ( $4 \times 10^{-8}$  Torr) and use relatively large cathode-tip sizes (micron sizes), over three time larger than conventional single crystal tungsten tip sizes, sizes that are comparable to the Schottky field emitter tip. Plotted in Figure 1c is the reduced brightness versus energy spread for three different emitters, shown alongside the state-of-the-art tungsten cold field emitter and Schottky emitter. The estimated reduced brightness, as well as their measured energy spread, are comparable to conventional single crystal tungsten cathode cold field emission sources.

Another development is that a micron sized smooth-edged graphene ring-cathode without any observable collapses [2] has been successfully fabricated, as shown in Figure 2a. By leaving a thin layer of chemically adsorbed Ni nanoparticles (Figure 2b) by additional  $\text{Ga}^+$  ion beam irradiation, the ring source is found to have a low work function of 2.77 eV and is more resistant to damages caused by ion back-bombardment in the HV conditions. Figure 2c presents the current ( $I$ ) passing through the anode aperture as a function of applied voltage ( $V$ ) curves, recorded from the individual graphene ring-cathode (blue rectangle) and GR-Ni emitter (orange pentagon). The turn-on voltage from the GR-Ni ring-cathode emitter with one order of magnitude thicker emission edges is about 60% higher than of that from the graphene

ring-cathode emitter. However, the overall emission current from the GR-Ni ring-cathode emitter is approximately one order of magnitude lower. Ring-cathode electron sources can be used in focused beam columns to image ring patterns on a sample directly, without the need to employ a projection mask or a scanning unit. Numerical simulation with direct ray tracing modelling is carried out to study the ring image characteristics of a ring-cathode focusing column as compared to that of a conventional point source electron beam focusing column using an annular aperture, and this will be given in a separate paper by W.K. Ang and A. Khurshed.

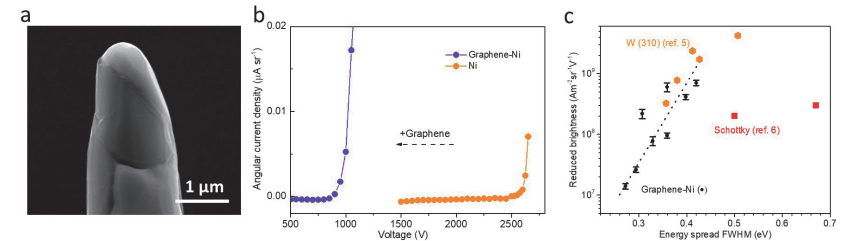


**Figure 1** (a) SEM image of a Graphene-Ni field emitter. (b) The angular current density-voltage trace from the Ni tip with a tip radius of 700 nm before coating with graphene (orange), and after coating with graphene (violet). (c) Reduced brightness versus energy spread and state-of-the-art electron sources.

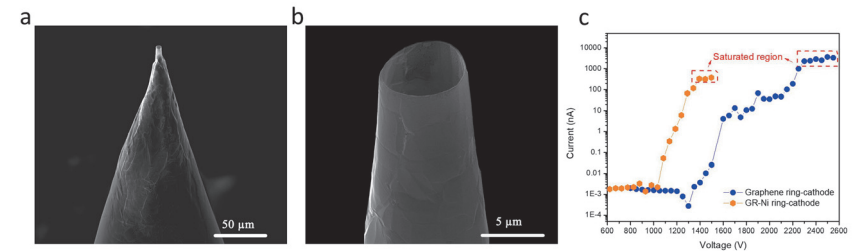


**Figure 2** (a) SEM image of concentric graphene ring-cathode field emitter (at low magnification). (b) SEM image of the graphene ring decorated with Ni nanoparticles (GR-Ni emitter). (c) Field emission characteristics of the graphene ring-cathode and GR-Ni ring-cathode.

### References:

- [1] X. Shao, A. Srinivasan, W.K. Ang and A. Khurshed, *Nature Communications* **9** (2018), 1288.
- [2] X. Shao, A. Srinivasan, Y. Zhao and A. Khurshed, *Carbon* **110** (2016), 378-383.
- [3] This work is funded by the National Research Foundation (NRF) Competitive Research Programme (CRP) award # NRFCRP13-2014-04 titled "Micro-fabricated Ring Carbon Nanotube electron/ion sources"

## THICKNESS DETERMINATION OF A CATHODOLUMINESCENCE ACTIVE NANOPARTICLES BY MEANS OF QUANTITATIVE STEM IMAGING

R. Skoupy<sup>1\*</sup> and V. Krzyzanek<sup>1</sup>

<sup>1</sup>The Czech Academy of Sciences, Institute of Scientific Instruments, Královopolská 147, 612 64, Brno, Czech Republic.

\*e-mail: ras@isibrno.cz

Labeling of specimens by nanoscale probes is common approach of complex biological systems exploration. Namely gold nanoparticles immuno-staining is well established method in electron microscopy. However, if more than two label sizes are used, the differentiation of individual nanoparticles becomes difficult.

This can be overcome by cathodoluminescence (CL) active particles – nanophosphors where labels recognition is done by wavelength of emitted light. This gives a great opportunity to use advanced multi probe labeling within one sample.

There is a huge variety of nanophosphors: green fluorescent protein, quantum dots, ZnO nanoparticles, organic molecules, rare earth-doped nanophosphors etc. [1] Therefore, in order to choose best type of nanophosphors for a given task, it is important to measure particles size/thickness, as the CL intensity is proportional to the probe volume.

We present a new method for investigation of the individual nanophosphor particles by the combination of STEM in the bright field and the CL imaging. Data were captured at the SEM Magellan (FEI) equipped by the retractable STEM 3 detector and the CL detector MonoCL4 Plus (Gatan). The sample is cooled down to -145°C by the cryo stage (Leica Microsystems).

Cooling down brings three advantages: It eliminates carbon contamination of the sample caused by imperfect vacuum; the CL signal yield is increased at cryo temperatures and drift of the sample caused by a primary electron beam is reduced. All together it brings superior and more repeatable results in comparison with room temperature imaging.

The STEM images (captured in field free mode of the microscope) were calibrated via the full-beam and the blank-beam images. In this step, images of the detector at the lowest possible magnification (in our case 50x) are captured. Irradiated area of an active STEM detector segment is detected and a mean signal response of the detector is calculated. Background is determined as the mean value of all pixels in the image, where electron beam is blanked. The results of calibration process are used for following data normalization and mass/thickness determination.

Such normalized data (ranging from 0 to 1) are compared with a Monte Carlo simulation of the sample calculated in the electron trajectory simulation software CASINO [2]. All procedures were programmed in Matlab (Mathworks) according to the methods described in Krzyzanek et al. [3].

The YAG:Ce nanoparticles (density 4.5 g/cm<sup>3</sup>) for the imaging were localized on carbon (9 nm thick) coated TEM grids. The bright-field STEM image (Fig. 1a) shows a cluster of the particles with sizes in range from 30 to 60 nm. The thickness of the particles was unknown as well as their size in the z-direction. The map of calculated thicknesses (Fig. 1c) indicates areas with one, two and/or three layers arrangement. Very similar layout can be clearly seen at the CL image, where the bright areas correspond with thick areas of the sample.

Resulting *sample thickness/CL activity ratio* (Fig. 2) of the YAG:Ce nanoparticles shows linear dependence between these quantities. We assume, that slope of this ratio is sample dependent and many types of the CL active compounds can be characterized by this unique method. Moreover, such knowledge can be used for selection of suitable CL active probes (optimal sizes and compositions) for a practical labeling of biological systems.

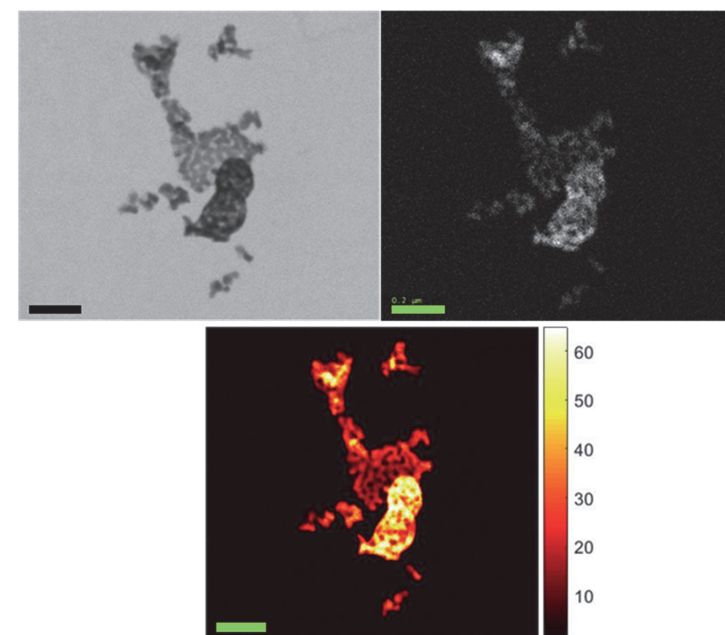


**Figure 1** The YAG:Ce nanoparticles on thin carbon covered lacy carbon grid. (a) The bright field STEM image. (b) The CL image (acceleration voltage: 30 kV, probe current: 6.3 pA, pixel time: 100 ms, panchromatic mode). (c) The thickness map created by the quantitative imaging (colorbar in nm). Bar 200 nm.

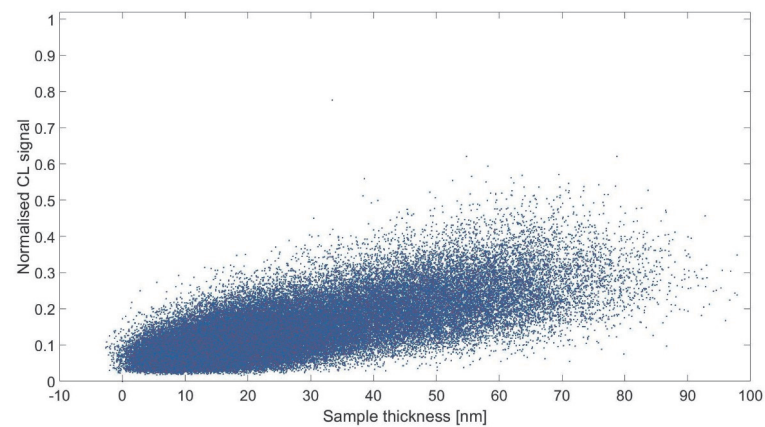


**Figure 2** The thickness / CL activity ratio of the YAG:Ce nanoparticles. The CL intensity is normalised to the maximum number of counts captured in the image. The thickness is relative to the sample. The area of thicknesses lower than zero is related to the carbon support film.

#### Acknowledgement:

The research was supported by the Czech Science Foundation (project 17-15451S), Ministry of Education, Youth and Sports of the Czech Republic (project LO1212). The research infrastructure was funded by Ministry of Education, Youth and Sports of the Czech Republic and European Commission (project CZ.1.05/2.1.00/01.0017) and by the Czech Academy of Sciences (project RVO:68081731).

#### References:

- [1] Furukawa T., Niioka H., Ichimiya M. et al. *Optics Express* **21(22)** (2013), p. 25655-25663.
- [2] Demers H., Poirier-Demers N., Réal Couture A. et al. *Scanning* **33(3)** (2011), p. 135-146.
- [3] Krzyzanek V. et al. *Journal of Structural Biology* **165** (2009), p. 78-87.

## ORBITAL MOTION FROM OPTICAL SPIN: THE EXTRAORDINARY MOMENTUM OF CIRCULARLY POLARIZED LIGHT BEAMS

V. Svak<sup>1\*</sup>, O. Brzobohatý<sup>1</sup>, M. Šiler<sup>1</sup>, P. Jákl<sup>1</sup>, P. Zemánek<sup>1</sup>, S. Simpson<sup>1</sup>

<sup>1</sup>Institute of Scientific Instruments of the CAS, v. v. i., Královopolská 147, 612 64, Brno, Czech Republic

\*e-mail: svakvo@isibrno.cz

The momentum of light, and the radiation pressure forces to which it gives rise, are usually thought to act parallel to the direction of propagation. However, recent work has indicated the existence of a spin,  $\mathbf{S} = \frac{1}{2\omega} \text{Im}[\mathbf{E}^* \times \mathbf{E}]$ , dependent component to the momentum,  $\mathbf{p}^s = \frac{1}{2} \nabla \times \mathbf{S}$  and an associated spin force,  $F^{spin} \propto p^s$ , that arise in inhomogeneous light fields [1]. Spin  $\mathbf{S}$  is given by ellipticity of the polarization of light and spin force tend to act in transverse directions. Experimental observation of this force is experimentally challenging. Spin momentum requires field inhomogeneities which inevitably generate other forms of optical forces, including gradient forces. Measuring its effects, relatively subtle spin forces must be reliably distinguished from other, stronger forces. This was achieved in a recent experiment in which the deflection of a nano-cantilever, immersed in a circularly polarized evanescent field was measured [2]. Other experiments involve analysis of motion of particles in liquid, subject to appropriate light fields [3].

In contrast, our experiments are striking and unequivocal. Ultimately, we observe the violent ejection of a probe particle from an optical trap, as a direct consequence of transverse spin momentum. We trap a silica microsphere (1,54  $\mu\text{m}$  diam.) in counter-propagating Gaussian beam trap, in vacuum (Fig. 1a). This symmetric geometry nullifies the axial scattering forces associated with each beam and emphasizes transverse components, when they are present.

A series of distinct regimes of motion are observed, depending on polarization of the light and optical power  $P$  for given ambient pressure of 4 mbar. First, we consider small optical power, thus small displacements. For small displacements of a microsphere from the center of the trap, the trap can be quantified by stiffness coefficient,  $K = kP$ , which is directly proportional to the optical power. In the overdamped regime, we see Brownian motion which complies with the equipartition theorem. The elastic and thermal energies of the trap can be equated,  $\frac{1}{2}k_B T = \frac{1}{2}K\langle x^2 \rangle = \frac{1}{2}kP\langle x^2 \rangle$  so that the position variance is inversely proportional to the power,  $P\langle x^2 \rangle = \text{const.}$ . Precisely the same behaviour is seen in the under-damped regime, when we use linear polarization (LP) (Fig. 1d). However, this equipartition theorem does not remain valid for circularly polarized beams (CP). Subtle deviations from equilibrium position, due to Brownian motion, allow the particle to accumulate momentum in azimuthal direction, dramatically altering the dynamics and giving rise to substantial departures from equilibrium behavior and from equipartition.

If the optical power is increased further, the particle begins to execute sustained deterministic orbits about the beam axis. As the bead orbits, azimuthal spin forces are balanced by viscous drag, gradient forces act as centripetal forces (Fig. 1b). Since the ratio of azimuthal and radial force is approximately constant with optical power, the orbit radius increases monotonically with optical power (Fig. 1e), and the frequency of the orbit is approximately independent of optical power. Ultimately, increases in optical power result in these orbits destabilizing before the particle is completely ejected.

This system acts both as a powerful demonstration of spin momentum and spin forces, and as a test bed for elementary non-equilibrium thermodynamics.

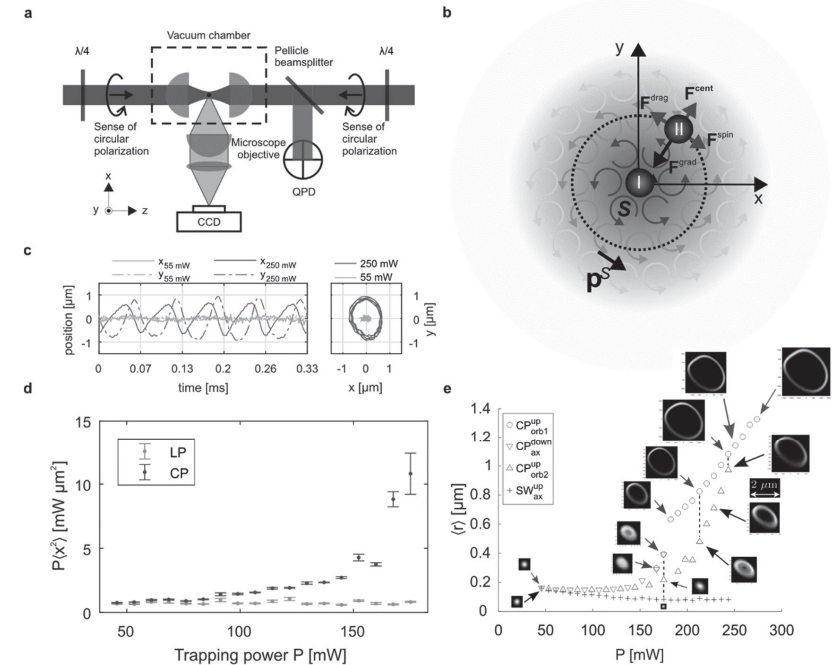


**Figure 1** a) Experimental setup. b) Section of Gaussian trapping beams showing forces acting on probe particle. Spin momentum  $p^s$  is perpendicular to propagation direction. In CP beams two regimes of motion are observed: I – biased Brownian motion (lighter line in picture c) and II – deterministic orbiting (darker line in picture c) d) Validity of equipartition for linearly polarized and circularly polarized optical trap. e) Mean orbit radius as a function of trapping power  $P$ .

### References:

- [1] Konstantin Y. Bliokh, Aleksandr Y. Bekshaev, Franco Nori, *Nature Communications* **5**, 3300 (2014)
- [2] M. Antognozzi, C. R. Bermingham, R. L. Harniman, S. Simpson, J. Senior, R. Hayward, H. Hoerber, M. R. Dennis, A. Y. Bekshaev, K. Y. Bliokh, F. Nori, *Nature Physics* **12**, 731–735 (2016)
- [3] Angelsky, O. V. *et al.* Orbital rotation without orbital angular momentum: mechanical action of the spin part of the internal energy ow in light beams. *Opt. Express* **20**, 3563–3571 (2012).

### Acknowledgements:

The research was supported by CSF (project GB14-36681G), MEYS CR (LO1212), its infrastructure by MEYS CR and EC (CZ.1.05/2.1.00/01.0017) and by CAS (RVO:68081731).

## GRAZING INCIDENCE INTERFEROMETER FOR FORM MEASUREMENT OF HOLLOW CYLINDERS

M. Sarbort\*, S. Rerucha, M. Hola and J. Lazar

The Czech Academy of Sciences, Institute of Scientific Instruments  
Kralovopolska 147, 612 64 Brno, Czech Republic  
\*e-mail: martins@isibrno.cz

Optical metrology of cylindrical specimens represents an interesting task in scientific and industrial practice. The most precise measurement methods use principles of laser interferometry where the phase difference between the reference wave and the object wave reflected from the tested surface is detected. The form measurement of hollow cylindrical tubes can be advantageously realized by an object wave with conical wavefronts generated by an axicon lens or an equivalent diffractive optical element. An axicon characterized by large apex angle forms a conical wave that fulfills the conditions of the grazing incidence, which results in suppression of the speckle noise. The previous experimental setups [1-4] were relatively complex since they involved a pair of mutually reversed axicons or a pair of diffractive optical elements that transform the object wave from planar to conical and vice versa.

In this paper we describe a new grazing incidence interferometer for the form measurement of hollow cylindrical tubes with the desired accuracy in the micrometer range [5]. It is based on a simple and robust optical setup where the reference and object waves correspond to the central and peripheral parts, respectively, of the conical wave generated by a single axicon (see Fig. 1). The imperfection of the axicon tip resulting in an additional unwanted nearly-spherical wave propagating through the optical setup is eliminated by a telescope formed by two lenses and a spatial filter. The interference between the reference wave and the object wave reflected from the inner surface of the cylindrical tube is detected by a CCD camera as an annular interferogram that is characterized by a closed-fringe pattern with a circular carrier (see Fig. 1). The interference phase is computationally demodulated using the spatial synchronous detection method. In addition, the correction of misalignment aberrations is done by an iterative computational procedure. As a final result we calculate the surface shape deviation of the tested tube from an ideal cylinder. The interferometer was experimentally tested for the specimens of the glass and stainless steel tubes with inner diameter of 9 mm and lengths from 220 mm to 600 mm. The tube deformations such as ellipticity or longitudinal bend were detected (see Fig. 2). The achieved combined measurement uncertainty of 4.4 micrometers was primarily given by the wavefront quality of the used conical wave. Further reduction of the measurement uncertainty is possible by the calibration of the interferometer using an optical etalon.

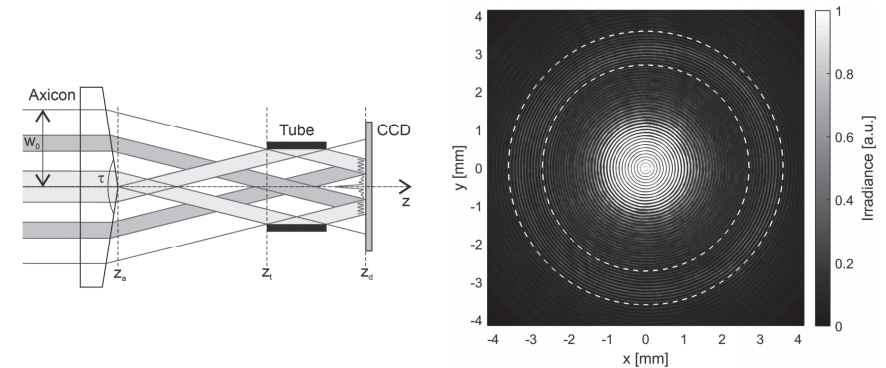


**Figure 1** Optical setup of the grazing incidence interferometer with the indicated object and reference waves (left). Irradiance pattern detected by the CCD camera (right), the interferogram annulus is bounded by the dashed-line circles.

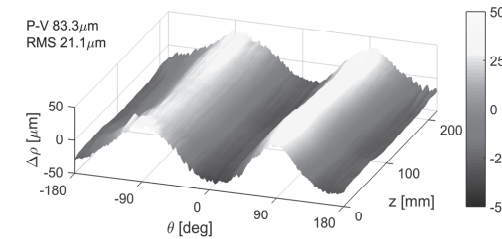


**Figure 2** Surface shape deviation for the glass tube with inner diameter of 9 mm and length 220 mm. The plot indicates that the transverse profile of the tube is elliptical.

### Acknowledgment:

The research was supported by Technology Agency of the Czech Republic (project TE01020233), Ministry of Education, Youth and Sports of the Czech Republic (project LO1212). The research infrastructure was funded by Ministry of Education, Youth and Sports of the Czech Republic and European Commission (project CZ.1.05/2.1.00/01.0017) and by The Czech Academy of Sciences (project RVO:68081731).

### References:

- [1] Dresel T., Brinkmann S., Schreiner R. and Schwider J., *J. Opt. Soc. Am. A*, **15** (1998), p. 2921–2928
- [2] Brinkmann S., Dresel T., Schreiner R. and Schwider J., *Appl. Opt.* **38** (1999), p. 121–125.
- [3] Schreiner R., Beyerlein M., Harder I., Dresel T., Lindlein N. and Schwider J., *Appl. Opt.* **41** (2002), p. 64–69.
- [4] Belyi V., Kroening M., Kazak N., Khilo N., Mashchenko A. and Ropot P., *Proc. SPIE* **5964** (2005), p. 59640L.
- [5] Sarbort M., Rerucha S., Hola M., Buchta Z. and Lazar J., *Appl. Opt.* **54** (2015), p. 9930–9938.

## IMAGING VIA MULTIMODE OPTICAL FIBER: RECOVERY OF A TRANSMISSION MATRIX USING INTERNAL REFERENCES

M. Šiler<sup>1\*</sup>, P. Ják<sup>1</sup>, J. Traegaardh<sup>1</sup>, J. Ježek<sup>1</sup>, H. Uhlířová<sup>1</sup>, T. Tučková<sup>1</sup>, P. Zemánek<sup>1</sup>, and T. Čižmár<sup>1,2</sup>

<sup>1</sup>The Czech Academy of Sciences, Institute of Scientific Instruments, Department of Microphotonics, Brno, 612 64, Czech Republic

<sup>2</sup>Leibniz Institute of Photonic Technology, Jena, 07745, Germany

\*e-mail: siler@isibrno.cz

Current research of life shows a great desire to study the mechanics of biological processes directly within the complexity of living organisms. However, majority of practical techniques used nowadays for tissue visualization can only reach depths of a few tens of micrometres as the issue obscures deep imaging due to the random light scattering. Several imaging techniques deal with this problems from different angles, such as optical coherence tomography, light sheet microscopy or structured light illumination. A different and promising strategy to overcome the turbid nature of scattering tissues is to employ multimode optical fibers (MMF) as minimally invasive light guides or endoscopes to provide optical access inside [1,2]. Although the theoretical description of light propagation through such fibers has been developed a long time ago it is frequently considered inadequate to describe real MMF. The inherent randomization of light propagating through MMFs is typically attributed to undetectable deviations from the ideal fiber structure. It is commonly believed that this additional chaos is unpredictable and that its influence grows with the length of the fiber. Despite this, light transport through MMFs remains deterministic and can be characterized by a transmission matrix (TM) which connects the intensity and phase patterns on the fiber input and output facets. Once the TM is known it can be used to create focus in any desired 3D coordinates beyond the distal fiber facet, see figure 1, and perform e.g. fluorescence based laser scanning microscopy [3] or optical trapping [4].

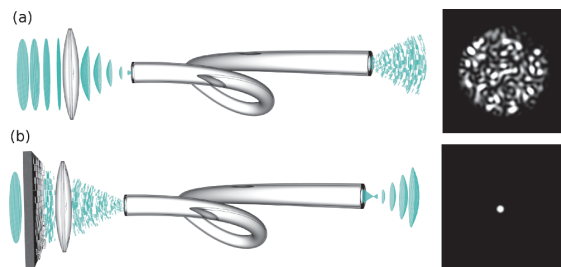


**Figure 1** (a) Light passing through the MMF creates a speckled pattern upon leaving the output fiber facet. (b) Properly designed and shaped (by spatial light modulator) input light creates a single focused spot close to the output fiber facet.

Therefore, a calibration step of measuring TM is needed in order to achieve any imaging technique. This is done by projecting a convenient pattern of the fiber input facet (co called

input mode) by a spatial light modulator and by measuring the output patterns. In order to recover both intensity and phase maps, i.e. the whole complex TM, a phase shifting interferometry is used. I.e. the TM is obtained by using the interference of light passing through fiber with a coherent reference beam externally guided to a CCD camera. Therefore, a complex optical pathways are required together with the compensation of mechanical drift between the signal and the reference optical pathways. These limitations can be lifted by using an internal reference signal (propagating through MMF) in a form of an arbitrarily chosen input mode. However, the output signal of such internal reference takes a shape of a random speckle pattern at the detector. Inherently, places of low light intensity (blind spots) are present and in such a spot the phase shifting interferometry fails to return reasonable information. Here we present a method that combines several TM measurements obtained for different internal references. The distribution of blind spots is unique for each internal reference and therefore combining multiple TMs while eliminating affected TM data leads to comparable performance as if measurements are obtained with the external reference, see Figure 2.

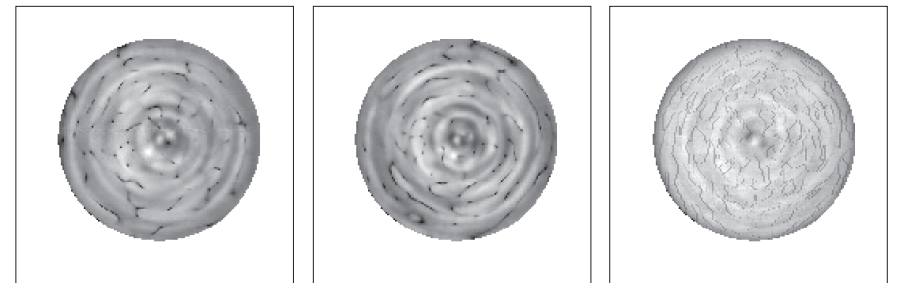


**Figure 2** Intensity of all the output MMF modes obtained by calibration with internal references. Left, Center: Intensity patterns obtained using a single reference mode, for two different reference modes. Right: Intensity pattern obtained using 5 reference modes.

Obtaining the transmission matrix using internal references of multimode optical fiber offers considerable advantages in simplifying the experimental setup of the endoscope. It is however required to use multiple reference modes of the fiber in order to suppress the blind spots caused by the specked patterns of fiber output. This may significantly increase the time needed for the calibration procedure. However, with the use of fast spatial light modulator based on MEMS technology this experimental delay becomes insignificant.

The research was supported by European Structural and Investment Funds Project “Holographic endoscopy for in vivo applications” (No. CZ. 02.1.01/0.0/0.0/15\_003/0000476) and MEYS CR (LO1212); its infrastructure by MEYS CR and EC (CZ.1.05/2.1.00/01.0017) and by CAS (RVO:68081731).

### References:

- [1] T. Čižmár, K. Dholakia, *Optics Express* **19** (2011), 18871.
- [2] T. Čižmár, K. Dholakia, *Nature Communications* **3** (2012), 1027
- [3] M. Ploeschner et al., *Nature Photonics* **9** (2015), 529
- [4] I. T. Leite et al., *Nature Photonics* **12** (2018), 33, 2018

## LOCKING IN ON LARGE VOLUME LIGHT-SHEET MICROSCOPY

T. Vettenburg<sup>1,2,5\*</sup>, H.I.C. Dalgarno<sup>2</sup>, J. Nylk<sup>2</sup>, C. Coll-Lladó<sup>3</sup>, D.E.K. Ferrier<sup>3</sup>, T. Cizmar<sup>4</sup>, F.J. Gunn-Moore<sup>3</sup>, and K. Dholakia<sup>2</sup>, A. Corral<sup>5</sup>, A. Rodríguez-Pulido<sup>6</sup>, C. Flors<sup>6</sup>, and J. Ripoll<sup>5</sup>

<sup>1</sup>School of Science and Engineering, Physics, University of Dundee, UK

<sup>2</sup>School of Physics and Astronomy, <sup>3</sup>Biology, <sup>4</sup>Medicine, University of St Andrews, UK

<sup>5</sup>Dept. Bio. and Aerospace Eng., Universidad Carlos III de Madrid, 28911 Madrid, Spain

<sup>6</sup>Madrid Institute for Advanced Studies in Nanoscience, Madrid, Spain

\*e-mail: t.vettenburg@dundee.ac.uk

Fluorescence light-sheet microscopy is increasingly adopted by developmental biologists to study how cells divide and differentiate to form organs and even entire organisms. The light-sheet microscope differs from a conventional microscope in that the specimen is illuminated by a plane of light orthogonal to the detection axis, thus keeping the out-of-focus areas dark while minimizing any potentially detrimental exposure of the sample. The light-sheet microscope has been found to be the ideal instrument for long-term and non-invasive studies of intact, and therefore three-dimensional, fluorescent samples.

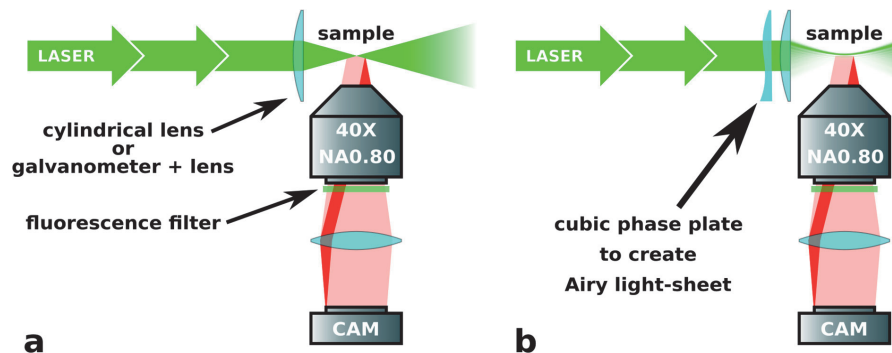


**Figure 1 a.** The conventional light-sheet fluorescence microscope. A laser (green) is focused into the focal plane of the sample by a cylindrical lens. The emitted fluorescence (red) is collected by the objective and reimaged onto the camera (CAM). **b.** The Airy light sheet microscope introduces a cubic phase mask in the illumination path to form a propagation-invariant Airy light sheet. The asymmetry of its profile enables high-resolution image reconstruction over a ten-fold larger field-of-view.

While the light-sheet microscope is able to rapidly image larger specimen such as the developing zebrafish, this comes with a trade-off between resolution and field-of-view. Diffraction prevents the conventional light-sheet, created by focusing a Gaussian beam in one dimension, to a thin plane throughout the entire width of the sample (**Figure 1a**). High axial resolution can only be obtained near the beam waist, while other regions suffer from reduced axial resolution and increased out-of-focus blur. Solutions such as two-photon excitation and blocking of the out-of-focus light by a confocal slit require a significant increase in sample exposure. This overturns one of the key advantages of the light-sheet microscope. We demonstrate how the asymmetric beam profile of the Airy beam can overcome the trade-off

between axial resolution and field-of-view without having to sacrifice the scarce fluorescence signal and without relying on the high, often photo-bleaching and damaging, peak-powers that are associated with two-photon excitation. The Airy light-sheet method enables sub-cellular resolution throughout a ten-fold larger volume [1].

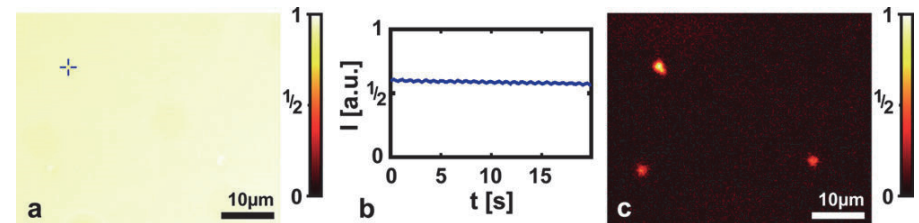


**Figure 2** Exploiting reversible photo-switching in light-sheet microscopy. Microspheres labeled with the reversible photo-switchable protein rsEGFP within a highly fluorescent medium. **a.** Conventional light-sheet image. **b.** The fluorescence intensity fluctuations, in lock-step with the laser, at the pixel indicated by the cross-hair in the left panel. **c.** Photoswitching-enabled contrast enhancement of the light-sheet image. Reprinted with permission from [3]. Copyright 2017 American Chemical Society.

A larger imaging volume also brings new challenges to the fore. The natural inhomogeneity of biological specimen leads to optical aberrations and scattering that quickly become significant when imaging through multiple layers of cells. Conventional light-sheet microscopy is thus mostly useful with quasi-transparent specimen such as the zebrafish (*Danio rerio*); however, biological samples are more often than not turbid or opaque to light. Moreover, indigenous auto-fluorescence of many biological tissues may severely reduce contrast and hamper the correct interpretation of the light-sheet microscopy images.

We demonstrate how a high resolution light-sheet can be formed within turbid samples by *in situ* correction of the wavefront to achieve high axial resolution even in turbid samples [2]. We further show (**Figure 2**), how the state of photo-switchable fluorophores can be controlled to single-out the structures of interest from the auto-fluorescence background [3]. This enables high contrast and resolution, even under the adverse conditions of turbid, highly auto-fluorescent, samples.

References:

- [1] T. Vettenburg, H.I.C. Dalgarno, J. Nylk, C. Coll-Lladó, D.E.K. Ferrier, T. Cizmar, F.J. Gunn-Moore, and K. Dholakia *Light-sheet microscopy using an Airy beam*, *Nature Methods* **11** (2014), p. 541–544. doi:10.1038/nmeth.2922
- [2] H.I.C. Dalgarno, T. Cizmar, T. Vettenburg, J. Nylk, F.J. Gunn-Moore, and K. Dholakia, *Wavefront corrected light sheet microscopy in turbid media*, *Applied Physics Letters* **100**, (2012) p. 191108. doi:10.1063/1.4710527
- [3] T. Vettenburg, A. Corral, A. Rodríguez-Pulido, C. Flors, and J. Ripoll, *Photoswitching-Enabled Contrast Enhancement in Light sheet Fluorescence Microscopy*, *ACS Photonics* **4** (2017), p. 424-428. doi:10.1021/acsp Photonics.6b00838

## INELASTIC MEAN FREE PATH FROM RAW DATA MEASURED BY LOW-ENERGY ELECTRONS TIME-OF-FLIGHT SPECTROMETER

M. Zouhar<sup>\*1</sup>, T. Radlička<sup>1</sup>, M. Oral<sup>1</sup> and I. Konvalina<sup>1</sup>

<sup>1</sup>Institute of Scientific Instruments of the CAS, v. v. i. (ISI CAS), Královopolská 147, 612 64, Brno, Czech Republic

\*e-mail: zouharm@isibrno.cz

The inelastic mean free path (IMFP) is a key parameter of electron transport in a solid. With the rise of so-called meta-materials, materials of specific shape, such as 2D crystals, or materials with tailored functionality for next-generation electronic devices, the investigation of the IMFP is still topical and of high importance [1]. This is true especially at low energies, landing energy of electrons below 100 eV, that are hard to study using well established techniques of electron spectroscopy.

The time-of-flight (TOF) spectrometer developed at the ISI CAS [2, 3] is a scanning transmission electron microscope that can also operate in a TOF mode with the landing energy below 300 eV.

The TOF operation mode in a nutshell is: For each pixel on the sample, equidistant electron pulses are emitted towards the pixel position. Pixels are switched periodically (switch time denoted as  $t_{px}$ , recorded). An electron pulse emitted from the electron gun ( $t_{pulse}$ , recorded) travels to the sample. Transmitted electrons leave the sample ( $t_{transmit}$ , not recorded) and travel through a drift-tube, finally hitting the detector ( $t_{detect}$ , recorded). The nature of the recorded events is specified by the number of channel from which the event is received by the detector. Because the primary electrons are decelerated very close to the sample, the propagation time above the sample  $t_{offset} = t_{transmit} - t_{pulse}$  will be very small when compared to the TOF, propagation time below the sample  $t_{for} = t_{detect} - t_{transmit}$ . The time the electrons spend in the thin sample can be neglected.

The input for the data processing and the processing can be separated into two types – the setting of the voltages at different components and the recorded times  $t_{pulse}$  and  $t_{detect}$ .

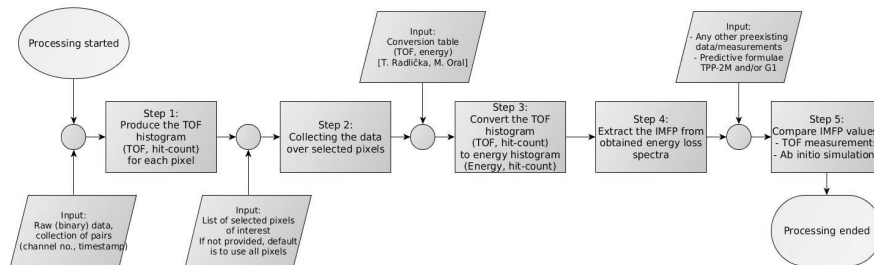


**Figure 1** TOF data processing work-flow.

The processing work-flow is depicted in Fig. 1 and the plan is that it should consist of five steps. The first three are written in-house in Python, unless explicitly mentioned otherwise.

1. *Obtain a TOF time histogram from the raw data, pixel-by-pixel.* This is done by processing files corresponding to different pixels in parallel. Consider a pair of emission ( $t_{pulse}$ ) and detection ( $t_{detect}$ ) events. Because  $t_{transmit}$  is not measured, we need to estimate  $t_{offset}$  in order to calculate  $t_{TOF}$ . The value of  $t_{offset}$  is estimated from measurements without the sample with predicted  $t_{TOF}$  subtracted from the difference  $t_{detect} - t_{pulse}$ . The processing scripts treat  $t_{offset}$  as a configurable input. Hence the TOF is  $t_{TOF} = t_{detect} - t_{pulse} - t_{offset}$ .

2. *Sum up the data to a cumulative TOF histogram corresponding to selected pixels.* The individual pixels to be selected from the collected data can be determined from the sample image obtained in the “standard” electron microscope mode; this allows to select a region with a high quality of the sample and/or with another properties of interest.

3. *Convert to an energy histogram.* This requires theoretical modeling of electron trajectories in the electrostatic field produced by voltages set on relevant components of the TOF spectrometer. The modeling is performed using combined forces of EOD [4], Matlab and C-code. The modeling tool provided by T. Radlicka (EOD and Matlab) and M. Oral (C-code, tracing library) accepts different energies and different angles to generate a set of trajectories for the transmitted electrons. In reality, the modeling is used to determine optimal values of the voltage at individual components of the TOF spectrometer prior the measurement. Optimal means that a reasonable compromise between the maximal achievable signal/noise ratio (maximum trajectories of transmitted electrons end at the detector) and the minimum angular dispersion in energy is achieved (the TOF spectrometer does not directly record angular dependence of the trajectories).

4. *Extract the physical information, namely the IMFP.* This part is in preparation and it will use theoretical models described in [5, 6].

5. *Perform ab initio simulations and compare predicted and measured IMFP.* The plan is to use free simulation codes Quantum-Espresso [7] or Abinit [8] and Yambo [9] and perform the calculations using resources of MetaCentrum and/or CERIT-SC [10].

This five-step processing will allow us to measure the IMFP at low energies for thin samples.

**Acknowledgement:** Co-funded by the project No. TE01020118 supported by TACR. Computational resources were provided by the CESNET LM2015042 and the CERIT Scientific Cloud LM2015085, provided under the programme "Projects of Large Research, Development, and Innovations Infrastructures".

### References:

- [1] Guo H., Gao J., Ishida N., Xu, M., and Fujita D.: Appl. Phys. Lett. **104** (2014) 031607.
- [2] Daniel B., Radlička T., Piňos J., Frank L. and Müllerová I.: Proceedings of 15th International Seminar Skalský dvůr (2016), p. 6-7.
- [3] This proceedings, companion contribution by Daniel B. *et al.*
- [4] Zlámal J., Lencová B., Nucl. Instr. Meth. A **645** (2011), p. 278-282.
- [5] Werner W S. M.: Surf. Interface Anal. **31** (2001) p. 141–176.
- [6] Werner W S. M.: Phys. Rev. B **74** (2006) 074521.
- [7] Project web-site: <http://www.quantum-espresso.org/>
- [8] Project web-site: <https://www.abinit.org/>
- [9] Project web-site: <http://www.yambo-code.org/>
- [10] Project web-site: <https://www.metacentrum.cz/en/>

# Delong Instruments

Low Voltage Electron Microscopes

## Transmission Electron Microscopes by Delong Instruments

We produce unique, compact table-top TEMs with very small footprints, entry level prices and no special technical requirements (no darkrooms, cooling water or high-voltage outlets). They are ideal for Material and Life Sciences applications.



### LVM 5 NEW GENERATION

*The only table-top TEM in the world*

Ideal for nanomaterial imaging  
5kV TEM/STEM/ED/SEM (BSE) modes  
resolution of 1.2 nm

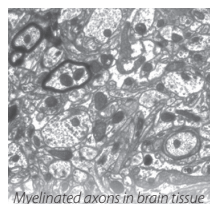
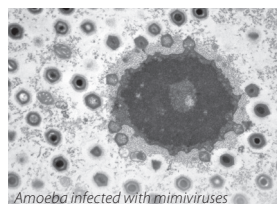
### LVM 25

*The latest compact multi-purpose TEM*

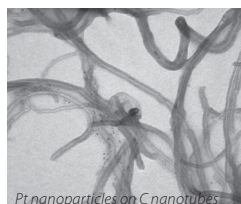
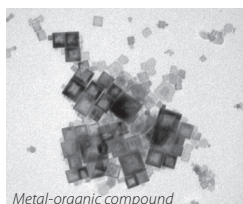
Ideal for biological  
& polymer applications  
25kV TEM/STEM/ED modes  
resolution of 1 nm



## Applications



polymers      composite materials  
**Material Sciences**  
nanomaterials      & more

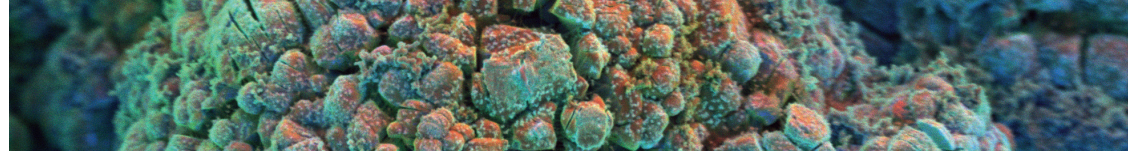


virology      pathology & neurology  
drug discovery      **Life Sciences**      cell biology  
& more



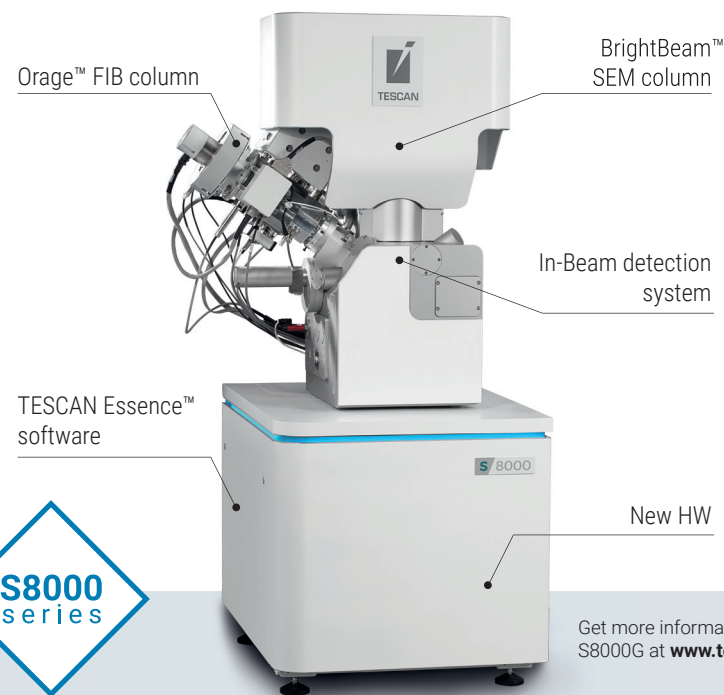
your way to electron microscopy

[www.delong.cz](http://www.delong.cz)



# TESCAN S8000G

RESOLUTION. CONTRAST. FLEXIBILITY.



#### BrightBeam™ SEM column

- Field-free ultra-high resolution SEM
- Excellent contrast on every sample

#### Orage™ FIB column

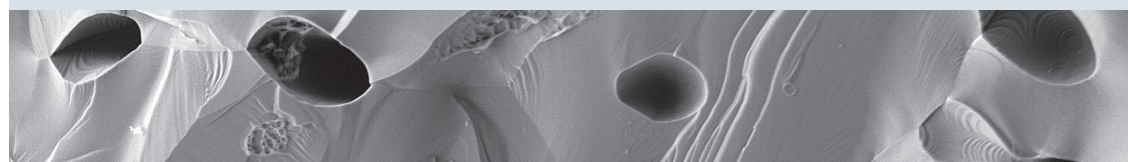
- Excellent low-kV resolution
- FIB currents up to 100 nA

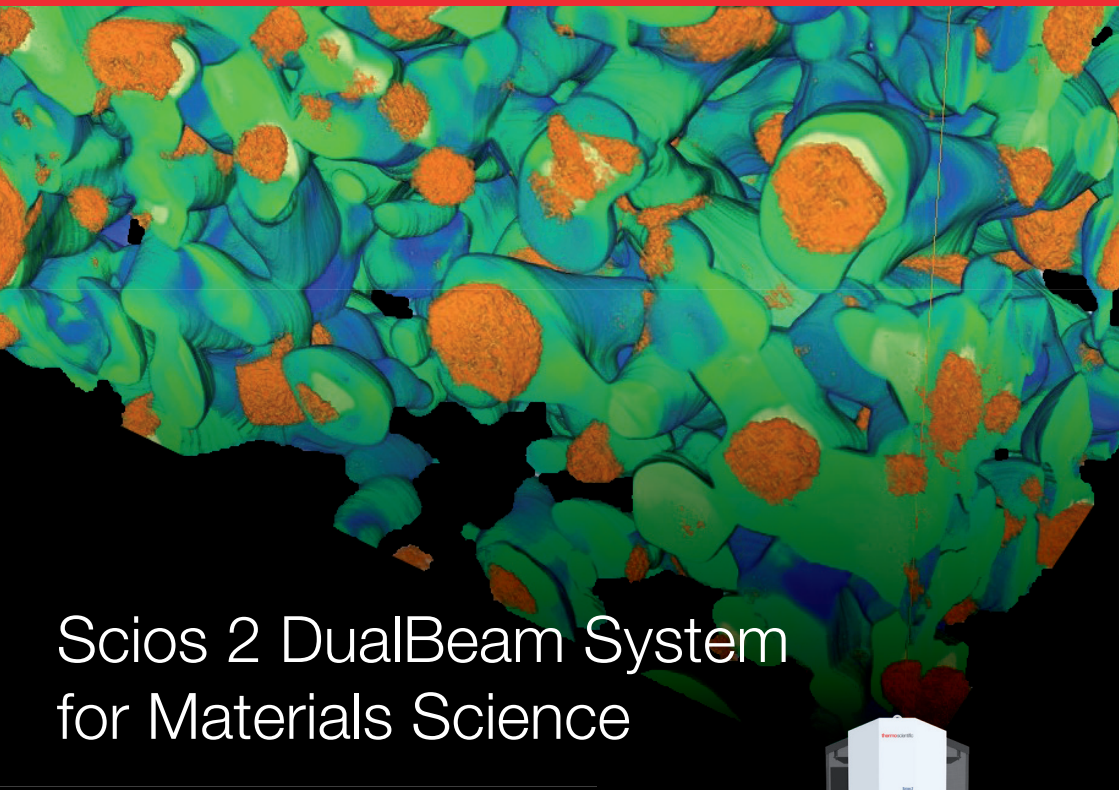
#### In-Beam detection system

- Energy-filtering BSE imaging
- Charge cancellation on samples

#### TESCAN Essence™ software

- Workflow-oriented wizards
- 3D collision model





## Scios 2 DualBeam System for Materials Science

### Versatility and High-Performance

The Thermo Scientific™ Scios™ DualBeam™ System is an ultra-high resolution analytical system that provides outstanding sample preparation and 3D characterization performance for the widest range of samples, including magnetic and nonconductive materials. It is an ideal solution to meet the needs of scientists and engineers in advanced research and analysis in all environments.



Find out more at  
[thermofisher.com/EM-materials-science](https://www.thermofisher.com/EM-materials-science)

**ThermoFisher**  
SCIENTIFIC

